Progression towards study of interactions with composite systems at ultracold temperature

by

Tridib Ray

a thesis submitted to
Jawaharlal Nehru University
for the degree of

Doctor of Philosophy

2014

Raman Research Institute
Bangalore 560 080
India

Declaration

I hereby declare that the work reported in this thesis is entirely original. This thesis has been composed by me at Raman Research Institute under the supervision of Dr. S. A. Rangwala. I further declare that, to my best knowledge, the matter presented in this thesis has not formed the basis for the award of any degree, diploma, membership, associateship, fellowship or any other similar title of any university or institution.

Tridib Ray

Countersigned:

Dr. S. A. Rangwala
Light and Matter Physics Group
Raman Research Institute
Bangalore-560 080

Certification

This is to certify that the thesis titled **"Progression towards study of interactions with composite systems at ultracold temperature"** submitted by Tridib Ray for the award of the degree of Doctor of Philosophy of Jawaharlal Nehru University is a bona-fide work. This has not been submitted to any other university for any other degree, diploma or title.

Dr. S. A. Rangwala
(Thesis Supervisor)
Light and Matter Physics Group
Raman Research Institute
Bangalore-560 080

Prof. Ravi Subrahmanyan
Director
Raman Research Institute
Bangalore-560 080

Acknowledgments

I wish to thank Dr. Sadiq Rangwala for giving me the opportunity to work in an exciting research field, and also for his guidance and constant supervision of my thesis work. It would not have been completed without his support and contribution towards this work.

I wish a very special note of thanks to Dr. Saikat Ghosh (IITK) for the active discussions and insightful comments on cavity physics and fiber optics. I gratefully acknowledge Dr. E. Krishnakumar (TIFR) for his technical support for high voltage switching.

My special thanks to Dr. Andal Narayanan, it was a pleasure to discuss my work with her. I also thank Dr. Reji Philip and his group for all the help received.

I sincerely thank Arijit and Jyothi for sharing experimental skills and knowledge, and also for useful discussions. Having them around was a great experience academically as well as personally. Special thanks to Jyothi for her significant role in the simulations and related discussions which undoubtedly helped us in understanding results from the experiments.

I thank Ravi and Lee for sharing lab time, instruments and knowledge.

I thanks Nandan and Deepak for all sort of academic and non-academic discussions.

I wish to thank Priya, Shafi, Surya and Asha for their help in lending us, in short notice, any instrument required.

My thanks to the director and the administrative department of Raman Research Institute (RRI) for facilitating the scientific environment. I gratefully acknowledge the technical support, N. Narayanaswamy and all other members of the general and precision workshops.

I sincerely thank to Mrs. Sujatha for her support in handling the electronic components used in the experiments.

I wish to show my gratitude to Harini, Savitha and Latha for their help. My special thanks to Shiva and Manju for all their hard work and support.

I thank the entire staff of RRI including library, computer department, canteen and

E B department who contributed in one way or the other in the accomplishment of the present work. Library staff's pleasant attitude was helpful throughout my PhD work.

For the non-scientific side of my PhD, my time at RRI was made enjoyable due to many friend and groups that became a part of my life. I enjoyed the presence of all the past and present members of the students' room: Deepak, Anirban, Nandan, Ravi, Lee, Jyothi, Rahul, Niranjan, Surya, Raviranjan, Madhuri and Amrutha in the Light and Matter Physics (LAMP) group.

I am indebted to RRI Football team for providing a stimulating and fun-filled evening time. It was a refreshing change from the work in the lab. I am happy to have enjoyed the post-football discussions in the ground.

Finally, I am indebted to my family for their faith, tremendous support and appreciation towards my thesis work. I appreciate your honest compliments and criticisms. I hope that this work makes you proud.

Synopsis

Trapped dilute mixtures of atoms, ions and molecules enable the study of a wide range of inter-species interactions, ranging from $1/r$ to $1/r^6$. The quantum nature of the interactions can be studied at ultracold temperature. Additionally a stable mixture opens up the possibility of non kinetic energy driven ultracold reactive chemistry. Techniques for production, trapping, cooling and detection of the individual species are well established and come with individual complexity. Recent efforts have been made to produce spatially overlapped mixtures of cold atoms and ions in a variety of systems ranging from single ion in BEC [1, 2], mixture of laser cooled ions [3] and atoms to spatially overlapped trapped ions with cold atomic ensemble [4–6].

Interaction of atoms, ions or molecules with quantized electromagnetic modes of an optical cavity allows the study of interesting physics ranging from optical bi-stability in weak coupling regime [7] to cavity QED in strong coupling regime [8]. The enhanced intensity of light and larger frequency selective interaction time due to long lifetime of resonant photons in the cavity makes the optical cavity an effective tool for precision spectroscopy and measurements [9].

The main motivation of the thesis is to build a platform that can create, cool and detect mixtures of atoms, ions and molecules, for the study of interaction at low temperature, within a Fabry-Perot cavity. The cavity can be used as a sensitive, frequency selective tool for probing the interactions in the mixture. In this thesis we describe the detailed construction of the apparatus. Then we study the interaction of the cold atomic ensemble in a magneto optical trap (MOT), with the quantized electro-magnetic mode of the cavity and the interactions of trapped atoms with the trapped ions. The atom cavity collective strong coupling is developed as a detection tool in the system. We demonstrate the formation of cold molecules in the apparatus and discuss possibility of trapping neutral molecules in the apparatus. Finally we demonstrate the formation, trapping and mass spectrometry of molecular ions in this system.

Design and construction of the hybrid apparatus

In contrast with the popular linear Paul trap [10] for study of ion-atom mixtures, we have utilized a modified spherical Paul trap, built using thin tungsten wires, in our system [11]. The open geometry of the trap provides large optical access to the center which allows a Fabry-Perot cavity to be built around it. The design is optimized keeping in mind the experimental requirements and the geometrical, optical and physical constraints. The detail of the process of assembling and aligning the components are discussed.

Collective strong coupling of atoms to the cavity

We have studied the collective strong coupling of the cold ^{85}Rb atomic ensemble with the fundamental mode of the cavity. In the experiment we prepare the atomic population in the $F = 3$ ground hyperfine state by sequentially switching off the cooling and the repumper laser. A very weak probe laser, scanning in frequency, is then passed through the cavity which excites the population. The strong coupling interaction between the atom and the field lifts the degeneracy of the system. As a result the transmitted spectra gets split (vacuum Rabi splitting) by a twice the coupling strength. The coupling strength (g) as a function of number of atoms effectively coupled to the cavity (N_c) is measured for the closed $F = 3 \leftrightarrow F = 4$ transition as well as for the open $F = 3 \leftrightarrow F = 3, 2$ transitions. It is observed that in the later case, weak repumper light is required in order to pump the atoms back to $F = 3$ ground state. The result agrees with the Tavis-Cumming model [12,13] where $g = g_0\sqrt{N_c}$. The experiments are performed with linear and circularly polarized light but no experimentally significant difference is found. This is because the randomly oriented atomic dipoles, in presence of the gradient magnetic field, see the probe light isotropically polarized. The experimental determination of the single atom coupling strength g_0, allows us to measure N_c at a given time. In the next experiment we perform ballistic expansion of the cloud by switching off the cooling process. The measurement of N_c as a function of time allows us to measure the rate of expansion and hence the initial temperature of the atomic

ensemble [14].

The ion trap and ion atom interactions

The modified spherical Paul trap is constructed using four thin tungsten wires wound in a square shape geometry. The center of the ion trap, by design, coincides with the center of the MOT which lies on the axis of the Fabry-Perot cavity. The novel design of the trap provides large optical access to the trap center. The ion trap is characterized in detail. The trap is loaded with $^{85}Rb^{+}$ ions derived from the parent MOT atoms by resonance enhanced two photon ionization (RE2PI). The number of ions trapped can be counted by extracting them onto a channel electron multiplier (CEM). Because the cavity is situated along the axis of the trap, a non standard transverse extraction is performed. The trap is well characterized and a good regime of operation for $^{85}Rb^{+}$ ions is established. The trap depth along radial and axial direction is determined by finding out the macro-motion resonance frequencies along the corresponding directions. The lifetime of the ions in the trap is measured in presence and absence of the MOT. When the ions are not in contact with the MOT, the RF heating leads to loss of the ions from the trap and eventually in few tens of seconds all the ions from the trap are lost. But when the ions are held together with cold atomic ensemble, the number of ions in the trap stabilizes to a value almost two third of the initial number. This demonstrates sympathetic cooling of ions by the localized parent cold atoms. There are two mechanisms for the cooling process. i) Elastic scattering, where the ion transfers a small amount of momentum to the atom with every scattering and hence cools down in multiple scattering events. ii) Resonant charge exchange, where the ion, in a glancing collision with the atom, receives an electron, and the newly created free atom escapes from the trap volume with the velocity of the incoming ion. On the other hand, the ion formed from the cold atom at the trap center has the low velocity of the parent atom and is trapped close to the center of the ion trap. As a result of the resonant charge exchange, the cold atom - hot ion pair ends up in a hot atom - cold ion pair in a single glancing collision. The hot atom leaves the trap (the vacancy get immediately filled as the MOT is con-

tinuously loading) and the cold ion gets trapped. This whole process of sympathetic cooling of ions by the localized ensemble of pre-cooled atoms [5, 11] leads to a stable ion-atom mixture which opens up the possibility of further studies including ultracold reactive chemistry [15, 16].

Toward composite molecular systems

Rb_2 molecules were formed from the MOT by photo-association (PA). We have used a $\sim$ 60 GHz red detuned laser for the process. In this process a colliding pair of ground state atoms, in presence of a photon (resonant to free to bound transition) forms a weakly bound excited molecular state. A fraction of the excited molecules then spontaneously decay to the deeper vibrational level of the ground electronic state forming a stable molecule. In our process of photo-association, the molecules created were not trapped and hence they escape from the MOT region. This introduces a mechanism for loss of atoms from the MOT. When the PA laser is scanned in frequency, dips in the MOT fluorescence can be observed as a result of atom loss from the MOT. We have observed the MOT loss spectra by scanning the PA laser.
In presence of the cooling laser light, a fraction of the Rb atoms in the MOT forms long range molecules by photo-associative process which are lost as they are not trapped. We use a nanosecond (ns) pulsed dye laser operated at 602.6nm, pumped by the second harmonic of a pulsed Nd-YAG laser, to perform a resonant two photon ionization of these molecules. The molecular ions produced in this process are then trapped in the ion trap. Atomic ions are also formed in the same process which are simultaneously trapped with the molecular ions. We perform a mass spectrometry to detect the ions by extraction onto the CEM [17].

Summary

In summary, we have designed, built and implemented a unique hybrid apparatus for the study of multi species interactions at ultracold temperature. The collective strong coupling of the cold atoms with the quantized electromagnetic mode of the cavity is

studied and it is developed as a tool for probing interactions in the system. The ion trap is characterized in detail and sympathetic cooling of the ions by the parent atoms is demonstrated. Finally formation of cold molecule and formation and trapping of molecular ions are demonstrated. The results establish the apparatus as an ideal platform for a variety of experimental investigations, including ultracold reactive chemistry, at low temperature.

Contents

CHAPTER 1

Introduction

1.1 Overview

Development of techniques for the production of cold, localized atomic ensembles [18] has opened up a new era of atomic physics. A variety of experiments have been performed with cold and ultracold gases for the study of many interesting problems ranging from fundamental interactions [19, 20], quantum simulators for magnetism [21], quantum computation [22], many and few body physics [23] etc. On the other hand, developments on trapping of ions and ability of laser cooling has provided excellent opportunity to study equally interesting problems ranging from precision metrology and clock, quantum computation, QED [24–26] etc. In fact, due to the similarity in the atomic structure and ability of preparing the systems of atoms and ions in specific quantum states, often similar physics has been demonstrated by both cold atom and ion systems. The interactions in pure atomic and pure ionic systems allows extensive studies of long range interactions of the form of $1/r^6$ (induced dipole - induced dipole) and $1/r$ (Coulomb) respectively.

Trapping of ions and atoms with spatial overlap opens up the possibility of studying interactions between the two species, both reactive and non-reactive. The long range interaction of an ion with a permanent dipole is $1/r^2$ in nature. In a system where the ion can reach much closer to the atom, it induces a dipole moment to the atom, leading to $1/r^4$ type relatively short range interactions. In case of atoms and ions, as the time averaged atomic dipole moment $< \mu >_{at} = 0$, the lowest order of non-vanishing interaction between the ion and the atom is $1/r^4$ due to the polarizability mediated interaction between them. W. W. Smith et. al [27] first demonstrated a hybrid trap that allows simultaneous and spatially overlapped trapping of atoms and ions. A group of labs across the world has demonstrated interesting physics arising from ion-atom in-

teractions in hybrid traps in a variety of systems. Single trapped ion inside BEC [1, 2], co-trapped laser cooled ions and atoms [3], spatial overlap of hot ions and cold atomic ensemble [4–6] are to name a few.

Developments in physics with optical cavities has enabled creation of quantized electromagnetic vacuum with desired boundary conditions, making it an attractive tool for a variety of experiments. Cold atomic and ionic ensemble have been separately coupled to optical cavities both collectively or at single entity limit. The interactions have been studied over a wide range of experimental systems [9] ranging from optical bistability [7], weak measurement [8], quantum entanglement [8], precise spectroscopy [28], study of QED [29] to enumerate a few.

Direct laser cooling of molecules is very challenging because of large number of states and absence of closed transition in molecules. There have been only some recent success [30, 31] in past few years. However to establish a general technique for direct laser cooling and specific state preparation of molecules are still challenging task. The most popular route for creation of cold molecules is from cold atomic ensemble. Co-existing mixture of atoms and molecules offers the study of anisotropic interactions. The dipole-dipole interactions can be of $1/r^3$ (static dipoles) or $1/r^6$ (freely rotating dipoles in space). In addition, reactive chemistry is possible in such mixture.

Overall, the study of cold dilute gas mixtures in the field of atomic physics has been of immense interest and holds out the promise of rich physics in near future. Although successful experiments have been performed with any two of these species, attempts have not been made toward combining these technologies to provide a common platform for study of multi-species interactions. In this thesis we address this problem and try to provide such common platform for the study of multi-species interactions at cold temperatures.

1.2 Motivation

Trapping of atoms, ions and molecules at low temperature in the same spatial region offers study of inter-species interactions at a largely unexplored region of collision energies below 1eV. Few and many body interactions, ranging from $1/r$ to $1/r^6$, can be studied by choosing the right combination of the mixture. Precise measurements, free from Doppler and other kinetic energy effects can be performed at cold temperature. The stable co-existence of such mixture opens up the possibility of non kinetic energy driven reactive chemistry leading to production of complex molecules at cold temperatures. The molecules offer internal degrees of freedom which can be manipulated in order to explore physics of inter-species interactions. Further, a class of the interactions can be be initiated, enhanced, tuned, or inhibited by means of near resonant photons or modified electro-magnetic (EM) vacuum inside an optical cavity.

The primary motivation of this work is to explore the physics of such multi-species mixture at low temperatures. Further, we implement an optical cavity around the hybrid trap to study interactions of the species within, with quantized EM field which can be developed as a frequency sensitive detection tool. The cavity can also be used for photon mediated reactive chemistry.

1.3 Objective

The primary objective of this work is to create a platform which provides the opportunity to create spatially overlapped mixtures of atoms, ions and molecules at low temperature, within an optical cavity and to study some of the interactions. The concept of an ideal apparatus is explained in a cartoon below (Fig.1.1). There exist established techniques for the implementation of each of the above-mentioned. The idea is to combine them in a feasible geometry so that the trapping, cooling and detection for the species can be done without interfering each other's performance.

Below we identify the key objectives of the thesis

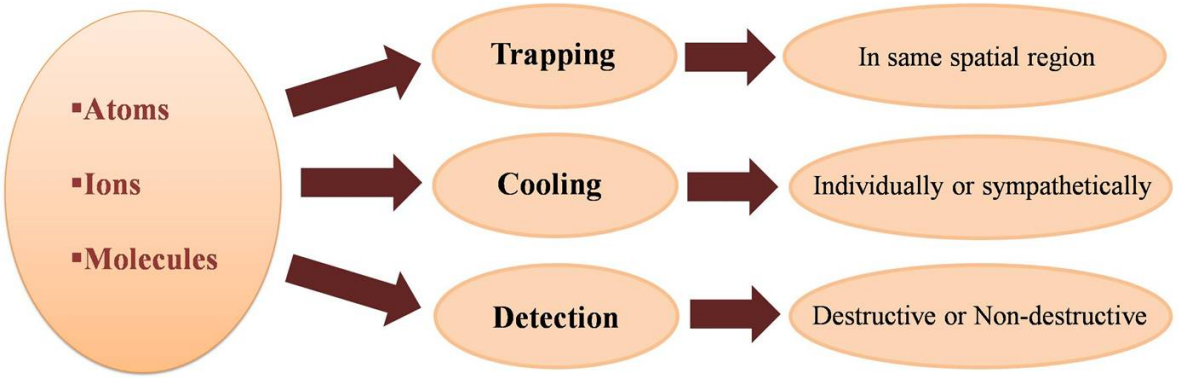

Figure 1.1: Concept of an ideal apparatus for the study of inter-species interactions. Atoms, ions and molecules must simultaneously trapped in the same spatial region. There must be process for cooling of each of the species. This can be direct laser cooling or any other process like sympathetic cooling. There must be mechanism for detection for the species trapped, preferably non-destructive. Sometimes for optically dark ions we have to use destructive detection method like extracting onto a channel electron multiplier.

- To design a hybrid apparatus that is capable of creating spatially overlapped dilute mixtures of atoms, ions and molecules, within a Fabry-Perot cavity. Individual aspects of trapping, cooling and detection of the species are addressed.
- To construct the hybrid apparatus and demonstrate its operation.
- To characterize the free space operation of the Fabry-Perot cavity.
- Investigate the collective strong coupling of the atoms with the fundamental mode of the cavity.
- To establish the atom-cavity strong coupling as a detection tool to probe the interactions. Use the technique to measure the temperature of the cold atomic ensemble.
- Characterize the ion trap and finding out the optimal region of operation.
- Establishing reliable detection techniques for the optically dark ions.
- Demonstration of stabilization of the ion-atom mixture and sympathetic cooling of ions by the parent cold atoms.

- Production of cold molecules from the cold atomic ensemble using photoassociation and explore the possibilities of trapping neutral molecules in the apparatus.
- Creation of molecular ions and demonstration of simultaneous trapping of atomic and molecular ions.

1.4 Organization of the thesis

In the second chapter we discuss the conceptual background of the experiments performed. A brief introduction to laser cooling and magneto-optical trap is provided. We discuss the solution of wave equation with imposed boundary conditions. A detail understanding of spherical mirror Fabry-Perot cavity is given. Collective coupling of the atoms to the fundamental mode of the cavity is also discussed. At the end, we provide an understanding of ion trap and its operation.
In the third chapter we discuss the detail design of the apparatus and the construction process. The detail of the lasers used for the experiments and the optical setup are also discussed.
In the fourth chapter, we characterize the free-space operation of the Fabry-Perot cavity. Then we discuss the formation of MOT inside the cavity and methods of detection of atoms from the MOT. Atom-cavity collective coupling is demonstrated for closed as well as the open atomic transitions. Vacuum Rabi split was observed as a proof of strong coupling and its variation with number of atoms coupled to the cavity was measured. The atom-cavity coupling is then developed as a tool for detection and the temperature of the cold atomic ensemble was measured using it.
The fifth chapter is dedicated for the ion trap, its operation and characterization. We characterize the trap in detail to find out the optimal operating region and compare it with the results obtained in simulation. We find the trap depth at the optimal operating parameters by means of a combination of simulation and experiment. We demonstrate the stabilization of the number of ions in the trap when held together with the cold atomic ensemble and attribute this to the sympathetic cooling of the ions by the cold

atoms. Finally we discuss a possible method of non-destructive detection of the dark ions by means of the cavity.

In the sixth chapter we demonstrate formation of composite objects. We demonstrate photo-associative production of homonuclear molecules. We discuss possibilities of trapping neutral molecules that can be implemented within the infrastructure of the apparatus. We finally demonstrate the production and trapping of molecular ions. We conclude the thesis by summarizing the work and the future prospects of research with multi-species experiments in such hybrid apparatus.

CHAPTER **2**

The conceptual background for the experiments

2.1 Overview

The experimental apparatus envisaged in the beginning of this thesis is extremely involved and complex. The apparatus constructed is unique of its kind. The construction and operation of the hybrid apparatus relies on careful understanding of the detailed background of several critical technologies and systems which have to be carefully put together. The resulting amalgam, that our experiment is, needs to work without any crosstalk from the atom trap, ion trap and cavity, yet allowing the species trapped within to interact. In this chapter we will discuss the conceptual backgrounds of the techniques that form the basis of the experiments reported in this thesis. We start with trapping and cooling of neutral atoms in a Magneto Optical Trap (MOT), follow up with a discussion on cavity and atom-cavity coupling and conclude with trapping of ions in a Paul trap.

2.2 Interaction of a classical field with a two level atom

Let us consider an ensemble of two level atoms consisting of the ground state $|g\rangle$ and the excited state $|e\rangle$ with eigen energies E_g and E_e respectively. The system can be described by the density matrix

$$\rho = \begin{pmatrix} \rho_{ee} & \rho_{eg} \\ \rho_{ge} & \rho_{gg} \end{pmatrix}$$

The diagonal elements of the density matrix ρ_{ee} and ρ_{gg} represents the population in the states $|e\rangle$ and $|g\rangle$ respectively, whereas the off-diagonal terms represents the co-

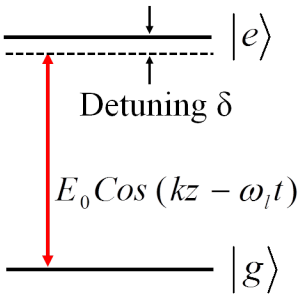

Figure 2.1: Two level atom consisting of ground state $|g\rangle$ and excited state $|e\rangle$ is interacting with a laser radiation field of frequency ω_l. δ is the detuning of the laser from the atomic resonance frequency ω_{eg}.

herence. For simplicity of calculation we consider $E_g = 0$. The atomic part of the Hamiltonian is

$$\hat{H}_A = \hbar\omega_{eg}|e\rangle\langle e|, \tag{2.1}$$

where $\omega_{eg} = (E_e - E_g)/\hbar$ is the transition frequency from the state $|e\rangle$ to $|g\rangle$.

Now let us assume that the atoms are at rest and interacting with a monochromatic, near-resonant radiation field $\vec{E} = \vec{\epsilon}E_0 cos(kz - \omega_l t)$, $\vec{\epsilon}$ being the direction of the polarization. The atom-field interaction Hamiltonian is

$$\hat{H}_I = -\hat{\vec{\mu}} \cdot \vec{E} = -e\hat{\vec{r}} \cdot \vec{E}, \tag{2.2}$$

where $\hat{\vec{\mu}}$ is the atomic dipole moment operator and e is the electron charge. Under the rotating wave approximation, the interaction Hamiltonian can be written as [32]

$$\begin{aligned} \hat{H}_I &= -\frac{\hbar\Omega}{2}(|e\rangle\langle g|e^{-i\omega_l t} + |g\rangle\langle e|e^{i\omega_l t}) \\ &= -\frac{\hbar\Omega}{2}(\hat{\sigma}^\dagger e^{-i\omega_l t} + \hat{\sigma}e^{i\omega_l t}) \end{aligned} \tag{2.3}$$

$\hat{\sigma}^\dagger = |e\rangle\langle g|$ and $\hat{\sigma} = |g\rangle\langle e|$ are the atomic raising and lowering operators respectively. Ω is the Rabi frequency of oscillation of the atomic population between the states $|g\rangle$ and $|e\rangle$ under the influence of the radiation and is given by

$$\Omega = -\frac{eE_0}{\hbar}\langle e|\vec{r}|g\rangle \tag{2.4}$$

The dynamics of the system can be described by the time evolution of the density matrix. In Heisenberg picture, the time evolution of the density matrix is given by it's

commutator with the total Hamiltonian $\hat{H} = \hat{H}_A + \hat{H}_I$

$$\dot{\rho} = -\frac{i}{\hbar}[\hat{H}, \rho] \tag{2.5}$$

The finite lifetime of the atomic excited state introduces a dissipative loss mechanism. We introduce Γ as the spontaneous emission rate from the excited state $|e\rangle$ so that Γ^{-1} is the radiative lifetime of the state. In presence of this loss, the time evolution of the density matrix is given by the Lindblad equation [33]

$$\dot{\rho} = -\frac{i}{\hbar}[H, \rho] - \frac{\Gamma}{2}[\sigma^{\dagger}\sigma\rho - 2\sigma\rho\sigma^{\dagger} + \rho\sigma^{\dagger}\sigma] \tag{2.6}$$

which leads to the optical Bloch equation for the two level atomic system

$$\begin{aligned}
\dot{\rho}_{ee} &= -\Gamma\rho_{ee} + \frac{i\Omega}{2}(\tilde{\rho}_{ge} - \tilde{\rho}_{eg}) \\
\dot{\rho}_{gg} &= \Gamma\rho_{ee} - \frac{i\Omega}{2}(\tilde{\rho}_{ge} - \tilde{\rho}_{eg}) \\
\dot{\tilde{\rho}}_{eg} &= (-\frac{\Gamma}{2} + i\delta)\tilde{\rho}_{eg} - \frac{i\Omega}{2}(\rho_{ee} - \rho_{gg}) \\
\dot{\tilde{\rho}}_{ge} &= (-\frac{\Gamma}{2} - i\delta)\tilde{\rho}_{eg} + \frac{i\Omega}{2}(\rho_{ee} - \rho_{gg})
\end{aligned} \tag{2.7}$$

Where $\tilde{\rho}_{eg} = \rho_{eg}e^{i\omega_l t}$. We have introduced $\delta = \omega_l - \omega_{eg}$ as the detuning between the laser frequency and the atomic transition frequency. The first two equations describe the evolution of the atomic population in the excited and the ground state respectively whereas the last two equations describe the change in coherence with time. In a closed system, the total population distributed among the ground and the excited state is constant. So that,

$$\dot{\rho_{ee}} = -\dot{\rho_{gg}} \tag{2.8}$$

which reduces the total number of the optical Bloch equations to three. In steady state, the density matrix does not change with time. So applying $\dot{\rho} = 0$ in equation 2.7, we get the steady state solutions. Here we are interested in the steady state population in the excited state

$$\rho_{ee} = \frac{\Omega^2}{\Gamma^2 + 2\Omega^2 + 4\delta^2} \tag{2.9}$$

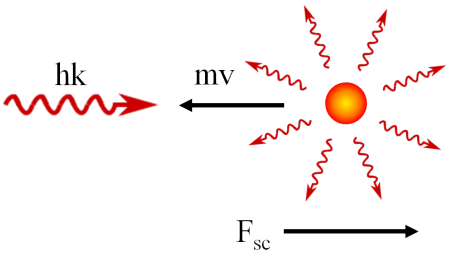

Figure 2.2: The figure shows the scattering force on an atom by momentum transfer due to successive absorption and spontaneous emission photons. Initial momentum of the atom is mv where m is the mass of the atom and v is the velocity. Absorption of a single photon leads to a net momentum loss of hk of the atom, where k is the wavenumber of the incident photon. The spontaneously emitted photon is emitted in a random spatial direction. So the time averaged momentum change due to spontaneous emission is zero.

As the Rabi frequency depends on the intensity $I = |E_0|^2$ of the laser radiation, the steady state population in the excited state can be written as a function of the laser intensity

$$\begin{aligned} \rho_{ee} &= \frac{1}{2}\frac{I/I_{sat}}{1 + I/I_{sat} + 4\delta^2/\Gamma^2} \\ &= \frac{1}{2}\frac{s_0}{1 + s_0 + 4\delta^2/\Gamma^2} \\ &= \frac{s}{2(1+s)} \end{aligned} \tag{2.10}$$

Where $I_{sat} = \frac{\pi\hbar c\Gamma}{3\lambda^3}$ is the saturation intensity, $s_0 = I/I_{sat} = 2\Omega^2/\Gamma^2$ is the on resonance ($\delta = 0$) saturation parameter and $s = \frac{s_0}{1+4\delta^2/\Gamma^2}$ is the off resonance saturation parameter. Clearly with increase of the incident laser intensity I, more fraction of the atomic population populates the excited state. On resonance, at $I = I_{sat}$, one fourth of the total atomic population is in the excited state (see eq.2.10). The spontaneous emission rate from the excited state is given by Γ. Hence the rate at which the photons are scattered from the ensemble is

$$R_{sc} = \frac{\Gamma}{2}\frac{I/I_{sat}}{1 + I/I_{sat} + 4\delta^2/\Gamma^2} \tag{2.11}$$

When an atom absorbs a photon, its momentum gets transferred to the atom. After the lifetime of the excited state, the photon is spontaneously emitted. The direction of

the emission is random and hence the average momentum transfer is zero. The stimulated emission does not change the momentum of the atom as the emitted photon has the same direction, momentum and polarization of the absorbed photon. So on the average, the atom experience a force causing a change of momentum due to scattering of photons. Considering the momentum of the photon to be $\hbar k$, the force due to scattering of photons exerted on the atom is

$$F_{sc} = \hbar k \frac{\Gamma}{2} \frac{I/I_{sat}}{1 + I/I_{sat} + 4\delta^2/\Gamma^2} \tag{2.12}$$

For a stationary atom, force from two counter-propagating beams of equal intensity balance each other and the net force on the atom is zero.

2.3 Cooling and trapping of neutral atoms

The idea of cooling of neutral atoms by scattering of near resonant photons was first proposed in 1975 by T. Hansch and A. Schawlow [34]. Chu et. al. [18] in 1985 demonstrated the "Three-dimensional viscous confinement and cooling of atoms by resonance radiation pressure". Further, suggested by Jean Dalibard et. al. and demonstrated by Raab et. al. [35] in 1987, in a MOT, position dependence of the viscous force is introduced by an inhomogeneous magnetic field which, along with the laser radiation, simultaneously cools and spatially confines the cold atoms. Magneto optical trap, soon after its demonstration has become the most widely used technique for producing spatially confined cold atoms due to its robustness and simplicity. In the sections below we will describe the basic concepts of Doppler cooling and MOT.

2.3.1 Doppler cooling: Optical molasses

Let us consider an atom moving at a velocity v and interacting with two balanced counter-propagating beam of frequency ω_l which is red detuned from the atomic resonance ω_{eg} by δ (Fig.2.3). For simplicity we consider a one dimensional case where the atom moves either in or against the direction of the k vector of the laser radiation. In

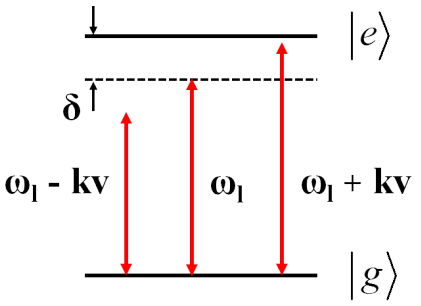

Figure 2.3: The figure explains the concept of Doppler cooling using red detuned laser beam. The atoms that are counter propagating the laser beam, see the frequency Doppler shifted toward the atomic resonance, resulting enhanced photon scattering. Whereas the atoms that are co-propagating the laser beam, see the frequency Doppler shifted away from the atomic resonance, resulting in a reduction of photon scattering. This process introduces a frictional force against the velocity of the atoms and leads to cooling.

the frame of reference of the atom, the atom sees the frequency of the light Doppler shifted by kv. The sign of the shift depends on the relative velocity of the atom w.r.t the k vector of the laser beam. The atoms moving against the k vector will see the frequency shifted by $+kv$ and hence closer to the atomic resonance. Whereas the atoms moving along the k vector will see the frequency shifted by $-kv$ and hence away from the atomic resonance. This leads to a radiation force against the velocity of the atom caused by more scattering of photons by the atom from the beam propagating against its velocity. Mathematically the scattering force from the two beams will be

$$F_{\pm} = \pm\hbar k \frac{\Gamma}{2} \frac{I/I_{sat}}{1 + I/I_{sat} + 4(\delta \mp kv)^2/\Gamma^2} \tag{2.13}$$

where $F_{\pm}$ is the force from the beam co/counter propagating w.r.t the atomic velocity. So the total force on the atom will be

$$\begin{aligned} F_{om} &= F_{+} - F_{-} \\ &= -4\hbar k^2 v \frac{I}{I_{sat}} \frac{2\delta/\Gamma}{1 + 4\delta^2/\Gamma^2} \\ &= -\alpha v \end{aligned} \tag{2.14}$$

where α is the proportionality constant that depends on the choice of transition (Γ) in a specific atomic species and the experimental parameters δ, I.

Clearly the total force on the atom is frictional in nature. So the atom in motion will experience a damping force against its velocity. As a result, the atom will lose momentum and translationaly cool till it comes to rest. At rest, the F_+ and F_- cancels out each other as described earlier and no net force is applied on the atom. This opens up the possibility of a cooling mechanism of neutral atoms, namely optical molasses [18]. A combination of three orthogonal pairs of counter-propagating beams can cool an ensemble of atoms in all three directions and leads to a cold atomic ensemble at the intersection.

2.3.2 Position dependent force: MOT

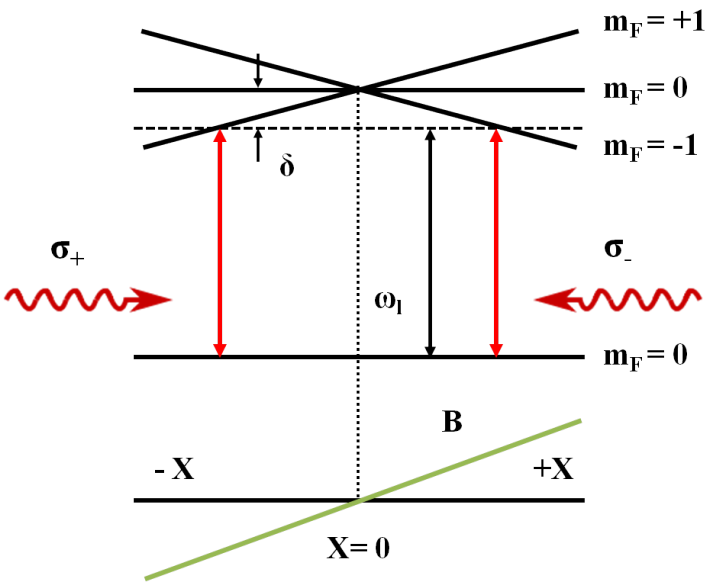

Figure 2.4: The figure explains the concept of MOT. The inhomogeneous magnetic field (green line) B causes position dependent Zeeman splitting of the hyperfine levels. Here the $F = 1$ excited hyperfine state splits into three Zeeman sublevels $m_F = -1, 0, +1$ and the amount of splitting depends on position. The $F = 0$ ground hyperfine state does not undergo any split. The selection rule $\Delta m_F = \pm 1$ ensures enhanced scattering of photons from the counter-propagating beams of orthogonal circular polarization when the atom tends to move away from the center. The result is a position dependent force that localize the cooled atoms.

The technique of optical molasses, described in the previous paragraph, provides

a mechanism for cooling of neutral atoms but does not localize the cooled atoms in space. In Magneto Optical Trap, a position dependence of the scattering force, along with the velocity dependence, is introduced by means of an inhomogeneous magnetic field. The magnetic field is created by a co-axial pair of coils in anti-Helmholtz configuration along the z-axis. In absence of the magnetic field the Zeeman sublevels (denoted here by m_F) within a hyperfine level (total spin F) are degenerate. The field lifts the degeneracy of the m_F levels. The inhomogeneity of the field causes the splits of various Zeeman sublevels to be position dependent. For simplicity we choose the hyperfine levels, for the ground state with $F = 0$ and for the excited state $F = 1$, so that the ground state does not experience Zeeman splitting in the magnetic field and the excited state splits into three states $m_F = -1, 0, +1$. The energy $m_F = -1$ and $m_F = +1$ states has position dependence as shown in Fig.2.4. Two counter propagating beams of opposite polarization, are interacting with the atom. When the atom is away from the center in $+\hat{x}$ direction, the level $m_F = -1$ becomes near resonant with the applied laser frequency and the selection rule is also satisfied for σ_- polarization. The atoms in that state and position experience enhanced scattering of photon from the σ_- polarized beam until it moves back toward position $x = 0$. A similar enhanced scattering from the atoms takes place from the σ_+ polarized beam, when the atom is displaced along $-\hat{x}$ direction. The tendency of scattering more photons away from the origin develops into a position dependent restoring force which allows the cooled atoms to be localized in space. Mathematically, the force from a pair of balanced counter propagating laser beams of orthogonal polarization is

$$F_{\sigma\pm} = \pm\hbar k \frac{\Gamma}{2} \frac{I/I_{sat}}{1 + I/I_{sat} + 4(\delta \mp (kv - \beta x))^2/\Gamma^2} \tag{2.15}$$

where β determines the Zeeman shift under the magnetic field B and

$$\beta = \frac{g_{eff}\mu_B}{\hbar}\frac{dB}{dx} \tag{2.16}$$

where g_{eff} is the effective Lande g factor. So the total force on the atoms is

$$\begin{aligned} F_{mot} &= F_{\sigma+} - F_{\sigma-} \\ &= -\alpha v - \frac{\alpha\beta}{k}x \end{aligned} \tag{2.17}$$

Clearly, along with the frictional force, the atoms experience a harmonic restoring force with the spring constant of $\alpha\beta/k$. This process simultaneously traps and cools the atoms leading to a localized cold ensemble of neutral atoms which is very convenient and useful for a variety of experiments. The remarkable point about this process is that the same magnetic coil pair can be used for cooling and trapping different atomic species simultaneously. As far as the alkali atoms are concerned, the $\hat{\vec{\mu}}.\vec{B}$ interaction depends on the moment of the outermost electron and $\vec{B}$ which is same for all the atoms. The efficiency of the cooling and trapping process in a MOT for different species is thus different only because of mass of the atom and the selected optical transition. This provides a versatile platform for the study of interactions of neutral atomic species at low temperature.

2.4 Wave equation and its solution

Let us start with the vacuum wave equation which determines the propagation of any electromagnetic(EM) wave $\vec{E}(r,t)$ in the free space.

$$\nabla^2\vec{E}(r,t) = \frac{1}{c^2}\frac{\partial^2}{\partial t^2}\vec{E}(r,t) \tag{2.18}$$

This equation has infinite number solution. The *plane wave* and the *spherical wave* solutions are two of specific relevance and widely known.
Here we consider scalar electric field with explicit time dependence as

$$E(\vec{r},t) = \hat{\epsilon}E_0\psi(\vec{r})e^{i\omega t} \tag{2.19}$$

where $\hat{\epsilon}$ is the unit vector in the direction of the polarization. We also assume that the propagation of the wave in space is paraxial so that the wavefront is normal to the wave vector. For a wave propagating in the z direction,

$$\psi(\vec{r}) = u(x,y)e^{ikz} = u(r_T,\theta)e^{ikz} \tag{2.20}$$

where (x,y) and (r_T,θ) represents the orthogonal coordinates of a 2D Cartesian or cylindrical coordinate system respectively. Inserting eq.(2.19) and eq.(2.20) into eq.(2.18)

and neglecting the fast varying term of ψ w.r.t z under the slowly varying approximation, we get

$$(\nabla_T^2 + 2ik\frac{\partial}{\partial z})\psi = 0 \tag{2.21}$$

where ∇_T^2 is the transverse Laplacian and is given by

$$\nabla_T^2 = \frac{\partial^2}{\partial x^2} + \frac{\partial^2}{\partial y^2} \tag{2.22}$$

Eq.(2.21) is known as *transverse Helmholtz equation* and governs the propagation of a paraxial wave in space. The transverse Helmholtz equation has many solutions. Depending on the symmetry of the boundary conditions, polynomial solutions may exist. These solutions are denoted as $TEM_{m,n}$ where m and n are the order of the polynomials in the corresponding transverse coordinates. The fundamental mode TEM_{00} for a regular symmetric boundary condition is given by [36]

$$\psi(r) = \frac{w_0}{w(z)} exp[-\frac{{r_T}^2}{w^2(z)}] \times exp[ikz - itan^{-1}(\frac{z}{z_0})] \times exp[ik\frac{{r_T}^2}{2R(z)}] \tag{2.23}$$

where E_0 is the electric field amplitude constant. The light is assumed to be monochromatic of wavelength λ. The beam waist is defined as the minimum beam radius and is given by

$$w_0 = \sqrt{\lambda z_0 / \pi} \tag{2.24}$$

The Rayleigh length z_0 is the distance from the waist, along k, where the area of the beam is double than that of at the waist. This parameter depends exclusively on the geometry of the boundary conditions. The *beam radius* and the *radius of curvature* of the beam at a distance z is given respectively as

$$w(z) = w_0\sqrt{1 + (z/z_0)^2} \tag{2.25}$$

$$R(z) = z[1 + (z/z_0)^2] \tag{2.26}$$

The first part of ψ in eq.(2.23) provides information about the electric field amplitude. $w_0/w(z)$ gives the decay of the electric field on the axis ($r_T = 0$) with propagation. At a given z, the electric field amplitude away from the axis is given by the factor $exp[-{r_T}^2/w^2(z)]$. The second part is the longitudinal phase factor, on the axis, acquired with propagation. $exp(ikz)$ is the phase factor due to plane wave propagation.

Due to structural deviation from the plane wave, the Gaussian wave acquires an additional phase, given by $tan^{-1}(z/z_0)$ over propagation. This phase is called *Gouy phase* and monotonically increases with propagation. The last part $exp[ikr_T{}^2/2R(z)]$ represents the radial phase factor arising from deviation from the axis of propagation.

Higher order modes

The structure of the higher order modes depends on the symmetry of the boundary condition on the radial plane. For $x-y$ symmetry, the solutions are in terms of Hermite polynomial and the higher order modes of this *Hermite - Gaussian* beams are given as [37]

$$\psi(r) = \frac{w_0}{w(z)} H_m\left[\frac{\sqrt{2}x}{w(z)}\right] H_n\left[\frac{\sqrt{2}y}{w(z)}\right] exp\left[-\frac{r^2}{w^2(z)}\right]$$
$$\times exp\left[ikz - i(m+n+1)tan^{-1}(\frac{z}{z_0})\right] \times exp\left[ik\frac{r^2}{2R(z)}\right] \tag{2.27}$$

where m and n are the orders of the polynomials along x and y directions respectively.

Similarly a boundary condition with cylindrical symmetry leads to the higher order *Laguerre - Gaussian* beams which can be represented as [37]

$$\psi(r) = \frac{w_0}{w(z)}\left(\frac{\rho}{w^2(z)}\right) L_n^m\left[\frac{2\rho^2}{w^2(z)}\right] exp\left[-\frac{\rho^2}{w^2(z)}\right] exp[-im\phi]$$
$$\times exp\left[ikz - i(m+2n+1)tan^{-1}(\frac{z}{z_0})\right] \times exp\left[ik\frac{\rho^2}{2R(z)}\right] \tag{2.28}$$

2.5 Fabry-Perot cavity

2.5.1 Plane mirror cavity

We consider the simplest type of cavity, the *plane mirror cavity* consisting of two plane mirrors placed parallel, facing each other. The EM wave inside the cavity forms standing wave by multiple reflection from the two mirrors. For a monochromatic plane wave of frequency ν (wavevector k), the criteria to form the standing wave is that the

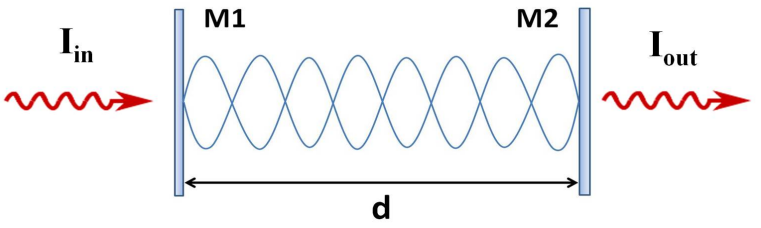

Figure 2.5: A plane mirror cavity consisting two plane mirrors separated by a distance d. When the resonance condition (given in eq.(2.29) is satisfied, the electric field forms a standing wave in the resonator so that the input light can transmit through the cavity.

total round trip phase will be integer multiply of 2π.

$$\begin{aligned} 2kd &= 2\pi q \\ or, \nu_q &= \frac{cq}{2d} \end{aligned} \tag{2.29}$$

where q is any integer and d is the distance between the two mirrors. So, for a light, scanning in frequency, as input to the cavity, whenever this resonance criteria is satisfied, light gets coupled out of the cavity. The difference in frequency between two peaks is called the *Free Spectral Range (FSR)* and is given by

$$FSR = \frac{c}{2d} \tag{2.30}$$

where c is the speed of light in free space. FSR is the inverse of the time taken by a photon for a complete round trip of the cavity. Ideally for a pair of perfectly reflecting mirrors, the cavity resonance peaks are delta function. But in practice, the finite reflectivity of the mirrors and several other loss mechanisms of the photons from the cavity (e.g. absorption and scattering of photons by the mirrors) leads to broadening of the peak. Assuming the photon losses are caused by only transmission through the mirrors, the full width at half maximum (FWHM) of the peaks are given as

$$\Delta\nu_{ideal} = FSR/F \tag{2.31}$$

where F is the finesse of the cavity and is determined by the reflectivity of the mirrors r_m as [36]

$$F_{ideal} = \frac{\pi\sqrt{r_m}}{1 - r_m} \tag{2.32}$$

$F/2\pi$ is the number of round trip a photon executes before leaving the cavity. Hence the lifetime of a photon inside the cavity is given by

$$\tau_p = \frac{F}{2\pi(FSR)} = \frac{1}{2\pi\Delta\nu} \tag{2.33}$$

2.5.2 Cavity with concave mirrors

Now we consider a Fabry-Perot cavity consisting of concave mirrors with their reflective concave surface facing each other. Because of the geometry of the boundary conditions imposed of the EM field inside by the concave mirrors, the modes survive inside have much more complex structure than simple plane wave. Initially we consider only the fundamental mode TEM_{00}.

We consider symmetric Fabry-Perot cavity where the mirrors are of equal radius of curvature R. The separation between the mirrors are d. The primary criteria for the mode to survive within the cavity is that the radius of curvature of the beam should match to that of the mirror at the concave reflecting surface. This constraint on the geometrical structure of the mode, defines the Rayleigh length for the TEM_{00} mode as [36]

$$z_0 = \frac{d}{2}\sqrt{\frac{2|R|}{d} - 1} \tag{2.34}$$

And the corresponding beam waist as

$$w_0 = \sqrt{\frac{\lambda d}{2\pi}\left(\frac{2|R|}{d} - 1\right)^{1/2}} \tag{2.35}$$

Once the structure of the beam inside the cavity is defined, the resonance condition can be found out by equating total round trip phase to integer multiple of 2π. For a Gaussian beam, in addition to the plane wave phase factor, the Gouy phase makes the resonance condition different from the plane wave. The new resonance condition is

$$\begin{aligned} 2\pi q &= 2k_q d - \left(tan^{-1}\left(\frac{d/2}{z_0}\right) - tan^{-1}\left(\frac{-d/2}{z_0}\right)\right) \\ &= \frac{2\pi\nu_q d}{c} - 2cos^{-1}\left(1 - \frac{d}{|R|}\right) \end{aligned} \tag{2.36}$$

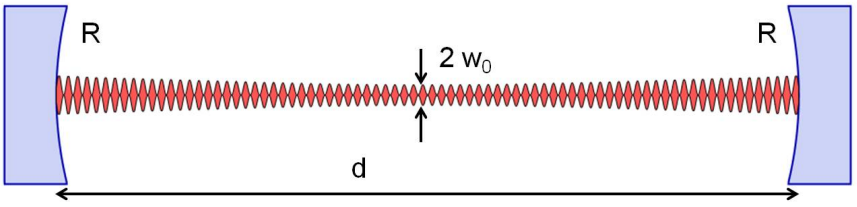

Figure 2.6: The figure shows a Fabry-Perot cavity consisting of two concave mirrors of radius of curvature R separated by a distance d. A schematic of the fundamental mode supported by the cavity is also shown.

so that the new resonance frequencies are

$$\nu_q = FSR\left(q + \frac{1}{\pi}cos^{-1}(1 - d/|R|)\right) \tag{2.37}$$

The point to note here is that although the resonance frequencies changes, the separation between two fundamental modes are still $c/2d$ i.e. FSR.

Resonance condition for higher order modes

Similar to the fundamental TEM_{00} mode, for the other higher order transverse modes also the Rayleigh length and the waist of the beam is determined by the radius of curvature of the two mirrors and their separation. The resonance condition for the TEM_{mn} can then be calculated in the similar way and the resonance frequencies for the TEM_{mn} mode is given as

$$\nu_{q,m,n} = FSR\left(q + \frac{1+m+n}{\pi}cos^{-1}(1 - d/|R|)\right) \tag{2.38}$$

one must notice that the modes $TEM_{m_1n_1}$ and $TEM_{m_2n_2}$ are degenerate if $m_1 + n_1 = m_2 + n_2$. Let us take $m + n = N$. The separation between the $q'th$ and the $(q+1)'th$ transverse mode of $N'th$ order is the FSR. The separation between the $N'th$ and the $(N+1)'th$ transverse mode within the same longitudinal manifold (same q) is given as [37]

$$\Delta\nu_{tr} = \frac{FSR}{\pi}cos^{-1}\left(1 - \frac{d}{|R|}\right) \tag{2.39}$$

2.5.3 Practical cavity

In the physical realization of an optical cavity, other than the loss of photons from the cavity due to the finite reflectivity of the mirrors, there are additional loss channels, for example the absorption and scattering of the photons from the mirrors. The effective FWHM of the peak reflects the total loss rate of the photons. The FSR does not change. So its more convenient to describe the systems in terms of loss rates. We assume both the mirrors to be identical and introduce the photon loss rate κ_m due to finite reflectivity r_m as

$$r_m = 1 - \kappa_m \tau_p \tag{2.40}$$

We also introduce κ_a as the loss rate due to all other process. So that the total loss rate κ is the sum of loss of photons from both the mirrors and the additional loss κ_a.

$$\kappa = 2\kappa_m + \kappa_a \tag{2.41}$$

We assume that the cavity length is tuned such that the resonance frequency for a particular mode is ω_c which satisfies the relation given in eq.(2.37). We define the laser-cavity detuning as

$$\Delta_c = \omega_c - \omega_l \tag{2.42}$$

where ω_l is the frequency of the laser interrogating the cavity. In this case the steady state transmittivity $\mathcal{T}$ and reflectivity $\mathcal{R}$ of the cavity can written as [38]

$$\begin{aligned} \mathcal{R} &= \left|\frac{E_{re}}{E_{in}}\right|^2 = \frac{(\kappa - 2\kappa_m)^2 + \Delta_c^2}{\kappa^2 + \Delta_c^2} \\ \mathcal{T} &= \left|\frac{E_{tr}}{E_{in}}\right|^2 = \frac{4\kappa_m^2}{\kappa^2 + \Delta_c^2} \end{aligned} \tag{2.43}$$

E_{in}, E_{re} and E_{tr} are the electric field amplitude of the input, reflected and transmitted light from the cavity respectively. The peak in the transmitted profile and the dip in the reflected profile of a scanning laser input to a cavity is determined by eq.(2.43). Note that both have a Lorenzian profile and the new FWHM of the peak/dip is

$$\Delta\nu = 2\kappa/2\pi \tag{2.44}$$

So the new finesse can be defined as

$$F = FSR/\Delta\nu \tag{2.45}$$

This finesse can be experimentally measured for an empty cavity by measuring the transmitted/ reflected intensity profile for a scanning (in frequency) laser input to the cavity. The frequency difference between two fundamental modes gives the FSR whereas the FWHM of the particular peak measures the $\Delta\nu$. The ratio gives the experimental value of the finesse.

2.6 Atom cavity interaction

In section 2.2 we have discussed the interaction of atom with a classical EM wave. In this section we will discuss the interaction of the atoms with a quantized EM field. Inside the cavity, the EM field that can survive, is determined by the boundary conditions imposed by the mirrors. Here we describe the interaction of the atom with a single quantized EM mode within the cavity.

When an atom is placed within the EM mode of a cavity, the system can be described in terms of three parameters. The photon leak rate from the cavity 2κ (as described in the earlier section), the spontaneous emission decay rate of the atoms into the free space $2\gamma = \Gamma$ and the atom cavity coupling $g(r)$. When the atoms cavity coupling $g(r)$ is larger than the other two loss mechanisms of photons from the cavity, an oscillatory energy exchange takes place between the atoms and the cavity field in a timescale much faster than the lifetime of the photon in the cavity. This regime is called as the *strong coupling regime* and has very interesting features which will be described below.

2.6.1 Single atom interacting with a single EM mode

We consider a single atom interacting with a single mode of the EM field inside the cavity. The system can be described within the Jaynes-Cumming picture. The total Hamiltonian is

$$\hat{H} = \hat{H}_A + \hat{H}_F + \hat{H}_{AF} \tag{2.46}$$

$\hat{H}_A$ is the atomic part of the Hamiltonian is given by eq.(2.1).

$$H_A = \hbar\omega_{eg}|e\rangle\langle e| \tag{2.47}$$

$\hat{H}_F$ is the photon-field part of the Hamiltonian and is given as

$$H_F = \hbar\omega_c\hat{a}^\dagger\hat{a} = \hbar\omega_c\hat{n}_p \tag{2.48}$$

where $a^\dagger$ and a are the photon creation and annihilation operators respectively. $\hat{n}_p$ is the number operator and expectation value of $\hat{n}_p$ gives the number of photons in the cavity mode.

$\hat{H}_{AF}$ is the atom-field interaction Hamiltonian and is given by

$$H_{AF} = -\hat{\vec{\mu}}.\vec{E}(r) \tag{2.49}$$

$\hat{\vec{\mu}}$ being the atomic dipole moment operator [32] and

$$\hat{\vec{\mu}} = \vec{\mu}(\hat{\sigma}^\dagger + \hat{\sigma}) \tag{2.50}$$

where $\vec{\mu}$ is the expectation value of the dipole operator between the atomic states $|e\rangle$ and $|g\rangle$ and is assumed to be real [32]. The single mode of the quantized EM field in the cavity can be written as

$$\vec{E}(r) = E_0\vec{\epsilon}\psi(\vec{r})(\hat{a} + \hat{a}^\dagger) \tag{2.51}$$

$\vec{\epsilon}$ is the polarization direction of the field. $\psi(\vec{r})$ is the spacial profile of the EM mode in the cavity and is determined by the boundary conditions. For TEM_{00} mode the expression for $\psi(\vec{r})$ is given in eq.(2.23). V_{CM} is the effective mode volume of the cavity and given as

$$V_{CM} = \int |\psi(r)|^2 d^3r \tag{2.52}$$

E_0 is the electric field amplitude. Zero point energy of the field mode at resonance frequency ω_c is $\hbar\omega_c/2$. Normalizing the electric field energy $\epsilon_0 {E_0}^2 V_{CM}$ with the zero point energy, we get [33]

$$E_0 = \sqrt{\frac{\hbar\omega_c}{2\epsilon_0 V_{CM}}} \tag{2.53}$$

So the atom-cavity coupling Hamiltonian takes the form of

$$\begin{aligned} H_{AF} &= -\hat{\vec{\mu}}.\vec{E}(r) \\ &= -\hat{\vec{\mu}}.E_0\vec{\epsilon}\psi(r)(\hat{a}+\hat{a}^\dagger) \\ &= \hbar g(r)(\hat{\sigma}+\hat{\sigma}^\dagger)(\hat{a}+\hat{a}^\dagger) \end{aligned} \tag{2.54}$$

where the atom - cavity coupling g(r) is defined as

$$\begin{aligned} g(r) &= -\frac{1}{\hbar}E_0\vec{\mu}.\vec{\epsilon}\psi(r) \\ &= -\sqrt{\frac{\omega_c}{2\hbar\epsilon_0 V_{CM}}}\vec{\mu}.\vec{\epsilon}\psi(r) \\ &= g_0\psi(r) \end{aligned} \tag{2.55}$$

g_0 is the single atom-cavity coupling strength for an atom that is placed on a anti-node at the center of the cavity. From eq.(2.54), by dropping the energy non conserving terms σa and $\sigma^\dagger a^\dagger$, we get the final form of the atom-field coupling Hamiltonian

$$\hat{H}_{AF} = \hbar g(r)(\hat{\sigma}^\dagger a + \hat{\sigma}a^\dagger) \tag{2.56}$$

We further assume that the atom is positioned at the center of the cavity and placed on the antinode EM mode so that position dependence of coupling strength is avoided and $g(r) \to g_0$. The total Hamiltonian then takes the form of

$$\hat{H} = \hbar\omega_{eg}|e\rangle\langle e| + \hbar\omega_c a^\dagger a + \hbar g_0(\hat{\sigma}^\dagger a + \hat{\sigma}a^\dagger) \tag{2.57}$$

This is the famous Jaynes-Cumming Hamiltonian [39] that determines the dynamics of the two level atom-cavity coupled system. The first part of H_{AF} represents absorption of a photon from the cavity mode by the atom which takes it from the ground state to the excited state. The second part represents emission of a photon by the excited atom into the cavity mode, resulting a ground state atom and an extra photon in the cavity mode.

Now we treat the problem in a new Hilbert space which is a product of the atomic and photonic Hilbert space. We define $|g, n_p+1\rangle \equiv |g\rangle \otimes |n_p+1\rangle$ and $|e, n_p\rangle \equiv |e\rangle \otimes |n_p\rangle$ as the dressed states where the atom is in its ground state with n_p+1 photons in the

cavity mode and atom is in its excited state with n_p photons in the cavity mode. The states $|g, n_p + 1\rangle$ and $|e, n_p\rangle$ are the eigenstates of the atomic and photonic Hamiltonian $H_A + H_F$.

$$\begin{aligned}(H_A + H_F)|g, n_p + 1\rangle &= \hbar\omega_c(n_p + 1)|g, n_p + 1\rangle \\ (H_A + H_F)|e, n_p\rangle &= (\hbar\omega_{eg} + \hbar\omega_c n_p)|e, n_p\rangle \end{aligned} \tag{2.58}$$

Clearly the sates $|g, n_p + 1\rangle$ and $|e, n_p\rangle$ are degenerate if $\omega_c = \omega_{eg}$ i.e. the cavity is resonant with the atomic transition. The atom-cavity coupling part of the Hamiltonian lifts the degeneracy of these states and the states $|g, n_p + 1\rangle$ and $|e, n_p\rangle$ are no longer the eigenstates of the total Hamiltonian. The new eigenstates and the eigenenergies can be obtained by diagonalizing the total Hamiltonian [33].

$$\begin{aligned}\hat{H}|E_n^{\pm}\rangle &= \hbar\omega_n^{\pm}|E_n^{\pm}\rangle \\ &= \hbar\left(\frac{\Omega_{n_p}}{2} + \omega_c(n_p + 1/2)\right)|E_n^{\pm}\rangle \end{aligned} \tag{2.59}$$

with,

$$\begin{aligned}\hat{H}|g, 0\rangle &= \frac{\hbar\omega_{eg}}{2}|g, 0\rangle \\ \Omega_{n_p}^2 &= 4{g_0}^2(n_p + 1) + \Delta_c^2 \end{aligned} \tag{2.60}$$

$|g, 0\rangle$ is the lowest state of the system. Ω_{n_p} is the n_p photon Rabi frequency of the oscillation of the system between the new eigenstates which are given as

$$\begin{aligned}|E_n^+\rangle &= sin\theta_{n_p}|e, n_p\rangle + cos\theta_{n_p}|g, n_p + 1\rangle \\ |E_n^-\rangle &= cos\theta_{n_p}|e, n_p\rangle - sin\theta_{n_p}|g, n_p + 1\rangle \end{aligned} \tag{2.61}$$

where,

$$tan\theta_{n_p} = \frac{2g_0\sqrt{n_p + 1}}{\Omega_{n_p} - \Delta_c}$$

The states $|E_n^+\rangle$ and $|E_n^-\rangle$ are called the dressed states. θ_{n_p} is the mixing angle. An elementary excitation of the system in its ground state $|g, 0\rangle$ carries the system to the states $|E_0^+\rangle$ and $|E_0^-\rangle$ separated by $2\Omega_0 = 2g_0$ when $\Delta_c = 0$. The corresponding excitation spectra shows a double peak structure separated by $2g_0$. This phenomena is called

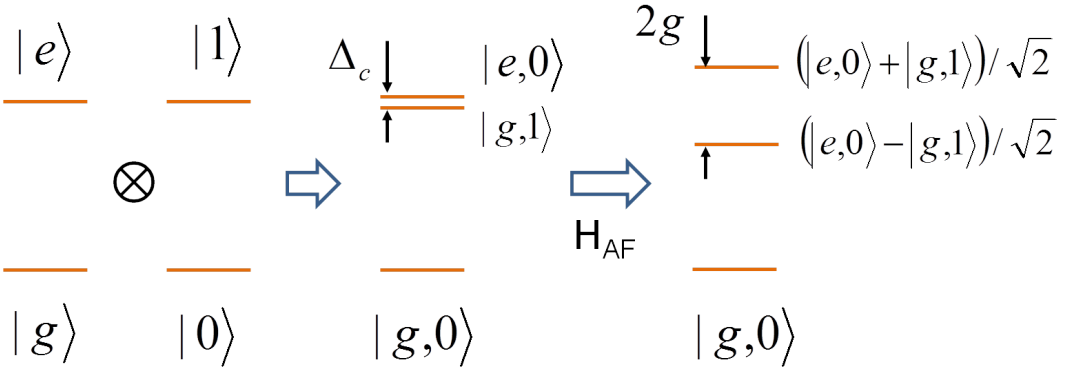

Figure 2.7: The schematic diagram explains the atom-cavity strong coupling in dressed state picture. The states $|e,0\rangle$ and $|g,1\rangle$ are nearly degenerate in absence of the atom-field coupling Hamiltonian H_{AF}. The coupling lifts the degeneracy and the new eigenstates $(|e,0\rangle + |g,1\rangle)/\sqrt{2}$ and $(|e,0\rangle - |g,1\rangle)/\sqrt{2}$ are separated in energy by $2g_0$.

vacuum Rabi splitting or *normal mode splitting*. The new eigenstates are

$$\begin{aligned} |E_0^+\rangle &= \frac{1}{\sqrt{2}}(|e,0\rangle + |g,1\rangle) \\ |E_0^-\rangle &= \frac{1}{\sqrt{2}}(|e,0\rangle - |g,1\rangle) \end{aligned} \tag{2.62}$$

Fig.2.7 schematically explains the splitting of the degenerate states in presence of the coupling. Vacuum Rabi splitting for single two level system strongly coupled to cavity has been demonstrated over a wide variety of system ranging from single atom [40], quantum dot [41] to superconducting qubit [42].

2.6.2 Multiple atoms interacting with a single EM mode

Now we consider the interaction of multiple atoms with a single EM mode of the cavity. This case was studied and the exact solutions were provided by Tavis and Cumming [12, 13]. The Hamiltonian can be written as

$$H_{N_c} = \sum_{j=1}^{N_c} \hbar\omega_{eg}|e_j\rangle\langle e_j| + \hbar\omega_c a^\dagger a + \sum_{j=1}^{N_c} \hbar g_0(\sigma_j^\dagger a + \sigma_j a^\dagger) \tag{2.63}$$

We restrict ourselves within the lowest levels of the system which consists of N_c atoms in its ground state and one photon in the cavity mode. The photon can be absorbed by any one of these N_c atoms going to the excited state, leaving no photon in the field

and remaining $N_c - 1$ atoms in the ground state. The unperturbed states then can be written as

$$\begin{aligned} |g,1\rangle_{N_c} &= |g_1\rangle|g_1\rangle...|g_j\rangle...|g_{N_c}\rangle|1\rangle \\ |e,0\rangle_{N_c} &= \frac{1}{\sqrt{N_c}}\sum_{j=1}^{N_c}|g_1\rangle|g_1\rangle...|e_j\rangle...|g_{N_c}\rangle|0\rangle \end{aligned} \tag{2.64}$$

The coupling part of the Hamiltonian connects these two states and the expectation value can be obtained as

$$\begin{aligned} {}_{N_c}\langle g,1|\, g_0\hbar\sum_{j=1}^{N_c}(\sigma_j^\dagger a + \sigma_j a^\dagger)\,|e,0\rangle_{N_c} &= (\hbar g_0/\sqrt{N_c})\sum_{j=1}^{N_c}\langle g_j,1|\,(\sigma_j^\dagger a + \sigma_j a^\dagger)\,|e_j,0\rangle \\ &= \hbar g_0\sqrt{N_c} = \hbar g_{N_c} \end{aligned} \tag{2.65}$$

So when N_c number of atoms collectively couple to the cavity, the degeneracy is again lifted and the energy separation between the two states are $2\hbar g_{N_c}$ which is reflected in the double peak structure of the emission spectrum. The important thing to notice here is that the collective coupling strength g_{N_c} is $\sqrt{N_c}$ times higher than the single atom coupling strength. So even if in a system the single atom cavity coupling is not large enough to achieve strong coupling, a collective strong coupling can be easily achieved by simply increasing the number of atoms coupled to the cavity mode. In the experiment presented in this thesis we have used this phenomena which will be described later. Collective strong coupling of atoms to a single mode of cavity has been observed in a variety of experimental systems [43–45].

2.6.3 Effect of photon loss

So far we have discussed about the atom- cavity strong coupling in a loss less cavity. The degeneracy of the dressed stated are lifted in presence of a strong coupling which is reflected in a double peak structure of the excitation spectra. Ideally these peaks are delta function. Practically, the photon loss from the cavity leads to broadening of the lines. There are two principle mechanisms for the broadening: the photon loss through the cavity mirrors and the photon loss by spontaneous emission of the atoms into the quasi continuum. The rates for these processes are given by 2κ and 2γ respectively.

The reflection and transmission spectra from of an empty cavity is given in eq.(2.43). In presence of a near resonant medium, the modified reflectivity and transmitivity are given as [38]

$$\begin{aligned} \mathcal{R} &= \left|\frac{E_{re}}{E_{in}}\right|^2 = \frac{(\kappa' - 2\kappa_m)^2 + \Delta_c'^2}{\kappa'^2 + \Delta_c'^2} \\ \mathcal{T} &= \left|\frac{E_{tr}}{E_{in}}\right|^2 = \frac{4\kappa_m^2}{\kappa'^2 + \Delta_c'^2} \end{aligned} \tag{2.66}$$

where the effective detuning Δ' and the modified photon loss rate κ' from the system are given as

$$\begin{aligned} \kappa' &= \kappa + g^2 N_c \frac{\gamma}{\gamma^2 + \Delta^2} \\ \Delta_c' &= \Delta_c - g^2 N_c \frac{\Delta}{\gamma^2 + \Delta^2} \end{aligned} \tag{2.67}$$

Clearly due to the structure of Δ_c' in the denominator, for a large value of g, both reflectivity and transmittivity will have double peak structure now.

2.7 Ion trap

Earnshaw's theorem states that "A charged particle can not be maintained in stable equilibrium solely by electrostatic forces". However techniques exist to confine charged particles without violating Earnshaw's theorem. For example, a Paul trap [46] uses time varying electric field in combination with a DC electrostatic field to dynamically trap the ions in space. A Penning [47, 48] trap uses an axial magnetic field superposed on a quadrupole electric field to trap the ions. In our experiment we have designed our ion trap based on a quadrupole Paul trap geometry. Below we provide a basic understanding of the working principle of a quadrupole Paul trap.

2.7.1 Paul trap

An ideal Paul trap consist of a ring with a hyperbolic inner surface and a pair of endcaps. A combination of an oscillating electric field on the ring and a DC electric field on

the endcap electrodes provides the confining potential. Electric field of peak voltage V_0, oscillating at radio frequency $\Omega_{rf} = 2\pi\nu_{rf}$ in combination with the DC field U_0 on the endcaps creates the trapping potential of the form [10]

$$\begin{aligned} \phi(x,y,z) &= \frac{U_0 + V_0 cos\Omega_{rf} t}{2d_0^2}(2z^2 - x^2 - y^2), \quad (2.68) \\ d_0 &= \sqrt{\frac{r_0^2}{2} + z_0^2} \quad (2.69) \end{aligned}$$

where r_0 is the smallest inner radius of the ring electrode and $2z_0$ is the minimum separation of the endcaps. In practice, for traps with non-hyperbolic electrodes, r_0 and z_0 defines the distance from the center of the trap upto which the form of the potential is pure quadrupolar. The equation of motion of a particle of charge Q and mass m_{Ion} in the potential is then

$$\begin{aligned} \ddot{x} - \frac{Q}{m_{ion}d_0^2}(U_0 + V_0 cos\Omega_{rf} t)x &= 0 \\ \ddot{y} - \frac{Q}{m_{ion}d_0^2}(U_0 + V_0 cos\Omega_{rf} t)y &= 0 \\ \ddot{z} + \frac{2Q}{m_{ion}d_0^2}(U_0 + V_0 cos\Omega_{rf} t)x &= 0 \quad (2.70) \end{aligned}$$

we use the notation u_i for the spatial coordinates so that $u_1 = x$, $u_2 = y$ and $u_3 = z$. We also define the parameters

$$\begin{aligned} a_x = a_y &= -\frac{4QU_0}{m_{Ion}d_0^2\Omega_{rf}^2} \\ q_x = q_y &= \frac{2QV_0}{m_{Ion}d_0^2\Omega_{rf}^2} \\ a_z &= \frac{8QU_0}{m_{Ion}d_0^2\Omega_{rf}^2} \\ q_z &= -\frac{4QV_0}{m_{Ion}d_0^2\Omega_{rf}^2} \\ \tau &= \frac{\Omega_{rf} t}{2} \quad (2.71) \end{aligned}$$

In terms of these dimensionless parameters the ion equation of motion can be reduced to three uncoupled Mathieu type differential equations.

$$\frac{d^2u_j}{d\tau^2} + \left(a_j - 2q_j cos(2\tau)\right) u_j = 0, j = 1,2,3 \quad (2.72)$$

Depending on the combination of the parameters a_j and q_j these equations have stable, bounded or unstable, unbounded solutions. The region in which the combination of a_j and q_j provides a stable solution is called the "stability region" of the trap.
The stable solution of the Mathieu equation is of the form [49]

$$u(\tau) = \eta(\tau)e^{\mu\tau} \tag{2.73}$$

where $\eta(\tau)$ is a π periodic function and represents the rapid oscillation of the ion inside the trap, namely micromotion, driven by the trapping RF field. The other term represents the slower secular motion of the ion in the trap under the time averaged trapping potential. μ is a parameter that depends on a and q. For an ideal Paul trap, the secular motion resonance frequencies are given by

$$\omega_{j,n} = (n + \beta_j/2)\Omega_{rf} \tag{2.74}$$

where n is the order of the resonance. The fundamental resonance frequency is at $n = 0$. Under adiabatic approximation ($a, q << 1$) the parameter β can be approximated as [10]

$$\beta^2 \approx a + q^2/2 \tag{2.75}$$

2.7.2 Modified spherical Paul trap

In our experiment we have used the basic geometry of a quadrupole Paul trap and modified the geometry according to the experimental needs and geometrical constraints. The electrodes consist of four thin tungsten wires wound in square shape geometry. An RF voltage in the inner pair of wires in combination with a DC voltage on the outer pair of wire provides the trapping potential. Because of the non-standard geometry, the potential can not be fitted with a pure quadrupolar form. As a result, analytical solution of the Mathiew equation is not possible. Hence in our study of the ion trap, most of the parameters of the ion trap are determined either experimentally or from simulation

where the equation of motion of the ion is solved numerically in the exact potential due to all the electrodes present in the setup. Near the trap center the potential can be approximated to be harmonic so that the ions can be trapped. As one goes away from the center, the anharmonicity increases. If an ion encounters the anharmonic part of the potential, it gets immediately ejected out of the trap. Fig.2.8 shows the projection of the secular motion and micromotion of a trapped $^{85}Rb^{+}$ ion.

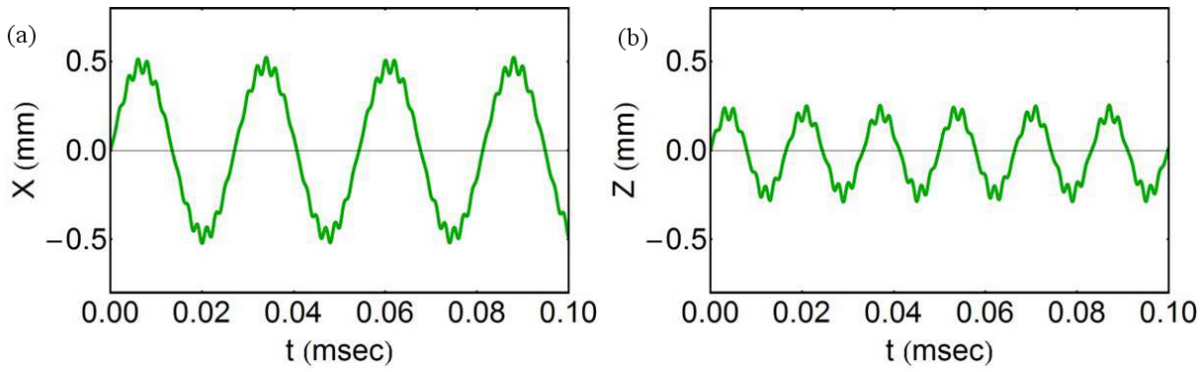

Figure 2.8: The projection of the motion of the ion on the x axis (a) and z axis (b) in our trap is shown. The lower frequency secular motion is modulated by the higher frequency micromotion.

2.8 Discussion

In this chapter we have discussed in detail the underlying physics of the experiments described in this thesis. We have discussed about the cooling and trapping of atoms, the fundamentals of Fabry-Perot cavity, strong coupling of the atomic ensemble with the cavity mode and finally the basic physics of quadrupole Paul trap. The understanding of the systems allows us to design and built the hybrid apparatus that combines these techniques and perform the experiments in a comprehensive way.

CHAPTER **3**

The experimental apparatus

3.1 Overview

The hybrid apparatus that enables simultaneous and spatially overlapped trapping of atoms, ions and molecules within a Fabry-Perot cavity, relies on various crucial established techniques described in the prervious chapter. In this chapter we will discuss in detail the design and construction of the apparatus. The diverse experimental needs and geometrical constraints arising from the symmetry of the individual traps make this a very involved and complicated process. We first explain the requirements and constraints of the design and then describe step by step the construction and assembling of the apparatus. Finally we provide the details of the lasers and the optical arrangement that has been used for the experiments described in this thesis.

3.2 Requirements of the apparatus

3.2.1 Experimental requirements

The primary experimental requirement of the apparatus is to have spatially overlapping traps of the atoms, ions and molecules, which can be operated simultaneously, minimally effecting each others performances, yet allowing the species to interact. Below we discuss the points we have considered for designing the hybrid apparatus.

Combination of ion trap and MOT

A magneto optical trap (MOT) simultaneously traps and cools atomic ensemble. The cooling is done by momentum transfer from photons to atoms as discussed in chapter 2. Three counter-propagating pairs of orthogonal red detuned laser beams cools the

atomic ensemble in all six directions whereas a gradient magnetic field from a pair of anti-Helmholtz coil, combined with the laser beams (Fig.3.1), provide the position dependent force which cools and localize the atoms.

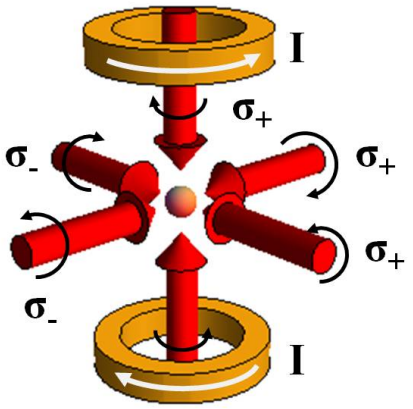

Figure 3.1: The schematic of an experimental arrangement for MOT. Three orthogonal pairs of counter-propagating beams of opposite circular polarization, with the gradient magnetic field provided by the pair of coils in anti-Helmholtz configuration, cools and localize the atomic ensemble at the intersection of the beams.

For trapping ions, the two most widely used techniques are *Penning trap* and *Paul Trap*. A Penning trap uses a combination of DC electric field and a magnetic field to confine the motion of ions in radial and axial directions. The typical magnetic field used for a Penning trap is few Tesla whereas the magnetic field gradient required for a MOT is few tens of Gauss/cm. The field of a Penning trap would cause non-linearities in the Zeeman shift of the atoms and is therefore unsuitable for ion traps which are to be combined with a MOT. In a Paul trap, the motion of the ion is confined using a combination of RF and a DC voltage at the endcaps which makes it a better choice for a hybrid trap. At the time of designing this instrument, it was already shown that the relatively weak magnetic field gradient used for MOT do not visibly effect the performance of the Paul trap [4]. In our experiment we use $\sim$ 22 Gauss/cm of

magnetic field gradient for the MOT and $\sim$ 80 V, 500 kHz of RF for the Paul trap.

MOT in a cavity

The cooling and localization of atomic ensemble in MOT relies on the fact that the spontaneous emission of the photons from the atoms have no preferred direction and hence happens at all 4π directions with equal probability. A presence of a near resonant cavity around changes the rate of emission in the direction of the cavity. In a very high finesse cavity this change of scattering rate can result in significant perturbation in the MOT, resulting in its destruction. We choose a moderate finesse Fabry-Perot cavity (finesse $\sim$ 2400) so that the formation of the MOT is not compromised yet a collective strong coupling can be achieved. The moderate finesse also allows to develop enough intra-cavity intensity. This situation allows one to use the cavity as versatile tool for resonant or off-resonant interrogation of the species within.

Creation and trapping of molecules

Direct laser cooling of diatomic molecules is challenging and no general prescription exist due to absence of closed transition and closely spaced large number of energy levels. So one usually creates cold diatomic molecules from cold atomic ensemble. Photoassociation and the utilization of a Feshbach resonance are two popular techniques. The Feshbach resonance technique often requires high magnetic field which does not allow coexistence of a MOT as a source of atoms. In our experiment we choose Photoassociation, which requires only far red detuned (few tens of GHz) intense laser light, as the technique for production of cold diatomic molecules. Trapping of neutral molecules is another challenging task. The cavity allows us to think about the possibility of creation and trapping (by optical dipole force) of molecules within the mode. Multispecies experiment provides the opportunity of creating polar molecules which can be electrostatically or dipole trapped. But in that case the ion trap can not be operated simultaneously.

3.2.2 Practical constraints for combining the trap

Every trap comes with its own geometry and symmetry. While designing a hybrid apparatus, we have to take care to maintain the symmetries of the corresponding traps and combine them. Another requirement is to have large optical access to the center of the trapping region. MOT itself requires 3 orthogonal pairs of beams for formation. Every type of optical interrogation or light collection requires optical access. Furthermore the cavity requires an input and an output optical port. The last, but not the least, one requires enough feed-through for electrical connections. The connecting conductors must be positioned such that they do not interfere with the operation of the trap. Altogether the challenge in designing lies in combining the traps with their natural geometric symmetries, with large optical access to the center and accommodating enough feedthrough with minimal stray field.

In principle, all the experiments described so far would also be possible with a segmented linear Paul trap with an axial cavity. But the problem lies in axial extraction of the ions for detection due to presence of the cavity mirrors. To solve this problem we have designed and constructed a Modified Spherical Paul trap (MSIT) in which the electrodes consist of thin tungsten wires of 80μm diameter. The ions can be radially extracted onto a CEM for detection. Further the same electrodes can be used to apply high DC electric fields or gradient electric fields for alignment or trapping of polar molecules [50]. So one needs the electrodes to be close to the center to obtain high electric field at the center, but without obstructing the MOT laser beams. Hence the choice of thin wires which do not create significant shadow at the trapping region. Also one gets large optical access to the center. Tungsten can also withstand very high energy of laser pulse making it the choice of element for electrode in our experiment. The whole experimental design resulted in a spherical hexadecagon vacuum chamber with 16 radial and 2 axial viewports that allows enough optical and electrical access.

Below we describe in detail the designing and building of the apparatus step by

step.

3.3 The Vacuum system

3.3.1 The main chamber

The core of the apparatus is situated inside a stainless steel (SS304) spherical hexadecagon chamber (Kimball physics Inc: MCF600-SphHexadecagon-F2A16). A schematic of the core is given in Fig.3.2 and Fig.3.3. The chamber has 16 CF16 and 2 CF100 ports, which allows sufficient optical and electrical access. The central electrode assembly has 4 stainless steel rods of 3 mm diameter held in a quadrupolar configuration, with center to center distance of 17 mm. The rod assembly is arranged symmetrically about the chamber diameter that runs through the center of two of the 16, CF16 ports of the chamber. The rods are electrically isolated as well as mechanically supported by two Macor®(machinable ceramic) plates of 3mm and 6mm thickness. The plates are 32 mm in diameter and has a central hole of 7.7 mm diameter for optical access to the cavity whose mirrors are mounted symmetrically on the Macor®support. A semi-circular section is cut off from the sides of the plates so that the laser beams for the MOT can pass through without any obstruction. Two highly reflective concave mirrors are used to form the Fabry-Perot cavity. The mirrors are 12.5 mm in diameter and 6 mm thick. The concave surface has radius of 50 mm. On the thicker plate, one of the cavity mirrors is fixed, by means of Torrseal, such that the concave side is facing the center of the chamber. On the other plate, a 3 mm thick ring piezoelectric transducer (pzt) is first attached so that the pzt is concentric with the hole in the plate. Then the other cavity mirror is attached on the pzt with TorrSeal. The highly reflective concave surfaces, facing each other, forms the Fabry-Perot cavity. The pzt can be used to scan the length of the cavity by several FSR of the cavity.

The Macor plates are attached to the chamber wall by means of groove-grabbers (Kimball Physics: MCF600-GrvGrb-C01). Each plate is attached to a pair of stainless steel (SS) groove-grabber (top and bottom) by means of four screws. With two of the

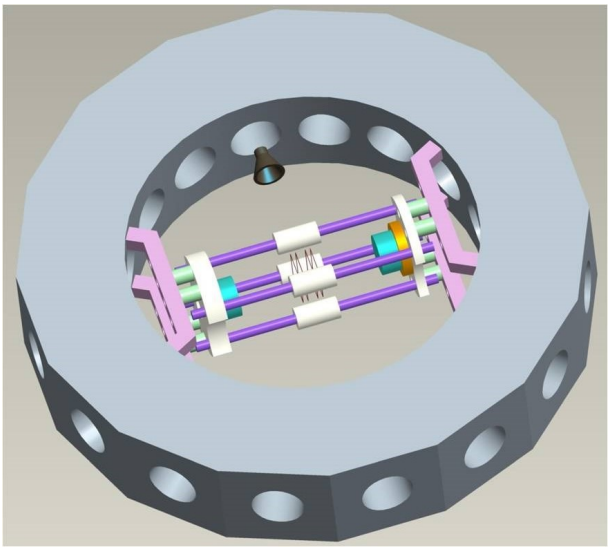

Figure 3.2: The main chamber (False colored): A 3D impression of the main chamber of the apparatus. The four-wire ion trap is shown wound around the white ceramic sleeves. The mirrors (blue) forming the Fabry-Perot cavity are attached to the Macor plates (white) of pzt (golden) which are then mounted on the chamber by means of groove grabber (pink). The SS rods (violet) provides support to the structure as well as used for ion extraction. The CEM (black) for the detection of the extracted ions is also shown.

screws, SS spacers are used to define the position of the Macor plates w.r.t. the chamber wall. The other two screws are used without spacers so that they can be used to provide a slight tilt, if required for the cavity alignment, to the mirror attached to the plate.

Periodically grooved Macor sleeves are attached to the SS rods at the center of the chamber. The 'v' shaped grooves are 100μm in depth and are placed 1.5mm apart. Around these sleeves, four 80μm tungsten wires are tightly wound in identical square configuration, separated by 1.5 mm, 3 mm and 1.5 mm respectively. The wires goes into the grooves and sits firmly so that the square structure does not distort with time. These four wires forms the modified spherical Paul trap for the apparatus. Another set of Macor sleeves are attached to the SS rods in front of the 3mm Macor plate. A pair of 80μm tungsten wires are wound around these sleeves. The first wire is wound in square configuration, similar to that of the ion trap. The second wire is wound in a criss-crossed configuration. The wires are placed at a distance 11 mm and 12.5 mm

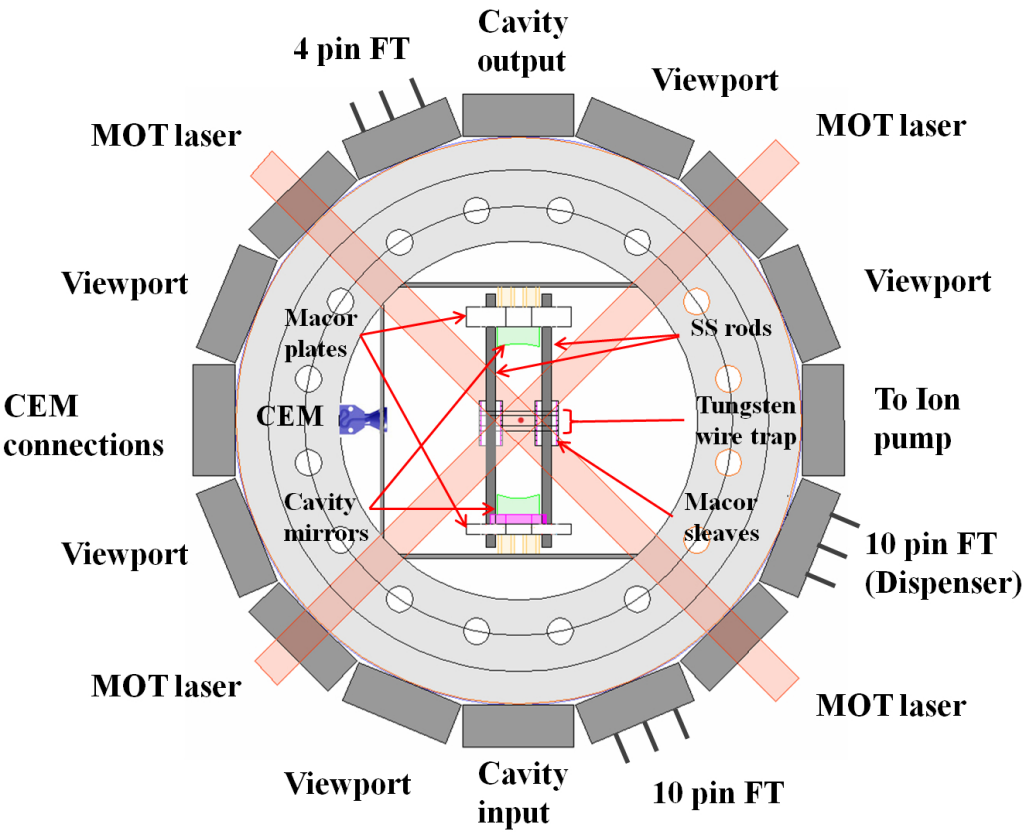

Figure 3.3: The main chamber: Top view of the main chamber. Crucial components are marked.

respectively from the 3 mm Macor plate. Details of the wire winding geometry are discussed later in this chapter. These wires protect the ion trap from the pzt voltage and plays crucial role in ion extraction process as will be discussed later.

Feedthroughs and electrical connections

There are two 10 pin (Kurt J Lesker, 2 kV, 10 A) and one 4 pin (Kurt J Lesker, 5 kV, 15 A) electrical feed-through (FT) directly attached to the chamber as can be seen in Fig.3.3. The 4 pin FT is used to provide electrical connections to the electrodes as well as to the pzt. The pins of the FT are separated using hollow glass beads. The electrodes are connected to the FT using bare copper wires. One side of a set of 1.5 mm thick copper wires are flattened using a hydraulic press and a tiny hole is drilled through. A M1.6 screw can go through the hole. These wires are used to carry the electrical connections

very near to the MSIT and then the tungsten wires are attached to it using the M1.6 nuts and bolts. The specialty of the copper wires are that they are flexible enough to bent arbitrarily but rigid enough to carry its own weight without any support. Also bare copper has reasonable UHV property, which makes it an ideal choice to use for electrical connections inside the chamber. The copper wires providing connections to the MSIT, are bent and placed in the shadow region behind the SS rods in such a manner that the voltage applied on them are screened from the trap by the SS rods. A set of specially designed copper beads are used to attach the copper wires to the FT. The copper beads have an off-axis through hole along with two radially threaded M2 holes on two end to connect the FT and the copper wires on two ends. It is also slotted axially to provide air-relief. The slots are also used to attach the dispensers which sources the atoms for our experiments.
Detail of the mechanical drawings of the crucial components of the apparatus are provided in the appendix.

Metal vapor dispensers

The apparatus is designed for the study of multi-species interactions. Naturally one requires sources of the corresponding metal vapors to be inside the chamber. As a source of metal vapors, we use dispensers that contains alkali metal salt. When heated, usually by passing few Amps of current through it, metal vapor is emitted out of the dispenser. In our apparatus we have used one 10 pin FT to connect 6 of these metal vapor dispensers. The copper beads with slots, mentioned earlier, were used to attach the dispensers directly onto the FT. The dispensers are mounted in such a way that the opening slot is facing towards the central trapping region. A list of the dispensers mounted are given in Table 3.1.

3.3.2 Channel Electron Multiplier

A channel electron multiplier (CEM) is used as an ion detector in this experiment. The CEM (Dr. Sjuts: KBL10RS) has a opening cone of 10 mm diameter for accepting the

Table 3.1: List of alkali metal vapor dispensers installed.

Species	Isotopes	Make	Number
Rubidium	$^{85}Rb(72.2\%), ^{87}Rb(27.8\%)$	Saes	2
Potassium	$^{40}K(8.4\%), ^{39}K$	Alvatec	2
Cesium	^{133}Cs	Saes	1
Calcium	$^{40}Ca(99.9\%)$	Alvatec	1

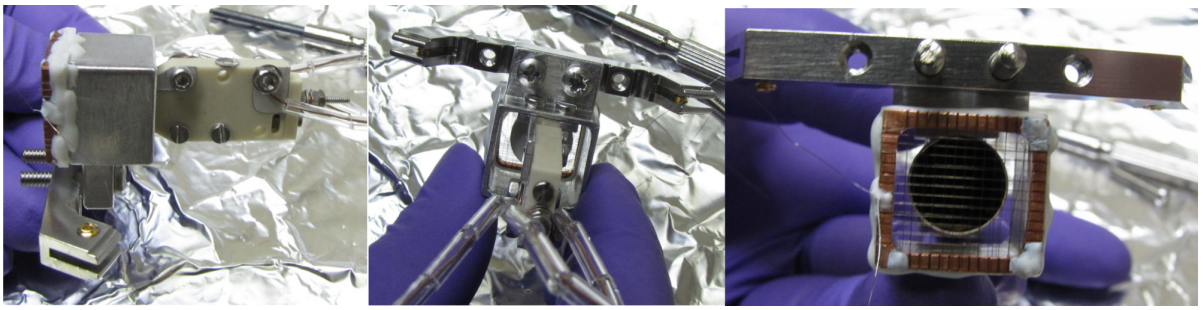

Figure 3.4: Mounted CEM: Side, back and front view of the CEM mounted in the aluminum box with the shielding grid in front is shown.

ions. It is mounted 44 mm away (cone position) from the trap center, facing the trap, transverse to the cavity axis, in front of a CF16 viewport (Fig.3.3). The CEM is housed in a grounded aluminum box to shield the field due to the high voltage applied on it. Also a homemade copper wire mesh is mounted on the aluminum box, in front of the CEM cone to protect the ion trap from the high voltage on the CEM cone. The CEM with the aluminum box and the grid is shown in Fig.3.4 . The aluminum housing along with the mesh is mounted on the chamber wall by means of a groove grabber. A 4 pin FT is attached to a CF40 - CF16 conical reducer nipple and the nipple is attached to the port. Bare copper wires, insulated by glass beads, are used to provide electrical connections from the FT to the CEM.

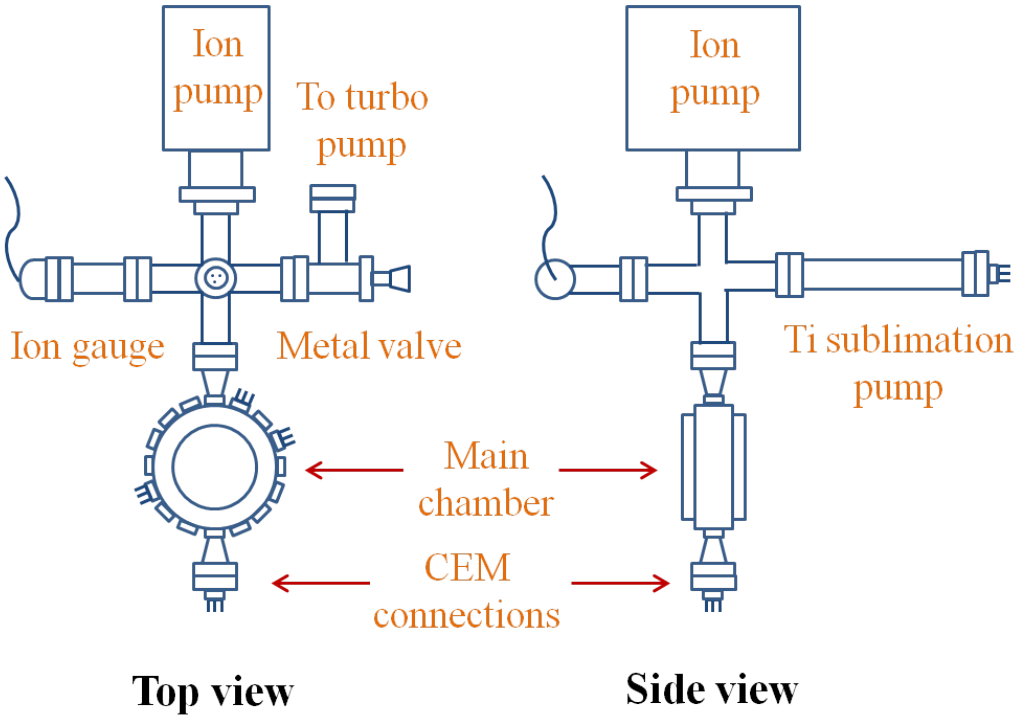

Figure 3.5: The vacuum system The image shows side and top view of the assembled vacuum system.

3.3.3 Pumps and Gauge

The chamber, along with the conical nipple for the CEM, is attached with a CF40 four way cross using another conical reducer nipple of similar dimensions. The arm opposite to the chamber is connected with a ion pump using a CF600 - CF40 zero length reducer flange. The ion pump is from Varian (VacIon Plus 919-1210) and has 40 l/s pumping speed. A titanium sublimation pump, contained within a CF40 flanged tube, is attached with the the top arm of the cross. The bottom arm of the cross is further attached with a CF 40 'T' section. One arm of the 'T' section contains a ion gauge (Varian: UHV-24) for measuring the pressure inside the apparatus. On the other arm, an all metal valve is attached which can connect or disconnect the apparatus with a turbo molecular pump (Pfeiffer: TMU 071). A schematic of the assembled system is shown in Fig.3.5.

3.4 The assembling process

3.4.1 Making and aligning the Fabry-Perot cavity

The Fabry-Perot cavity is the most alignment sensitive part of the instrument. Also the axis of the cavity should go through the center of the chamber and hence the center of the hybrid trap. Thus it requires utmost care in assembling and alignment. In the following we describe the step by step procedure of assembling it.

At first the cavity mirrors and the pzt are stuck to the Macor plates as described in section 3.2.1. The pzt is vacuum compatible. But the connecting wires are coated with Teflon, which is not. So the wires are carefully stripped off the Teflon. A dab of Torrseal is applied on the connecting point of the wire and the pzt to ensure durability of the connection. It also covers the surface of the connecting point to prevent any emission which is not good for vacuum.

A laser, at 780 nm, from a Toptica DL100 laser system is used for the cavity alignment. The spatial profile of the laser beam is cleaned up by passing it through a single mode polarization maintaining (SMPM) fiber. We use a small focal length output coupler to get a small output beam diameter which illuminates only a small part of the cavity mirror. The chamber is mounted horizontally 30 cm above the optical table. Two Teflon caps, with 1mm hole at the center, are fitted tightly on two opposite CF16 viewports of the chamber. The reference laser beam coming out of the fiber is carefully aligned, by means of two beam steering mirrors, to pass through the tiny holes of the Teflon caps. In this process we make the reference beam coincident with the diameter of the chamber, and therefore ensure passage through the center. Now we have to build the cavity w.r.t this reference beam so that the mode of the cavity will pass through the trap center. A pair of apertures are installed outside the chamber on the reference beam path.

The mirror attached with the 6mm Macor plate is chosen as the rear mirror. The plate is mounted on the chamber wall, in front the CF16 viewport, using the SS spacers and groove grabbers. The plate is positioned such a way that the reference beam is

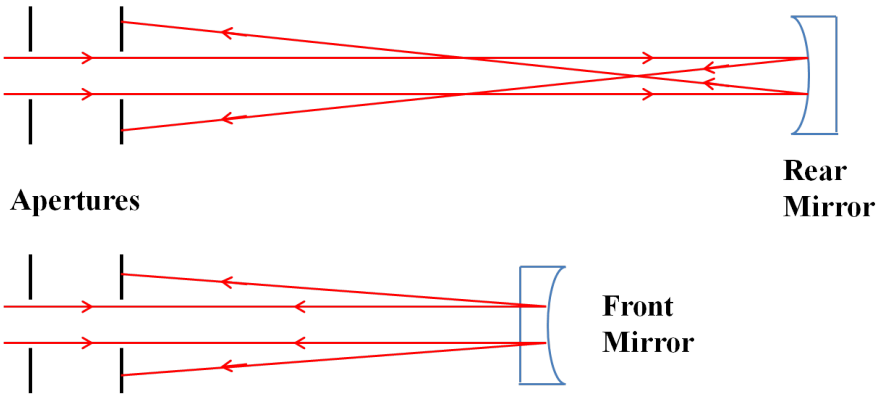

Figure 3.6: Cavity mirror alignment principle: The image shows the laser beam reflected from the front and the rear mirrors of the cavity and its impression on a pair of apertures positioned on the path of the incoming beam.

incident more or less at the center of the concave surface. The reflection of the beam from the concave surface will first focus within the chamber and then diverge and propagate out of the chamber (Fig.3.6). The projection of the beam can be seen on the aperture. The mirror is finely aligned, using the screws attaching the Macor plate to the groove-grabber, so that the diverging beam is centered around both the apertures. The plate is rigidly fixed in this position. Now we install the front mirror, along with the pzt, in a similar way, facing the rear mirror. The four SS rod along with the Macor sleeves, are secured in a manner which allows some play at the time of connecting the macor plates. The reference beam will have two reflections from this mirror as can be seen in Fig3.6. The reflection from the flat surface does not diverge and has the same spot size as the incident beam. The reflection from the convex side (back side of the concave plane) will diverge when propagating post reflection. The plate is aligned, again using the screws attaching the Macor plate to the groove grabber, in such a way that the reflection from the flat surface goes through both the apertures and the diverging reflected beam from the convex surface is concentric with the apertures. The Macor plate is rigidly tightened in this position and also the threads at the ends of the four SS rods are gently tightened to provide a rigid mechanical coupling between the two mirrors. This process ensures primary gross alignment of the cavity mirrors.

For finer alignment of the cavity, the beam coming out of the cavity through the

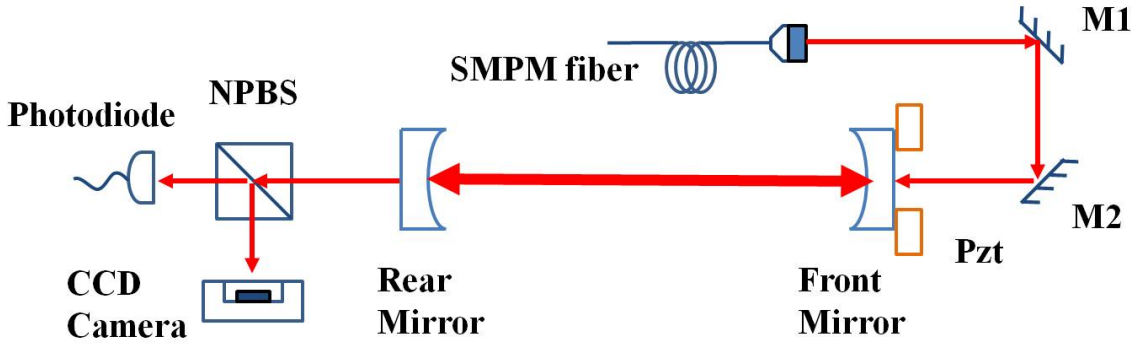

Figure 3.7: Cavity alignment setup: The image shows setup for the cavity alignment. A Gaussian shaped and collimated laser beam out of a SMPMF, scanning in frequency, is incident on the cavity using two beam steering mirrors. The output of the cavity is divided in two parts. One part is imaged on the CCD while the other part falls on a photodiode to measure the intensity.

rear mirror is monitored while the laser is scanning in frequency. The beam is divided using a non-polarizing beam splitter (NPBS) as shown in Fig.3.7. One part is picked up by a photodiode and is monitored at a oscilloscope triggered by the laser scan. The other part falls on a CCD camera to monitor the spatial profile of the mode. In the camera, two bright spots originating from two mirrors can be seen. When the primary alignment is done carefully, these two spots merge and gives rise to a bright single spot. Several TEM spatial profiles (zeroth and higher orders), with visible distortion, can be observed on the camera while the reference laser is scanning. Now the rear mirror tilt is slightly adjusted, using the screws without the spacers, to get a radially symmetric spatial profile of the beam. An iterative alignment is performed, using these two screws, to ensure a good overlap of the spots as well as a radially symmetric beam profile. When this condition is satisfied, a series of narrow peaks can be observed on the photodiode signal, corresponding to the cavity resonances. A mode matching lens (100 mm focal length, plano-convex) is placed outside the chamber, at a distance 100 mm from the center of the cavity. The lens is placed on a 3D translation stage. The position of the lens is again adjusted by monitoring the spatial profile of the outcoupled beam for radial symmetry. After successful mode matching, the relative strength on

the TEM_{00} mode increase significantly while the other higher order modes becomes weaker.

3.4.2 Winding the ion trap

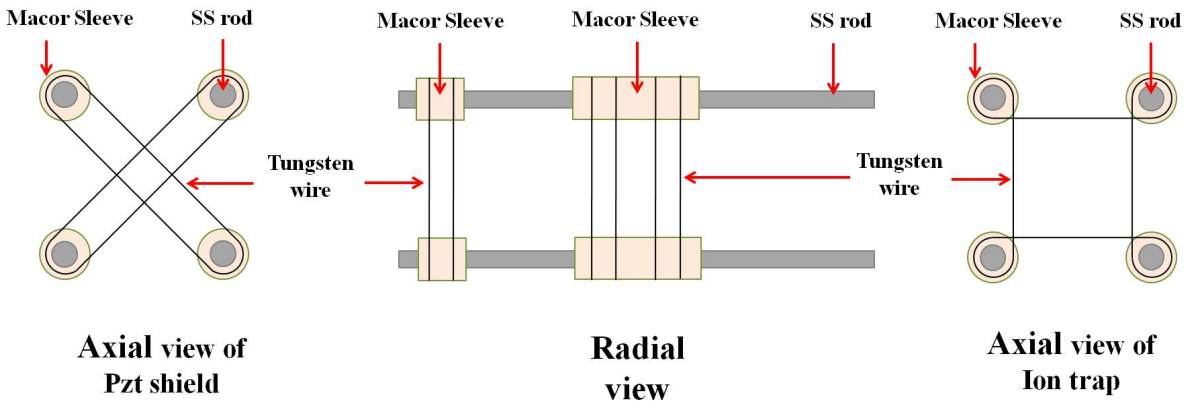

Figure 3.8: The schematic of the thin wire ion trap and the pzt shield: The image shows the radial and axial view of the winding of the thin wire trap and the pzt shield.

The ion trap is constructed by winding 80μm tungsten wires, in square shape, around the Macor sleeves as shown in Fig.3.8. The high elastic limit of tungsten and fragility due to minimum thickness of the wire makes the winding and the connection a difficult and delicate job. At first a mm graph paper is installed at the bottom of the chamber as a reference. It is made sure that the SS rods are parallel to each other and positioned correctly. The macor sleeves are stuck on the SS rod using Torrseal such that the four grooves, on which the wires will be wound, are placed symmetrically around the center. Once the Torrseal is dried, we start the winding. The wire is first threaded into a needle. Then, starting from one corner, the wire is wound in square shape around all the four sleeves so that it comes back to the sleeve we started from (Fig.3.9). The front and back end is then pigtailed gently on the groove. A dab of Torrseal is applied on the pigtailed part to prevent unwinding from mechanical strain. All the four squares are wound in this way starting from one side. The open ends are now connected to the one side flattened copper connectors using M2 nuts and bolts. The grid in front of the pzt is also wound in a similar way. But this time the winding

is criss-crossed geometry to shield the pzt voltage. The process of winding may cause some deformation in the cavity. So the cavity fine tuned once again by adjusting the rear mirror angle and monitoring the radial symmetry. At the end, the CEM with the housing and wire mesh is installed as described in section 3.3.2.

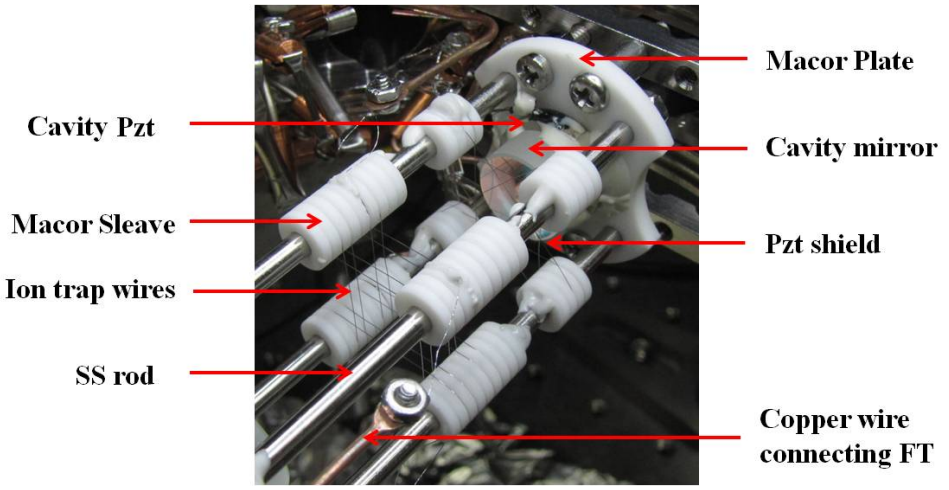

Figure 3.9: The thin wire ion trap: The image shows the thin wire trap after winding and connection. The pzt voltage shield electrode is also shown.

3.5 Bakeout and achieving UHV

After the mounting process is complete, all the CF 16 viewports as well as the top and bottom CF 100 viewports are closed using torque wrench. The sealed chamber is now attached with the remaining part of the vacuum system, which is already built on the table, as shown in Fig.3.5. For achieving UHV, at first step we run the turbo pump for a week and achieved $\sim 3 \times 10^{-8}$ mBar of pressure. After this a very slow and low temperature bake-out of the whole system is performed by wrapping it with heating tape and aluminum foil. The temperature was raised to $\sim$ 110 degree centigrade over 24 hours, held at that temperature for 48 hours and then slowly lowered to the room temperature for 24 hours. This allows the surface adsorbed water vapor to be pumped out. Thermocouple sensors were attached at different parts of the system to ensure a uniform temperature across the entire vacuum system. The slow bakeout was required

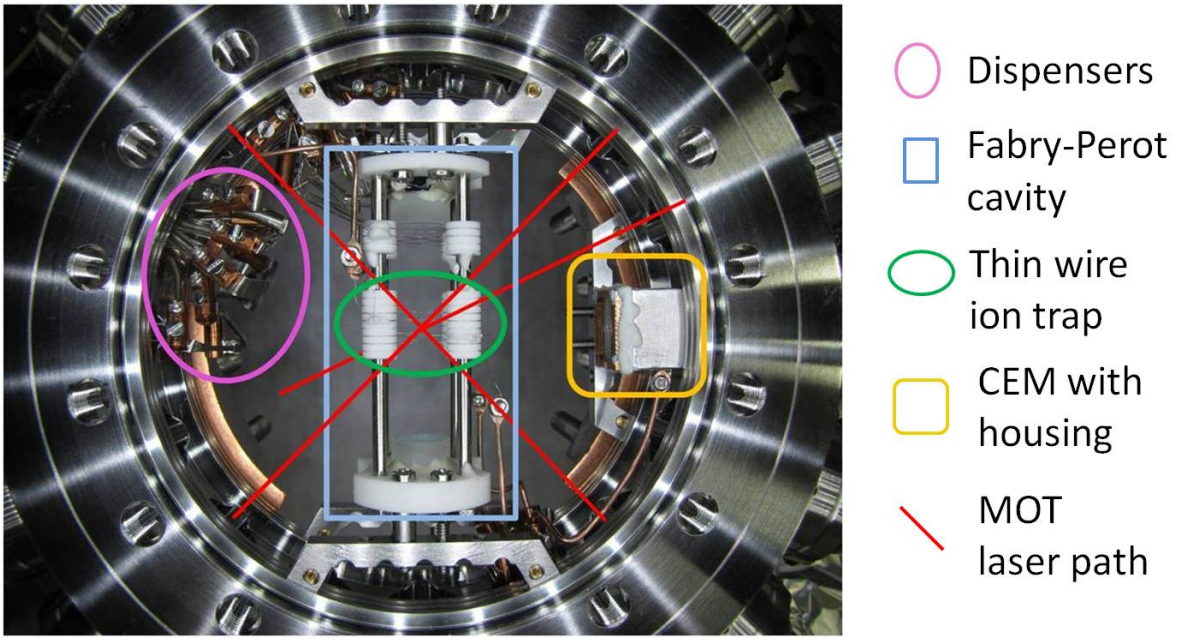

Figure 3.10: The assembled main chamber: A photograph of the main chamber with all the components mounted is shown. The crucial parts are marked.

to prevent any misalignment of the cavity and the wire trap. During the lowering of the temperature, we start the ion pump and in the end, the Ti-Sublimation pump was fired with 50 Amp, for 30 seconds. In this process, we achieved a vacuum of 5×10^{-11} mBar.

3.6 Magnetic coils

We use a pair of coils in anti-Helmholtz configuration to create the gradient magnetic field required for the MOT. The coils are 40 mm in diameter and has 100 turns each. The coils are wound using 1.2 mm copper wire around a copper former. The copper formers with the coils are mounted on brass plates, which sit on the CF 100 viewports of the chamber. Both the copper structures and the brass plates are slotted to prevent the flow of eddy current. In our experiment we pass 5 Amps of current through the coils to obtain a magnetic field gradient of 22 G/cm at the center of the trap. At the bottom of each coil, a set of 8 ultraviolet LEDs, in an annular printed circuit board (PCB) is attached. The PCB is insulated from the copper coil by thin annular strip

of Teflon. The PCB, mounted on the coil structure with the brass plate is shown in Fig.3.11(a). The LEDs can be used to perform light induced atomic disorption (LIAD) of the Rb atoms physisorbed on the glass surface. This is useful to cleanup the glass surfaces, especially the reflecting surface of the cavity mirrors, at regular intervals. LIAD can also be used to create low velocity atomic vapor in the chamber, from which the MOT can be loaded. The spectral profile of the LED is shown in Fig.3.11(b)

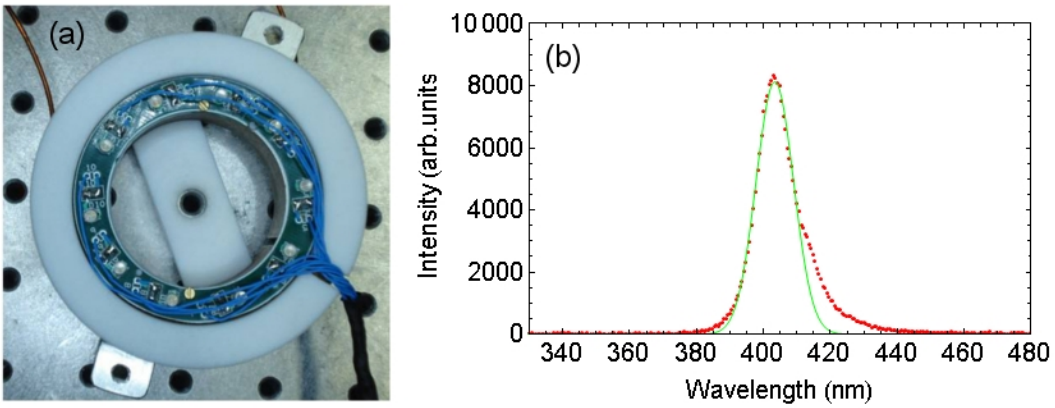

Figure 3.11: (a) The UV LED s mounted at the bottom of a magnetic coil is shown. The removable Teflon piece attached at the center of the coil is used to align the MOT laser beams w.r.t. the coils. (b) The experimentally measured spectral profile (red dots) of the LED . A Gaussian fit (green line) on the regular part of the data yields a central wavelength of 403.4 nm and FWHM of 13.2 nm.

3.7 Lasers

For the experiments performed for the work of this thesis, we have used four external cavity diode lasers (ECDL) [51]. Detail of the design of these homebuilt ECDL can be found in ref. [52]. In the following we describe the detailed optical arrangement of these lasers.

3.7.1 Cooling laser

The cooling laser is a home-built ECDL with a Thorlabs:DL7140 laser diode installed. The temperature, current and the cavity length is tuned so that it scans across ^{85}Rb

$5S_{1/2}\ (F = 3) \leftrightarrow 5P_{3/2}$ atomic transition. The laser can be actively stabilized (locked) to a frequency, red detuned to the $5S_{1/2}\ (F = 3) \leftrightarrow 5P_{3/2}\ (F' = 4)$ transition, using a PID and Pound-Drever-Hall (PDH) combination.

The detail of the optical arrangement is given in Fig.3.12(a). The light out of the laser is first shaped using an anamorphic prism pair and then passed through a 40 dB isolator to prevent optical feedback to the laser. Post isolator, the beam is divided into two parts. One part is frequency shifted for red detuned locking of the laser using a pair of AOMs. The frequency of the laser, before and after the frequency shifting, is monitored using saturation absorption spectroscopy (SAS) setup. The first AOM, A1(Isomet:1206C), shifts the frequency by 2×110 MHz in double pass in +1st order. The second AOM, A2(Isomet:1205C), shifts the frequency by -2×90 MHz in double pass in -1st order. So in combination, these two AOM provides a frequency shift of $+50$MHz. In this process, the 1st cross over of the frequency shifted SAS lies $\sim$ 12 MHz red detuned w.r.t the unshifted $5S_{1/2}\ (F = 3) \leftrightarrow 5P_{3/2}\ (F' = 4)$ peak which is the cooling transition. Hence locking the laser on the first crossover of the shifted SAS ensures the cooling laser to be locked at a frequency $\sim$ 12 MHz red detuned w.r.t the $5S_{1/2}\ (F = 3) \leftrightarrow 5P_{3/2}\ (F' = 4)$ closed transition.

The other part of the beam with the bulk of the laser power is injected into a tapered amplifier (TA). The output of the TA, after an isolator, is coupled into a single mode polarization maintaining fiber (SMPMF). The output coupler of the SMPMF is chosen to have a small focal length aspheric lens to have a small diameter Gaussian beam out. This is passed through another 80 MHz AOM, A3 (Isomet). The zeroth order is coupled to another SMPMF which carries the light to the experiment table. This AOM is used to control the intensity of the cooling laser. When the AOM is switched on with maximum RF power, most of the laser power is shifted to the first order. The remaining power in the zeroth order also fails to couple to the SMPMF as the spatial mode profile is not Gaussian anymore and propagation through SMPMF extinguishes it. This gives very high fidelity switching of the cooling laser beam. The RF power to the AOM can be varied to achieve a analog modulation of the cooling laser power.

3.7.2 Repumper laser

The repumper laser for the MOT is a Toptica DL100 laser system. It is locked to the $5S_{1/2}\ (F = 2) \leftrightarrow 5P_{3/2}\ (F' = 3)$ atomic transition during the operation of the experiment. The detail of the optical arrangement is given in Fig.3.12(b). The beam out of the laser is first passed through an APP and isolator and then divided into two parts. One part is double passed through a 200 MHz AOM, A5(AA optics: MT200-A0.5-800) and coupled to a SMPMF which carries the laser to the experiment table. The AOM A5 is used to completely extinguish or modulate the intensity of the laser beam delivered to the experiment. The MOT can survive even with very low repumper laser intensity (few tens of micro-watt is enough). Hence this double pass arrangement is required to completely cut off the laser beam. The other part of the laser is double passed through a similar 200 MHz AOM, A4 (AA optics: MT200-A0.5-800) to ensure the same frequency shift as the part going to the experiment. The frequency is monitored in a SAS setup. The laser can be locked on the above mentioned atomic transition based on the signal from PD3 using a PID-PDH combination.

3.7.3 Cavity laser

The cavity laser is a homebuilt ECDL with a Thorlabs:DL7140 laser diode in it. The laser is tuned to scan across the $^{85}Rb5S_{1/2}\ (F = 3) \leftrightarrow 5P_{3/2}$ atomic transition. The optical arrange is very similar to that of the repumper laser, as can be seen in Fig.3.13(a). After APP and isolator, the beam is divided in two parts. Both the parts are frequency shifted by same amount (2×200 MHz) by double passing through similar AOMs A6 and A7 (AA optics: MT200-A0.5-800). One part of the frequency shifted laser is monitored in a SAS and the signal from PD4 can be used to lock the laser on desired atomic transition. The other frequency shifted part is passed through an isolator and then coupled to a SMPMF which carries the laser to the experiment table. The isolator is required to prevent optical feedback from the cavity. This AOM A7 is used to control the cavity laser intensity. Between the AOM set up and the SMPMF, another SAS set

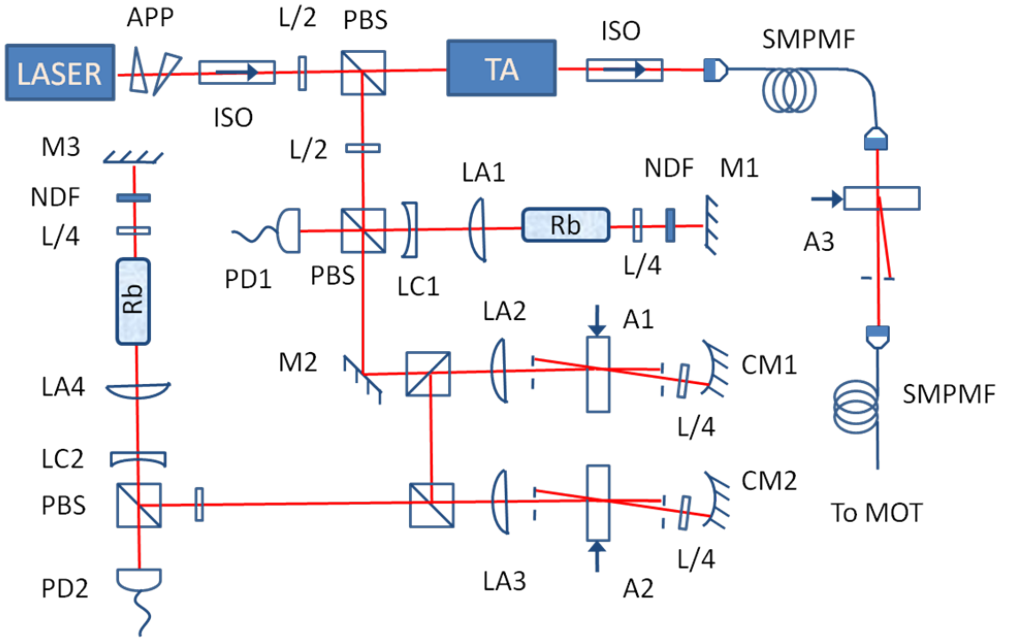

(a) Cooling laser setup

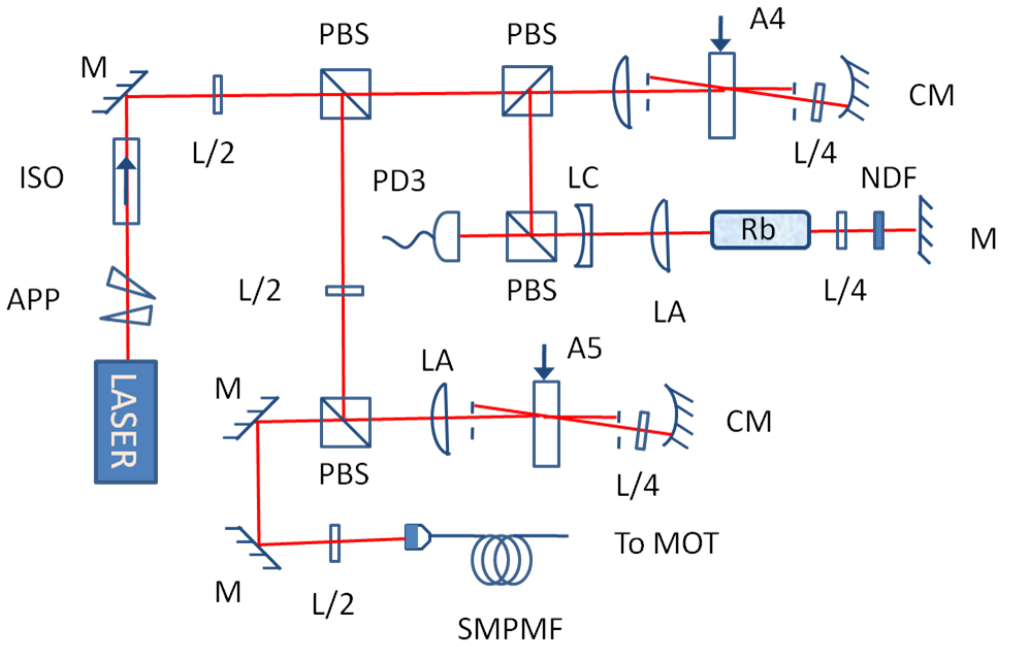

(b) Repumper laser setup

Figure 3.12: The laser setup: Schematic of the optical setup for the cooling (a) and the repumper (b) laser is shown. The abbreviations are explained. APP: Anamorphoic prism pair, ISO: Optical isolator, PBS: Polarizing beam splitter, NPBS: Non Polarizing beam splitter, TA: Tapered Amplifier, M: Plane mirror, CM: Concave mirror, LC: Plano-concave lens, LA: Plano-convex lens, L/2: Half wave plate, L/4: Quarter wave plate, NDF: Neutral density filter, A: Accousto optic modulator, SMPMF: Single mode polarization maintaining fiber, Rb: Rubidium reference cell, PD: Photo diode.

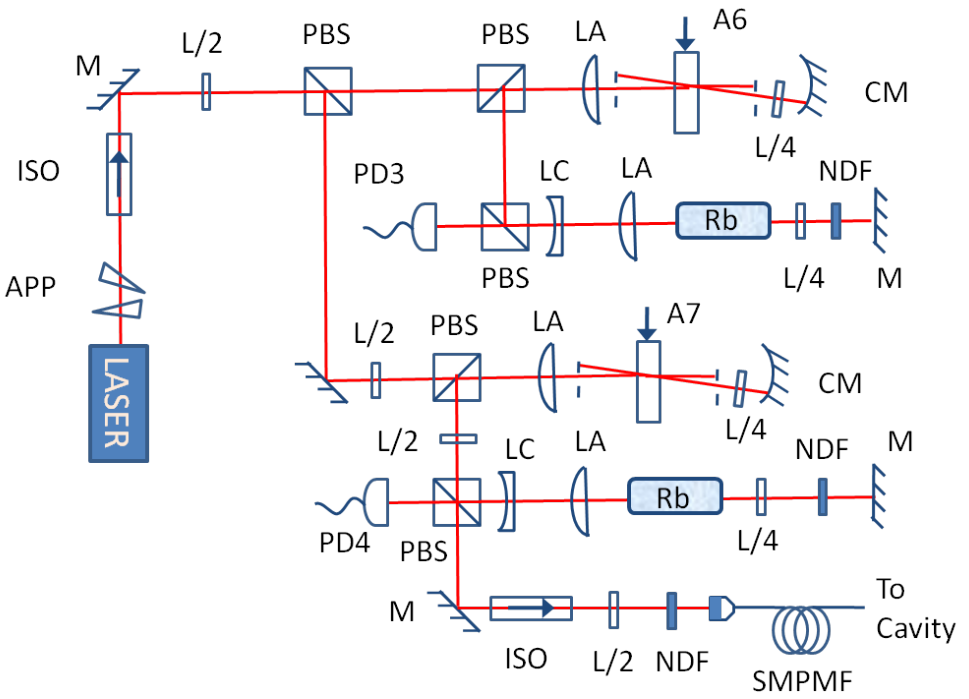

(a) Cavity laser setup

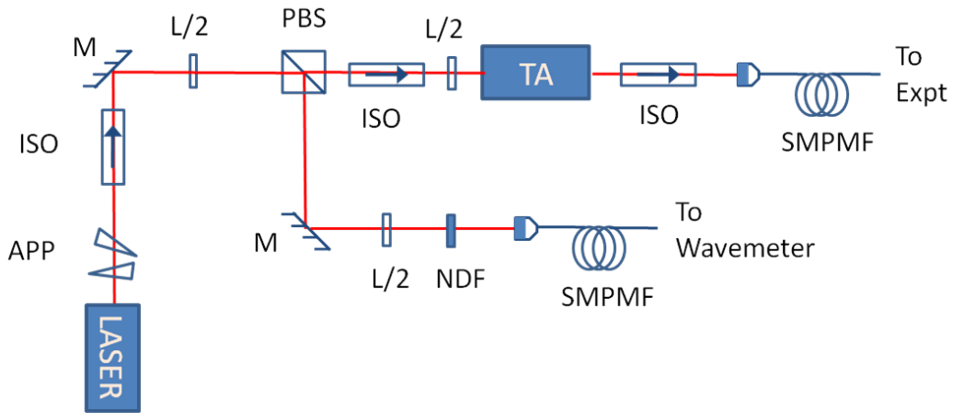

(b) PA laser setup

Figure 3.13: The laser setup: Schematic of the optical setup for the cavity (a) and the Photoassociating (b) laser is shown. The abbreviations are explained. APP: Anamorphic prism pair, ISO: Optical isolator, PBS: Polarizing beam splitter, NPBS: Non Polarizing beam splitter, TA: Tapered Amplifier, M: Plane mirror, CM: Concave mirror, LC: Plano-concave lens, LA: Plano-convex lens, L/2: Half wave plate, L/4: Quarter wave plate, NDF: Neutral density filter, A: Accousto optic modulator, SMPMF: Single mode polarization maintaining fiber, Rb: Rubidium reference cell, PD: Photo diode.

up is installed to actively monitor the frequency of the laser going to the experiment table.

3.7.4 Photoassociation laser

The Photoassociation (PA) laser is also a homebuilt ECDL with a Thorlabs:DL7140 laser diode in it. The laser is tuned to $\sim 60GHz$ red detuned from the $^{85}Rb5S_{1/2}\ (F = 3) \leftrightarrow 5P_{3/2}$ transition. The laser has a very wide mode hop free scanning range of $\sim 10GHz$. The optical arrangement is shown in Fig.3.13(b). The output of the laser is passed through APP and isolator and then divided into two parts. One part is coupled to a SMPMF which is connected to a wavelength meter (High Finesse: WS6) to monitor the wavelength of the scanning laser. Other part is injected into a tapered laser amplifier (Toptica BoosTA) which provides 1W output power. The BoosTA is accompanied by two optical isolators, at input and output end, to avoid feedback. A part of the output from the BoosTA is coupled to a SMPMF which transports the laser light to the experiment table.

3.8 Discussion

In this chapter we have discussed in detail the design and construction of the hybrid apparatus. With the requirements of the apparatus in mind and the constraints arising from combining the traps and the cavity, we have established the platform in which the interaction of multiple species can be studied. We have also discussed about the lasers and the optical arrangements that have been used for the experiments described in this thesis. The experiments performed in the hybrid apparatus to establish its credibility will be discussed in the following chapters of the thesis.

CHAPTER 4

Strong coupling of cold atoms to cavity

4.1 Overview

We now turn our focus to the coupling of atoms to the Fabry-Perot cavity and therefore accessing the QED regime of atom-photon interactions. We will characterize the Fabry-Perot cavity, the MOT of ^{85}Rb atoms formed within the cavity and study the coupling of the laser cooled atoms with the TEM_{00} mode of the cavity. The finesse of the cavity is insufficient to couple individual atoms strongly to the cavity mode. However, a fraction of the atoms in the MOT can couple collectively to the cavity to achieve strong coupling. Vacuum Rabi splitting is demonstrated as an experimental manifestation of atom-cavity strong coupling, and its variation with an effective number of atoms (N_C) coupled to the cavity mode is shown. The system is studied for a closed two-level case as well as with open three-level atomic systems. In both cases the results agree well with the Tavis-Cummings model. This allows one to reliably determine number of atoms effectively coupled to the cavity from experimentally measured VRS. We use this to determine the temperature of the MOT. The significance of such a measurement and its utility as a general technique for the study of interactions in multispecies experiments will be discussed.

4.2 Magneto optical trap of ^{85}Rb atoms.

4.2.1 Rubidium energy level

In the second chapter of this thesis we have discussed the principle of a MOT for a simple two level atom with ground state $F = 0$ and excited state $F' = 1$. Rubidium is a group 1 element with atomic number 37. ^{85}Rb has a nuclear spin of $\frac{5}{2}$. The energy

level diagram for the relevant (to the expt) ^{85}Rb $5S_{1/2} \leftrightarrow 5P_{3/2}$ D2 atomic transition is shown in Fig.4.1. $5S_{1/2}(F = 3) \leftrightarrow 5P_{3/2}(F' = 4)$ is a closed (within dipole approx-

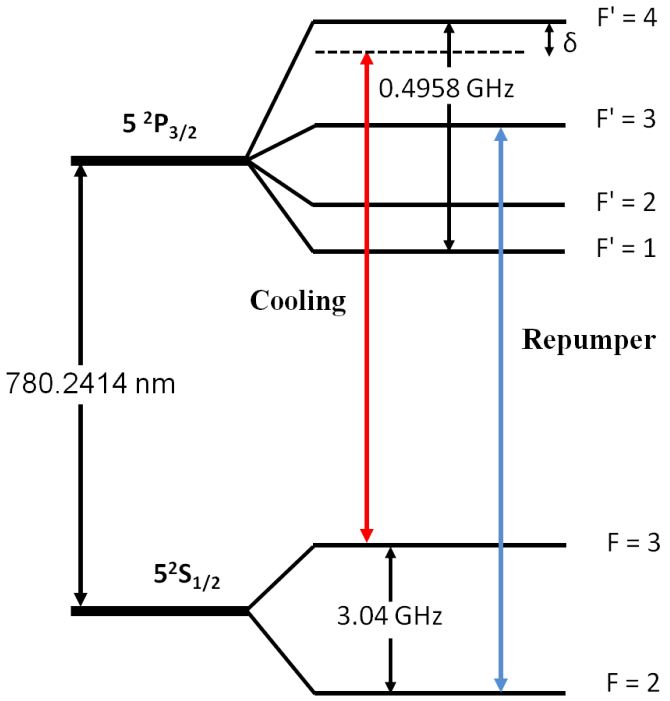

Figure 4.1: Energy level diagram relevant to ^{85}Rb D2 transition

imation) and strong transition, so is chosen for the cooling cycle. Our cooling laser is locked $\sim$ 12MHz (2Γ) red detuned from the atomic resonance. Due to off-resonant pumping from the tail of the Lorenzian frequency distribution of the cooling laser light and quadrupole allowed decay transition from the $F = 4$ excited state, a very weak transition to the $F = 2$ ground hyperfine state is active. The result of this atom accumulation in the $F = 2$ ground state is that within a short time interval the entire population transfers to the $F = 2$ ground and the cooling stops. To operate the MOT in steady state, a mechanism to transfer the atoms to the F = 3 ground state is required. This is achieved with the help of another laser, namely the repumper laser. This laser is locked on the $5S_{1/2}(F = 2) \leftrightarrow 5P_{3/2}(F' = 3)$ transition. So the atoms are repumped back by dipole allowed decay from the $5P_{3/2}(F' = 3)$ to $5S_{1/2}(F' = 3)$ ground state and reenters the cooling cycle. Switching off the cooling or the repumper for a short duration, that is for which the atoms hardly moves but the internal state populations

completely modify due to the transitions, allows us to transfer the entire population in one of the ground states.

Reduction to a two level system

The inhomogeneous magnetic field applied causes Zeeman splitting of both ground and excited hyperfine levels (denoted by quantum number F). The ground $F = 3$ state splits into 7 Zeeman sublevels, denoted by quantum number m_F, ranging from $m_F = -3$ to $m_F = +3$ while the $F' = 4$ excited state splits into 9 $m_{F'}$ states ranging from $m_{F'} = -4$ to $m_{F'} = +4$. Dipole transition between different m_F levels are allowed if $\Delta m_F = 0, +1, -1$ which can be accessed by $\pi, \sigma+, \sigma-$ polarized light respectively when the angular momentum conservation is satisfied. Clearly, for a MOT, under the influence of $\sigma+$ and, $\sigma-$ light, all the atoms will eventually be transferred to the extreme m_F states and will cycle in the $m_F = -3 \leftrightarrow m_{F'} = -4$ or $m_F = +3 \leftrightarrow m_{F'} = +4$ states. So the whole system reduces to an equivalent two level atomic system which can be modeled easily so that the effective position dependent scattering force on ^{85}Rb atom as given in eq.(2.17).

4.2.2 Formation and loading of the MOT

The ^{85}Rb MOT is formed using three mutually orthogonal pairs of counter propagating laser beams intersecting at the geometrical center of the vacuum chamber. The wires of the ion trap is wound in a manner that the center is free from any shadow. Also the thin wires do not create any significant diffraction pattern at the trapping region. Each of the laser beams is $\sim$ 8 mm in diameter and 2Γ detuned from the $5S_{1/2}(F = 3) \leftrightarrow 5P_{3/2}(F' = 4)$ transition, where Γ is the natural linewidth of the transition. The repumping light is on resonance with the $5S_{1/2}(F = 2) \leftrightarrow 5P_{3/2}(F' = 3)$ transition and co-propagating with the cooling laser beams. The cooling and the repumper lights are derived from two different lasers and mixed using a beam splitter. Both the lasers are frequency referenced by saturation absorption spectroscopy (SAS) and can be actively stabilized to a desired frequency by means of PID feedback to

the ECDL cavity. The smoothed SAS signal is shown in Fig.4.2. Both the lasers goes through AOM before being transferred to the experiment table (see section 3.7 for detail). The driving RF power to the AOMs can be used to control the intensity of the lasers at the experiment. A complete ON(OFF) of the RF power of the AOM in the cooling (repumper) path leads to complete switch OFF (ON) on the experiment table.

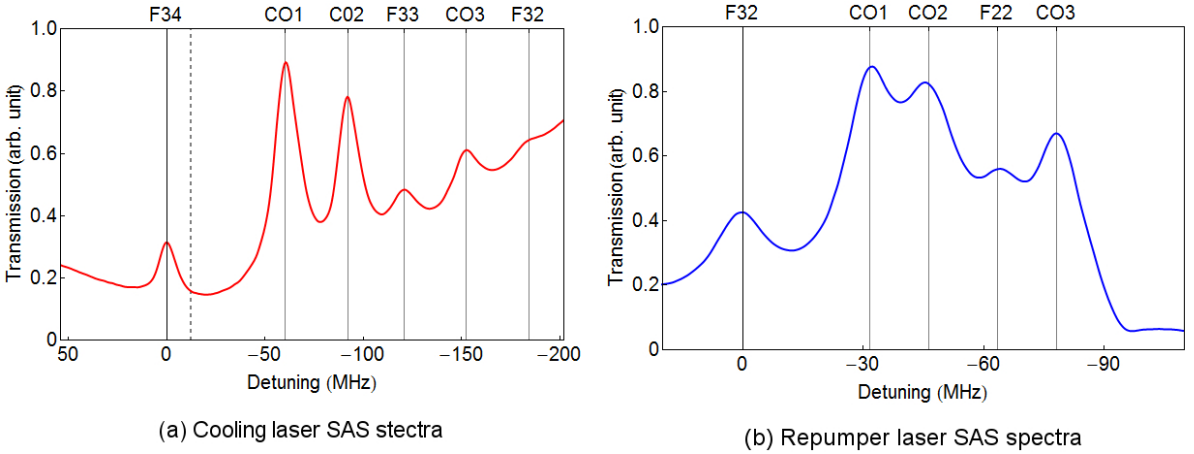

Figure 4.2: Saturation absorption spectroscopy of the cooling (a) and the repumper (b) laser. The dipole allowed hyperfine transitions and the crossovers are marked with solid line. F_{ij} represents the $F = i \leftrightarrow F' = j$ hyperfine transition. The dotted line shows the position where the cooling laser is locked.

The magnetic field gradient is produced using a pair of coils in anti-Helmholtz configuration. Detail of the coils are provided in chapter 3. We use 5 Amps of current through the coils to obtain a 22 G/cm of magnetic field gradient at the center of chamber. This relatively high gradient magnetic field helps to create a compact but dense MOT which is helpful to couple a larger fraction of the atomic ensemble to the cavity mode.

The atoms are derived from a Rubidium getter source (SAES:Rb /NF / 4.8 / 17FT10+10). When a few Amps of current is passed through it, the getter heats and emits hot atomic vapor. The rate of emission depends on the current which is not linear. However at any set value of getter current, the rate emission of atoms is very stable and reproducible. The capture velocity for ^{85}Rb atoms in our MOT configuration is 30 m/s.

So only a very small fraction of the atoms emitted by the source are captured in the MOT. The rest, in an equilibrium between the emission and pumping out rate, forms the background vapor. Collision between the MOT atoms and the relatively high energy background vapor leads to loss of atoms from the MOT. An equilibrium between the loading rate and the loss rate of atoms determines the total number of atoms in the MOT. The dynamics of the loading process can be written as [53]

$$\begin{aligned} N_{MOT}(t) &= N_0\left(1-e^{-\gamma_{ml}t}\right) \\ &= \frac{L}{\gamma_{ml}}\left(1-e^{-\gamma_{ml}t}\right) \end{aligned} \tag{4.1}$$

where $N_0 = \frac{L}{\gamma_{ml}}$ is the steady state atom number in the MOT. L is the loading rate of the atoms in the MOT and γ_{ml} is the loss rate of atoms from the MOT. Fig.4.3 shows a typical loading of the MOT. A fit of the presented data with eq.(4.1) yields MOT loading rate $L = 3.31 \times 10^5$ atoms/s and collisional loss rate $\gamma_{ml} = 0.254/s$ corresponding to a steady state atom number in the MOT, $N_0 = 1.3 \times 10^6$. In our experiment, we vary the total number of atoms in the MOT by changing the current through the dispenser which changes the MOT loading rate too.

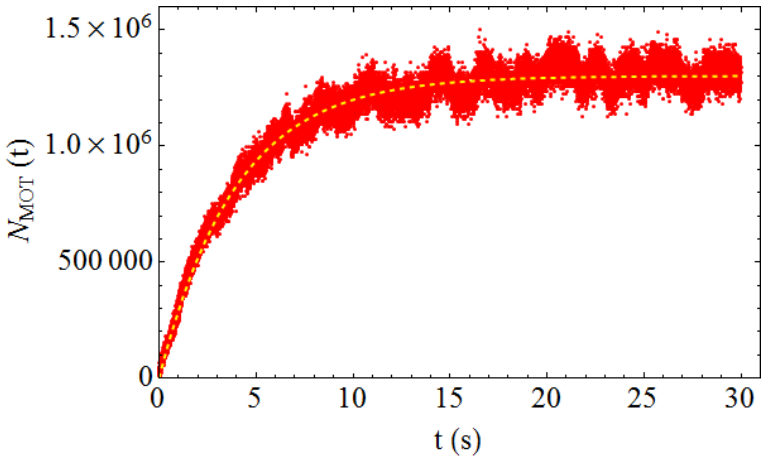

Figure 4.3: Typical MOT loading: The red dots shows the experimental data. The dashed line is a fit with eq.4.1 yielding MOT loading rate $L = 3.31 \times 10^5$ atoms/s and collisional loss rate $\gamma_{ml} = 0.254/s$ corresponding to a steady state atom number in the MOT, $N_0 = 1.3 \times 10^6$.

4.2.3 Imaging and atom number detection

The atoms participating in the cooling cycle scatters photons at a rate given by eq.(2.11) in all 4π steradian. The photons, scattered in a given solid angle, are collected to image the MOT as well as determine the number of atoms in the MOT. In addition to the atomic fluorescence, the thin Tungsten wires of the ion trap also scatters some light which creates a very noisy background for measurement. To eliminate this problem, we spatially filter the fluorescence of the MOT using a 2f-2f lens combination. A schematic of the set up is shown in Fig.4.4.

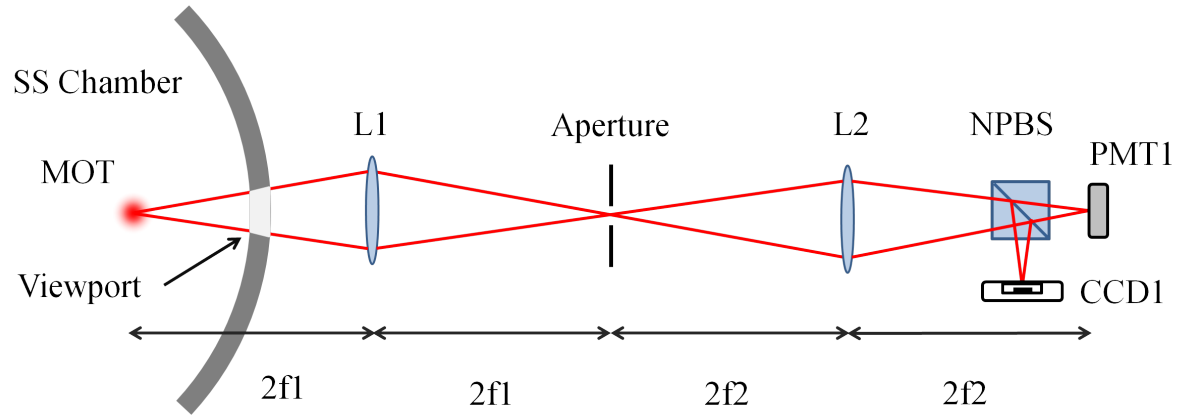

Figure 4.4: Schematic of the MOT detection scheme: The fluorescence is collected and spatially filtered to eliminate background scattered light. The light is then divided into two parts using non polarizing beam splitter (NPBS). One part goes to a photomultiplier tube (PMT) for total atom number detection. Other part images the MOT onto a CCD camera to obtain the spatial profile of the MOT.

The viewport of the chamber defines the solid angle of the light collection. The spatially filtered light is then divided by a non-polarizing beam splitter. One component is incident onto a CCD camera (Thorlabs: DCU224M), imaging the MOT. The other component is incident onto a calibrated PMT (Hamamatsu Photonics:R636-10) which returns a current value proportional to the incident light intensity. The photon flux, scattered by the atoms in the MOT, is measured by the PMT. The small current signal is then amplified by 10^5 times using a calibrated preamplifier (Hamamatsu Photonics: C7319) and then terminated onto an oscilloscope to obtain a voltage proportional to the

number of atoms in the MOT. Given the atom-photon scattering rate for the intensity and detuning of the cooling laser, the total number of atoms in the MOT is determined. Calibrated band pass filters (Thorlabs: FL780-10) are installed in front of both PMT and CCD camera in order to eliminate all the off-resonant light.

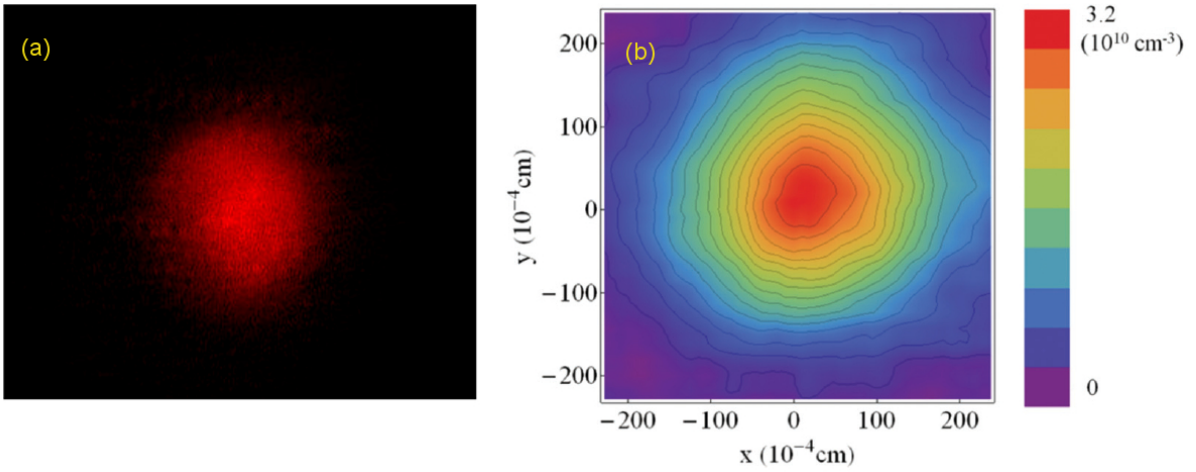

Figure 4.5: Typical MOT profile: (a) False colored unsaturated image of a typical MOT. (b) The MOT density profile. The Gaussian FWHM is 235μm and peak number density is 3.2 $\times$ $10^{10}/cm^3$

The camera images the MOT and provide information about the projection of the spacial profile of the MOT in a plane perpendicular to the imaging axis. The spatial profile, along with the total number of atoms captured in the MOT provides the density profile of the MOT. We assume a symmetric 3D Gaussian MOT which is accurate to a certain extent in our experiment. Fig.4.5 show a typical MOT and the density distribution. A symmetric Gaussian fit on the spatial profile obtains the full width at half maximum (FWHM) of 235 μm. Normalized Gaussian distribution with the fitted FWHM, multiplied by the total number of atoms captured in the MOT gives the number density distribution $\rho_A(x, y, z)$ of the MOT.

4.3 The Fabry-Perot cavity

The Fabry-Perot cavity consists of two mirrors with radius of curvature R = 50mm. The mirrors are mounted (See chapter 3 for detail) symmetrically on both side of the MOT at a separation of $\sim$ 45 mm. A DC voltage can be applied to a ring pzt attached to one of the mirrors to fine tune the length of the cavity. The axis of the cavity passes through the center of the trapping region. The measured reflectivity r_m of each mirror is $r_m = 0.9997$ at $\lambda = 780nm$. Detail characterization of the cavity is given below.

4.3.1 Cavity characterization setup

To characterize the cavity, a probe laser beam scanning in frequency, is coupled into the cavity by means of two beam steering mirrors. The setup is shown in Fig.4.6. The beam is coming out of a SMPMF in order to clean up the spatial mode and have a pure TEM_{00} mode at the input of the cavity. A half wave plate and polarizing beam splitter (PBS) combination at the input provides control over the intensity of the input light as well as ensures pure linear polarization. Output of the cavity is divided in two parts using a NPBS. One part fall on a CCD camera to monitor the mode built within the cavity. The other part fall on a photodiode which monitors the intensity of the light coupled out of the cavity.

4.3.2 Coupling the probe laser to the cavity

The initial alignment for coupling is done by monitoring the light reflected back from the cavity. The ray reflected from the plane surface of the input mirror should track back the original ray and the diverging ray reflected from the convex (w.r.t the input beam) surface of the mirror should also be coaxial. This can be achieved by a beam walk using mirrors M1 and M2. At this stage, some mode should be visible at the CCD camera while the probe laser is scanning. The coupling is further optimized in an iterative process by monitoring the higher order modes at the CCD camera. Using one mirror the brightness of the mode is increased while using the other mirror the sym-

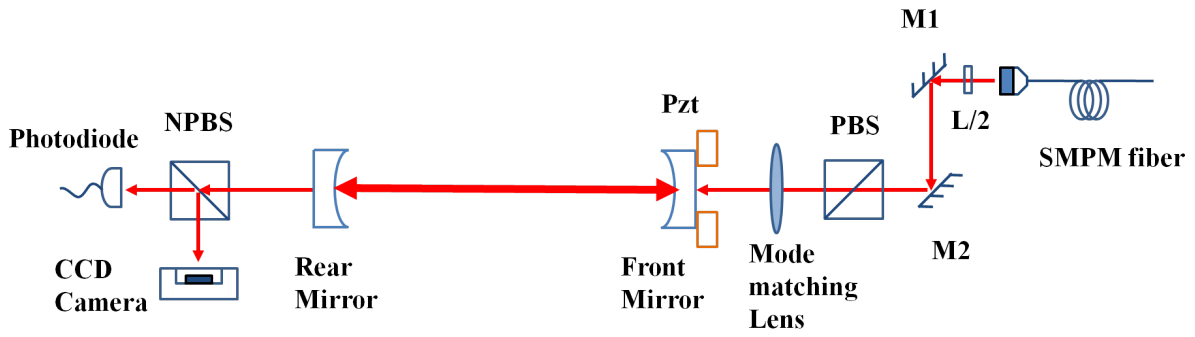

Figure 4.6: Set up for cavity characterization: The TEM_{00} beam coming out of the SMPMF is coupled into the cavity using a pair of beam steering mirrors (M1 and M2) and a mode matching lens. A half wave plate and PBS combination controls the input light intensity. Light coupled out of the cavity is divided into two parts. The intensity is measured in a photodiode while the mode profile is monitored on a CCD camera.

metry of the mode is restored. After a few iterations one can obtain a bright symmetric mode. At last the mode matching lens is placed on the path of the input beam just before the cavity to ensure maximal light coupling to the desired TEM_{00} mode. We use a 100 mm focal length achromatic doublet mounted on a 3D translation stage for this purpose. The lens is positioned $\sim$ 100mm from the center of the cavity. The x-y position of the lens is again adjusted by looking at the symmetry of the mode.

4.3.3 Cavity linewidth and finesse

A typical spectrum of the cavity while the probe laser is scanning in frequency is shown in Fig.4.7(a). The probe laser is frequency referenced by means of a SAS of Rubidium. The separation between two TEM_{00} modes is measured to be 3.3 GHz. The linewidth of the cavity, is measured by creating 20 MHz sidebands on the laser light coupled into the cavity and detected in transmission as the cavity length is scanned (Fig.4.7(b)). A series of these measurements permits the determination of the cavity linewidth at this frequency as $1.4 \pm (0.2)$ MHz, which corresponds to the finesse of $\approx$ 2350 as per eq.(2.45). The measured reflectivity of the mirrors are $\approx$ 0.9997 which corresponds to an ideal finesse of $\approx$ 10500. The reduction in the measured value of finesse of our

cavity can be attributed to the additional loss channels of the photons from the cavity by scattering and absorption at the two mirrors and the fact that the laser used has a linewidth of ~ 1 MHz. It must be noted that generation of side bands actually increases the FWHM slightly. So what we measure is actually the lower bound of the finesse.

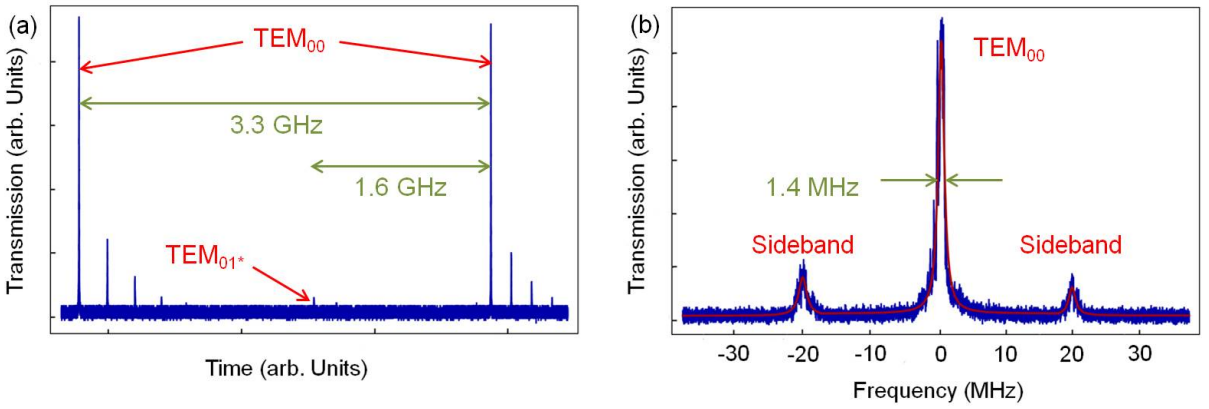

Figure 4.7: Cavity transmission: (a) A full FSR scan is shown. After mode matching, the dominant peaks are TEM_{00}. The next higher order transverse peak TEM_{01^*} is also shown. Other higher order transverse modes appears due to aberration effect lifting the degeneracy of the folded transverse modes. (b) 20 MHz sideband generated around the TEM_{00} peak. The position of the sidebands are used as a frequency reference to measure the FWHM of the peak.

4.3.4 Cavity waist and mode volume

In order to determine the mode volume V_{CM} and the waist w_0, one needs to accurately measure the length d of the cavity. The frequency spacing between a specific TEM_{mn} and the next higher order transverse mode is given by

$$\Delta\nu_{tr} = \nu_{m,n} - \nu_{m,n+1} = \frac{c}{2\pi d}\cos^{-1}\left(1 - \frac{d}{R}\right), \tag{4.2}$$

where $c/2d$, the free spectral range (FSR) of the cavity is the frequency spacing between two adjacent TEM_{00} modes. The exact length of the cavity is obtained by measuring $\Delta\nu_{tr}$ using the sideband technique, giving the precise value of $d = 45.7$ mm. The waist of the TEM_{00} mode at the center is $w_0 = 78\mu$m.

4.4 Atom Cavity Interactions

When the cavity is loaded with near resonant atoms, the emission properties of the atoms and the cavity gets modified in presence of each other [8, 29]. Two regimes of interest are (a) weak coupling and (b) strong coupling between the cavity and the atoms. These regimes are categorized using three independent parameters, the free space atomic spontaneous emission decay rate γ, the photon decay rate from the empty cavity κ, and the single atom cavity coupling g_0. In the weak coupling regime, when $\gamma > g_0 > \kappa$, the spontaneous emission rate of the atom into the cavity mode can be enhanced or inhibited depending on the system parameters. For a single atom, the strong coupling regime is achieved when $g_0 > (\gamma, \kappa)$ [39]. Here the atom cavity coupling lifts the degeneracy in the atom photon dressed state manifold. This lifting of degeneracy is detected, by measuring the near atomic resonance transmission profile, of the atom cavity coupled system. A split in the transmission profile of $2g_0$ is observed and identified as the vacuum Rabi split (VRS) [43,54,55]. When N_C atoms collectively couple to a single mode of the cavity, the coupling strength is enhanced by a factor of $\sqrt{N_C}$ and the new eigenstates are separated by the effective coupling strength $2g_0\sqrt{N_C}$ [44,56,57]. In our experiment, the finesse of the cavity is not sufficient for achieving a single atom -cavity strong coupling. However a fraction of the atoms can collectively couple to the cavity mode to achieve strong coupling. Vacuum Rabi splitting is demonstrated as an experimental manifestation of atom-cavity strong coupling.

4.4.1 Experimental setup

A schematic of the experimental setup is shown in Fig.4.8. The probe laser scanning in frequency, comes out of a SMPMF and is coupled into the cavity by means of two beam steering mirrors M1 and M2. A PBS along with a $\lambda/2$ wave plate is used to control the intensity of the probe laser as well to ensure a linear polarization. A neutral density filter (NDF) is used to further reduce the light intensity. A mode matching lens L3 is placed 100 mm from the cavity center to match the spot size and radius of curvature of

the input beam to that of the TEM_{00} mode of the cavity to ensure maximum coupling of light to the TEM_{00} mode. A $\lambda/4$ wave plate, with its axis oriented at $\pm 45^{\circ}$ w.r.t to the polarization of the input beam, can be placed just before the mode matching lens to create circularly polarized light. The output light is divided into two parts. One part goes to a calibrated PMT (PMT2) to measure the intensity of the output beam. The other part is imaged onto a CCD camera to monitor the mode developed within the cavity. The fluorescence from the MOT is collected using lens L1 and is spatially filtered as shown in Fig.4.4 for atom number detection as well as monitor the spatial profile.

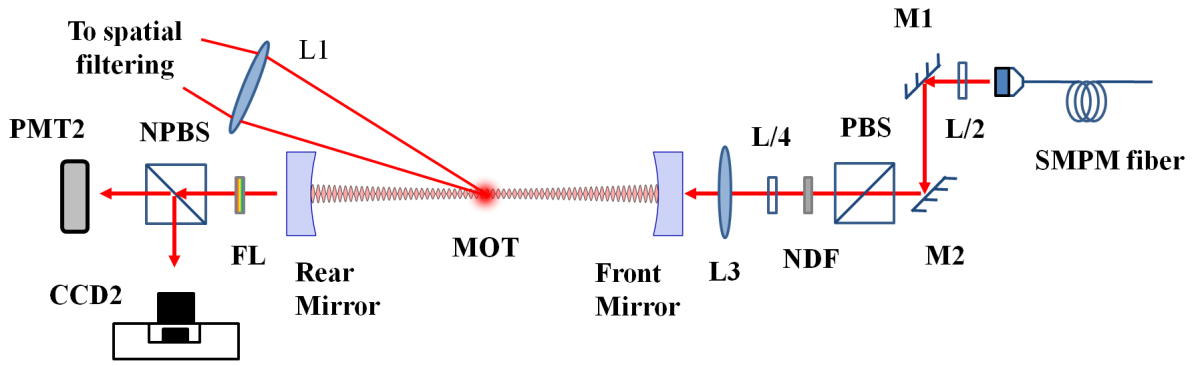

Figure 4.8: The experimental setup: The MOT is formed at the center of the cavity. The probe light is coupled into the cavity using a pair of beam steering mirrors (M1, M2) and a mode matching lens (L3). Intensity of the input probe light is controlled using a NDF and a combination of half wave plate (L/2) and PBS. A quarter wave plate (L/4) controls the polarization of the input beam. The transmitted probe light from the cavity is divided and detected by PMT2 and CCD2. Fluorescence light from the MOT atoms is collected on lens L1, spatially filtered (as shown in Fig.4.4), and detected by the PMT1-CCD1 setup. Narrow band optical filter (FL) is installed in the path in order to eliminate light of unwanted wavelength.

4.4.2 Alignment of MOT to the cavity

Alignment of the MOT center with the cavity axis is very crucial for this experiment. By design, the cavity axis is supposed to pass through the center of the MOT. The po-

sition of the MOT can be changed by adjusting the anti-Helmholtz coil pair. With basic alignment, a fraction of the MOT fluorescence is coupled out of the cavity. The spatial structure of the modes is monitored on CCD2. Fine alignment is achieved iteratively, by maintaining radial symmetry of the higher order modes coupled out of the cavity as well as the symmetric Gaussian spatial profile of the MOT (imaged on CCD1). Fig.4.9 shows the MOT fluorescence coupled out of the cavity at different modes when a good alignment is achieved.

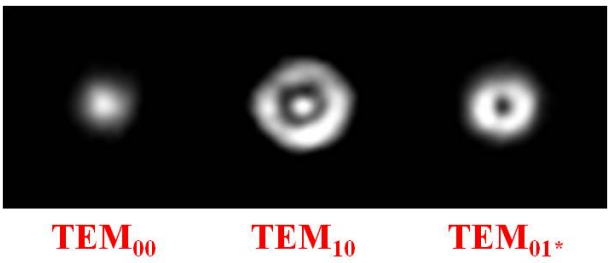

Figure 4.9: The MOT fluorescence is coupled to the cavity if the resonance condition is satisfied. When the MOT is well aligned w.r.t the cavity axis, radially symmetric modes (fundamental and higher orders) can be observed on CCD2 as the cavity length is scanned. The images shows few such modes imaged on CCD2.

It must be noted that the MOT density FWHM is much larger than the cavity waist. Also the radius of curvature of the spherical wave front of the fluorescence do not match exactly to that of the mirror at the reflecting surface. As a result, the spectral degeneracy between several higher order transverse modes are broken. So if we scan the cavity length while the MOT is fully loaded, a number of higher order transverse modes apart from the TEM_{00} mode also gets excited and the spectra is quite dense. Also with every peak in the cavity transmission, one observes a dip in the free space MOT fluorescence collected by PMT2. This is due to enhanced spontaneous emission of the atoms into the cavity mode by suppression of the free space emission rate. This effect can be used to develop a cavity mediated frequency sensitive detection technique for trapped molecules.

4.4.3 Experimental procedure

Below we describe the experimental procedure to measure the VRS across all the dipole allowed D2 atomic transitions (ω_{at}) from the $F = 3$ ground state. The relevant energy level diagram is shown in Fig.4.10. The MOT is first loaded to number saturation. The cavity length is tuned so that it is resonant with one of the atomic transition frequency $\omega_{34,33,32}$ corresponding to $5S_{1/2} - 5P_{3/2}$, $F = 3 \leftrightarrow F' = 4, 3, 2$ (shorthand notation: $3 - 4', 3', 2'$) transitions shown in Fig.4.10(a). The atoms are then optically pumped by sequentially switching off the cooling and repumping lasers to create a non-fluorescing atomic population in the $5S_{1/2}$ $(F = 3)$ atomic state. At first the cooling laser is switched off, preparing the atoms in $F = 3$ state. The repumper laser pumps the small fraction of atoms in the $F = 2$ state back to $F = 3$ state and then switched off after 100 μs. After another 100 μs, the weak probe laser is turned on and scanned across the relevant ω_{at} within next 1ms. The experimental sequence is shown in Fig.4.10(b). The transmitted light from the cavity is detected as illustrated in Fig.4.8. The transmitted spectra shows a double peak structure around the atomic resonance (as shown in inset of Fig.4.10(b)) when strong coupling is achieved. It is important to note that the $3 - 4'$ is a closed cycle transition but the $3 - 3'$ and $3 - 2'$ are not. When these open transitions are being probed, no VRS is seen, unless the weak repumping light is also kept on to recycle back the atoms to the $5S_{1/2}, F = 3$ ground state.

4.4.4 Conditions for atom-cavity strong coupling

Condition for strong coupling for a single atom to a single mode of a cavity is $g_0 > (\gamma, \kappa)$ [44,55]. The single atom-cavity coupling g_0 is written as [29,54],

$$g_0 = \sqrt{\frac{\mu^2 \omega_{at}}{2\hbar\epsilon_0 V_{CM}}}, \tag{4.3}$$

where, μ is the transition dipole matrix element between the participating states, ω_{at} is 2π times the transition frequency, ϵ_0 is the permittivity of free space, $\hbar$ is the reduced Planck's constant and $V_{CM} \sim \pi w_0^2 d/2$ is the cavity mode volume. In our experiment,

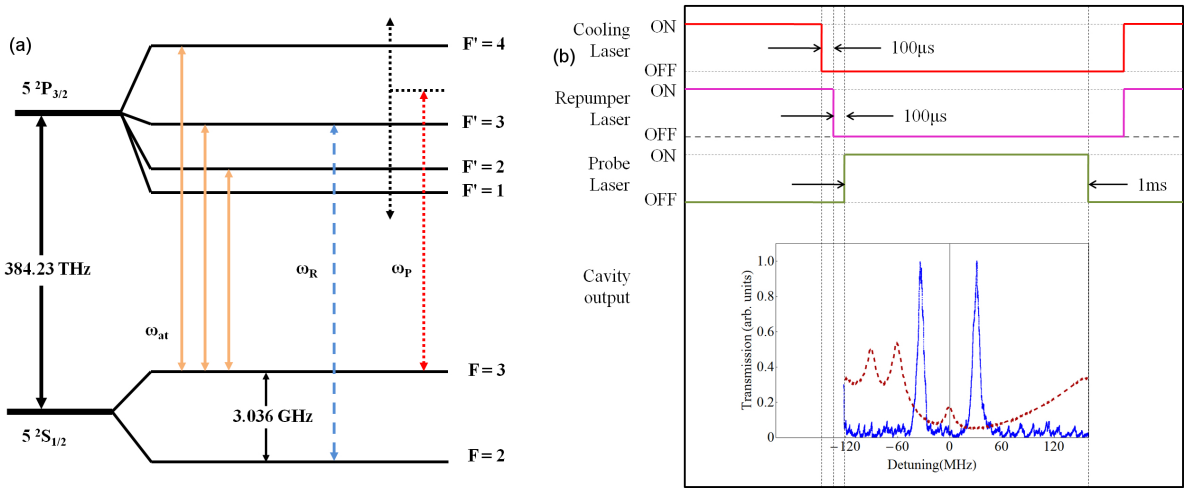

Figure 4.10: (a)The energy level diagram for ^{85}Rb relevant to the present experiment. The solid orange line shows the dipole allowed atomic transitions (ω_{at}) connecting $F = 3$ ground state. VRS is observed against one of these transitions. Cooling laser is $\sim -2\Gamma$ red detuned from (ω_{34}). The dashed blue line represent the repumping laser frequency. The dotted red arrow represent the probe laser scanning across. (b) Timing sequence diagram illustrates the procedure for measurement of the VRS on the $F = 3 \leftrightarrow F' = 4$ transition. The cooling and the repumper lasers are sequentially switched off at 100μs interval to prepare the population in $F = 3$ ground state. A weak probe laser scanning across ω_{34} is then turned on for 1ms. The transmitted spectra shows VRS (inset) during the measurement, the cavity is tuned to ω_{34}. The whole sequence is repeated at 12.5Hz. In the bottom figure, the solid trace shows a typical VRS spectrum while the dashed trace exhibits a part of the Rb saturation absorption spectrum, which serves as a frequency reference.

given the relatively large mode volume required by geometric constraints to accommodate the MOT, the single atom cavity coupling strength is too small to allow strong coupling. However collective strong coupling can easily be achieved by increasing the number of MOT atoms (N_C) coupled with the cavity mode as discussed in chapter 2 of this thesis. In this scenario, the separation between the new eigenstates is given by [44, 56, 57],

$$VRS = 2g_0\sqrt{N_C} \tag{4.4}$$

Depending on the strength of the dipole transition of the two participating states, the minimum number of atoms required to achieve strong coupling changes. In the

present experiment, the MOT gradient magnetic field is on throughout the experiment. In this case the atomic dipoles of the cavity mode atoms will have projections along all three directions depending on their positions. As a result, over the entire atomic ensemble in the cavity mode, the probe light of any given input polarization can be considered to have a nearly isotropic polarization, seen by the atomic dipoles. So we utilize the transition dipole matrix for isotropically polarized light [58], in estimating the theoretical value of g_0, using eq. (4.3). The calculated values for g_0 are 142 kHz, 93 kHz and 50 kHz corresponding to ω_{34}, ω_{33} and ω_{32} respectively. The typical $N_C(\sim 10^4)$ in the present setup is therefore sufficient to achieve a detectable strong coupling VRS, for these transitions.

4.4.5 Experiments and Results

The number of atoms in the MOT is determined by measuring the fluorescence collected on PMT1. The density profile of the MOT is determined by fitting a symmetric Gaussian to the image of the MOT captured by CCD1. The fitted normalized Gaussian distribution with the measured FWMH, multiplied by the total number of atoms captured in the MOT gives the number density distribution $\rho_A(x,y,z)$, of the MOT. The field distribution of the TEM_{00} mode of the cavity is given by [59],

$$\psi(x,y,z) = \frac{w_0}{w(z)}\, exp[-\frac{x^2+y^2}{w^2(z)}]\, sin(kz), \tag{4.5}$$

where, $\hat{z}$ is the cavity axis and $w(z)$ is the width of the cavity mode at a distance z from the cavity center. So the effective number of atoms coupled to the cavity mode is given by

$$N_C = \int_{\tilde{V}} \rho_A(x,y,z)\, \psi^2(x,y,z)\, dxdydz, \tag{4.6}$$

where the integration volume, $\tilde{V} \gg V_{MOT}$ the MOT volume.

The variation of VRS as a function of N_C, when the cavity length is tuned to the atomic resonance (ω_{at}), is measured. In such a measurement only the $3-4'$ transition is closed and therefore is a two level system, whereas the $3-3', 3-2'$ transitions are open, allowing the atom from the excited $3', 2'$ state to decay to the $5S_{1/2}(F=2)$ state, making

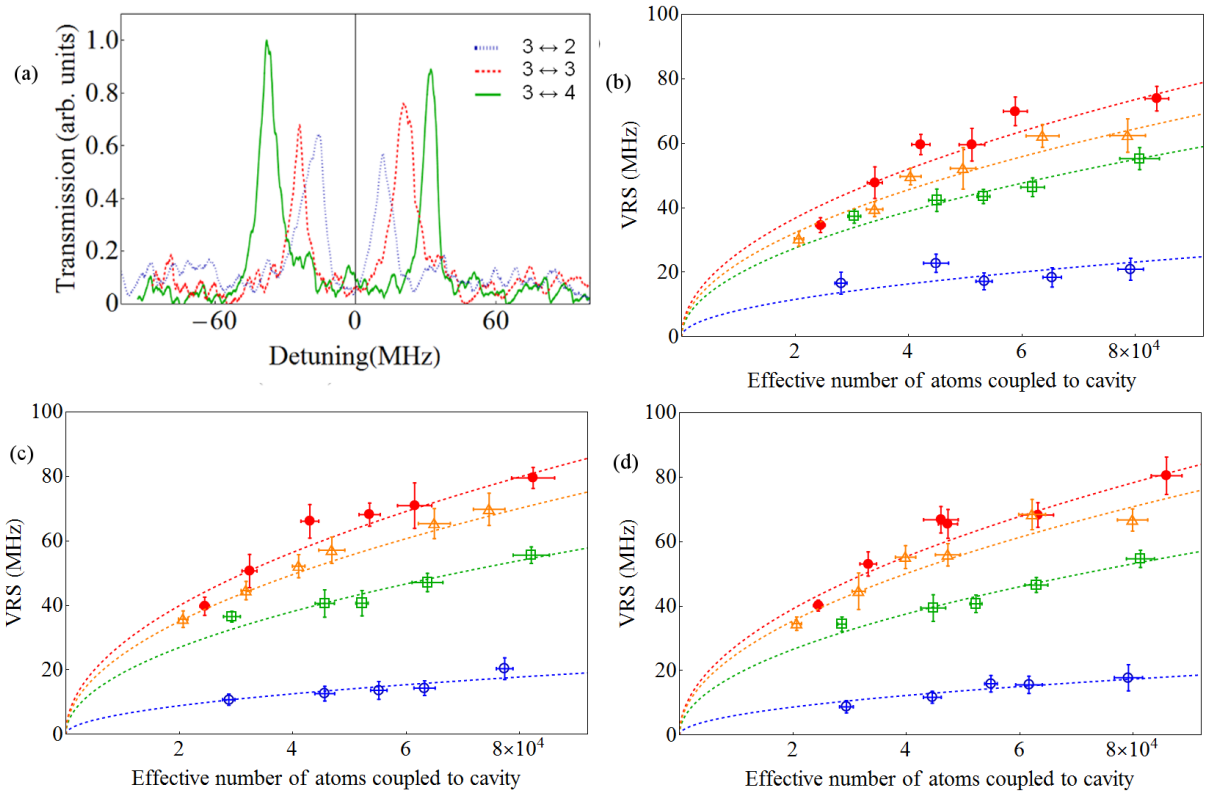

Figure 4.11: (color online) (a) Typical experimentally observed VRS against the $F = 3 \leftrightarrow F' = 4, 3, 2$ atomic transitions. Panels (b), (c) and (d) illustrate VRS as a function of atom number (N_c) in the cavity mode. Red discs, orange triangle, green square and blue circles represent VRS across ω_{34} with repumper on, ω_{34} with repumper off, ω_{33}, and ω_{32} transitions respectively. The error bars are the statistical errors representing one standard deviation. The dashed lines are the fits to each set of data by $2g_0\sqrt{N_C}$, from which the value of g_0 can be determined for each transition. Data for linear polarization (LinP) (b), left circular polarization (LCP) (c), and right circular polarization (RCP) (d), of the probe laser has been shown. Fit value and errors to the fits have been summarized in the Table.4.1.

these effectively three level systems. This then constitutes a loss channel from the excited state, and no VRS is detected in this case, unless this loss channel is plugged by keeping the weak repumping light on. When this is done, VRS can be observed around the $3-3',2'$ transitions also. VRS measurements were made across $3-4'$ transition with repumper on and off to compare the difference. These measurements are illustrated in Fig. 4.11.

To measure the atom cavity coupling, the number of atoms in the cavity mode volume is varied by changing the getter current in a systematic way. The variation in the atom number is measured from the MOT fluorescence. The corresponding change in VRS is shown in Fig. 4.11. Fit of the data by eqn. (4.4) measures the g_0 for each transition. The results are given in Table. 4.1.

Table 4.1: Experimentally measured values of g_0, the atom$-$cavity coupling constant, for the various cases of probe polarization and transitions considered. R and NR in parenthesis represents a measurement with repumping or no repumping respectively. The standard deviation errors to the fits in Fig. 4.11 are shown for each measurement.

At.$-$Cav. Coupling	LinP (kHz)	LCP (kHz)	RCP (kHz)
$g_{0;34}$(NR)	$114 \pm (2.6)$	$124 \pm (2.9)$	$125 \pm (3.3)$
$g_{0;34}$(R)	$130 \pm (3.9)$	$141 \pm (3.2)$	$138 \pm (3.7)$
$g_{0;33}$(R)	$97 \pm (2.1)$	$95 \pm (2.4)$	$94 \pm (1.8)$
$g_{0;32}$(R)	$41 \pm (3.5)$	$31 \pm (1.7)$	$31 \pm (1.3)$

Clearly, when repumping is off, the measured value of $g_{0;34}$ is lower than when the repumping laser is on. This is attributed to a loss of atoms during the experiment, into the $F = 2$ dark state. When the repumping laser is on, the atoms are pumped back into the $F = 3$ ground state, and participate in atom-cavity coupling. For the $g_{0;33}$ and

$g_{0;32}$ measurements, the presence of the repumping light is a must. We also note that the measured values of g_0 are mostly insensitive to the polarization state of the probe light, as seen in Table. 4.1, and discussed earlier. For further measurements using VRS, we use the experimental values of g_0, as these will incorporate any birefringence due to the cold trapped atoms and the cavity mirrors.

4.4.6 Temperature measurement of MOT using VRS

Having determined the experimental atom cavity coupling constants, we now use them to measure the MOT temperature. Since the duration of the measurement is long, the getter source is kept at a low current value, so that there is no build up of ambient vapor pressure during the experiment. This means working with a small MOT and therefore smaller VRS. It also implies that the measurements needs to made across ω_{34}. The experimental sequence remains similar to the one described above, with one exception. The time interval between the switching off of the cooling laser and the probing of the cavity mode atoms, τ is now varied. Once the cooling laser is turned off, the cooling stops and the MOT undergoes ballistic expansion. The repumper laser remains on throughout the experiment. As τ increases, number density of the MOT decreases and hence the number of atoms coupled to the cavity mode falls. The fall of N_C with τ can be probed from the measured VRS at different time intervals using eqn. (4.4). This behavior is illustrated in Fig. 4.12. Under the reasonable assumption that the expanding atom density distribution is Gaussian and symmetric, the σ for the Gaussian density distribution can be found as a function of τ. For the ballistically expanding cold cloud with initial temperature T the rate of expansion is given [60] as,

$$\sigma^2(\tau) = \sigma^2(0) + \frac{k_B T}{m_{Rb}}\tau^2, \tag{4.7}$$

where k_B is the Boltzmann constant and m_{Rb} the mass of the ^{85}Rb atom.

Fig. 4.13 shows experimentally measured $\sigma^2(\tau)$ as a function of τ^2. The linear slope

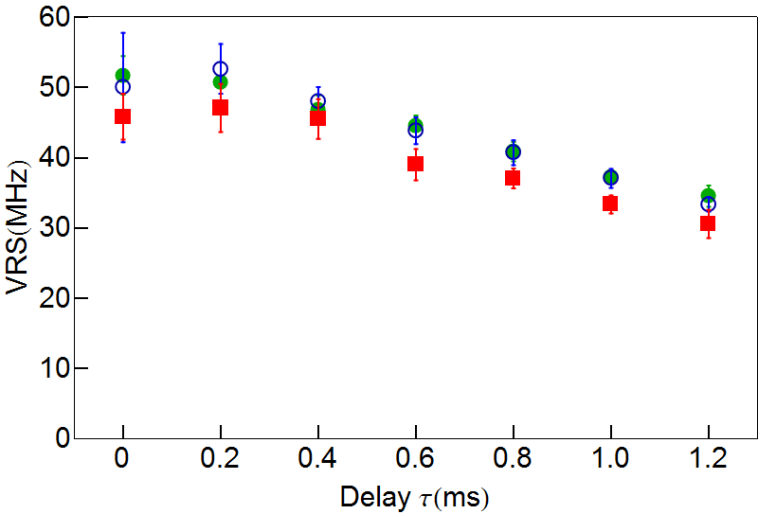

Figure 4.12: (color online) The fall in the VRS as a function of time interval τ. Due to the systematic decrease in the N_C after the cooling laser is cut, the VRS falls with increasing τ. The measurement is done across ω_{34} transition, with repumper on, for a MOT with low atom number. Red square, green disk and blue circles represents data for LinP, LCP and RCP probe laser respectively. The error bars represents the statistical errors in measurement.

on this plot is proportional to the temperature of the MOT (T_{MOT}). We note that the intercept $\sigma^2(0)$ very accurately measures the initial spatial size of the MOT, emphasizing the robustness of the time of flight measurement technique demonstrated here. The experiment was performed across ω_{34} with linearly polarized (LinP), left (LCP) and right (RCP) circularly polarized probe laser, with the repumping light on. The MOT temperatures obtained are given in Table. 4.2, along with the one-sigmas errors to the respective fits. The combined temperature of the MOT obtained from all three polarization states of the probe laser is $T_{MOT} = 107.7 \pm 7.5\ \mu$K [14], which is reasonable for the small MOT in the experiment.

4.4.7 Systematic errors

In addition to the statistical errors that has been stated, two sources of systematic errors in this method for temperature determination are the gradient magnetic field and gravity. It must be noted that the gradient magnetic field has not been turned off during

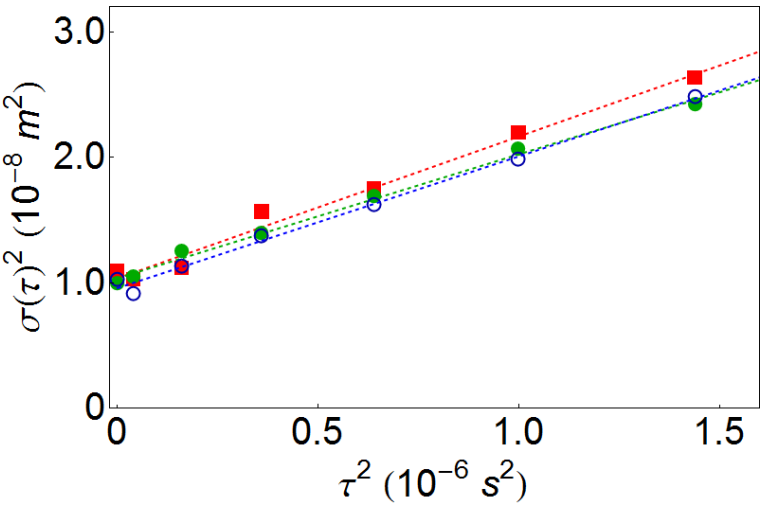

Figure 4.13: (color online) The plot of the square of the width of the released distribution of atoms as a function of the square of the time interval between the release and the measurement. The slope of the linear fit gives the MOT temperature and the y intercept the initial size of the MOT. Red square, green disk and blue circles represents data for LinP, LCP and RCP probe laser respectively.

MOT expansion. The field causes acceleration/deceleration of the atoms depending on their m_F state and direction of velocity. The effect of the magnetic field on $\sigma^2(\tau)$ is $\sim \pm(v_{at} a \tau^3)$, where a is the magnitude of acceleration/deceleration of the atom in the magnetic field and v_{at} is the initial atomic velocity. Maximum a in this case is $\sim$ 15 m/s^2 leading to a worst case error $\sim$ 9%, in the measurement of $\sigma^2(\tau)$. In the current experiment, where the potential energy of the atoms in the magnetic field is much smaller than their kinetic energy, the contribution can be neglected. The effect of gravity is to shift the center of the atomic cloud with time, causing the overlap of the MOT and the cavity mode to reduce faster. The present experiment was performed for a very small time of expansion so that the effect of gravity can be safely be neglected [61] for the measured temperature limit. It is estimated that the error in the measurement due to gravity would cause a maximum error of $\sim$ 20 kHz in VRS for the maximum τ, which is well within the statistical error bars of the measured VRS, and is therefore not corrected for.

Table 4.2: Measured temperature of the cold atomic cloud for linear (LinP), left and right circularly polarized (LCP and RCP) probe light and the corresponding measured g_0 value. One standard deviation errors are shown for each temperature value.

Probe Polarization	g_0 (kHz)	T_{MOT} (μK)
LinP	130	115 ± 9.4
LCP	141	101 ± 5.7
RCP	138	107 ± 7.3

4.5 Discussion

MOT densities are low enough for the atoms to be non-interacting and there is little contribution from any potential energy or interaction terms, in the present single MOT experiment. Therefore the method does measure the temperature of the MOT. When one considers loading cavities with mixtures of interacting cold species in their respective traps, the technique can be adapted to measure the inter-species interaction [62], with minimal perturbation of the overall system. As an example one could use this method for the determination of ion-atom interactions and atom temperature in mixed ion-atom systems [3, 5, 6, 16, 63]. The fact that the measurement takes place within a milli-second, allows for repeated and frequent measurement. Since a cavity supports only a narrow band of frequency, it can be used to selectively interrogate the properties of a specific species in atom mixture experiments, to be performed in the near future. The demonstration that the atom-cavity system can be pushed into strong coupling and this can be detected whether we probe on an open or a closed transition allows for flexibility in detection. This is significant because in the presence of other fluorescing atoms/ions, the frequency of the probe light for one set of atoms, might coincide with

resonant build up from fluorescing atoms/ions of the other species, in one of the many transverse cavity modes, and saturate the detector. If several options are available for interrogation, as demonstrated here, this problem can be avoided to a very good extent. For atom−cavity systems, this technique therefore represents a versatile method for measurement of temperature and other properties of cold atomic ensembles.

CHAPTER 5

Ion trap and ion-atom interaction

5.1 Overview

The study of atom-ion mixture in ion-neutral hybrid trap opens up the possibility of studying interactions at collisional energy below 1eV. The ion induces dipole moment on the atom which offers the study of relatively short range $1/r^4$ type interactions. A handful of experiments has been constructed and applications ranging from collision studies, few particle processes to ultracold chemistry have been experimentally demonstrated in these experiments. In such trapped mixtures of ions and atoms, the ion trap utilize linear Paul trap as it provides the large amount of optical access required. In our hybrid apparatus, we develop a modified quadrupolar Paul trap using thin tungsten wire electrodes with large optical access such that it is geometrically consistent with the requirements of the experiment. The design of this ion trap is inspired by a configurationally similar wire trap for neutral cold polar molecules [20]. Further, the precise design of the trap ensures the need for overlapping the trapped ion atom mixture with the mode volume of the Fabry-Perot cavity, so that entirely new methods of manipulating and detecting the mixtures can be developed. In this chapter, we demonstrate the operation of the ion trap, establish a mechanism for detection of the trapped ions and characterize the trap both numerically and experimentally for $^{85}Rb^{+}$ ions. We also demonstrate the stabilization in the number of trapped ions when held together with the cold atomic ensemble and attribute it to the sympathetic cooling of the ion by the atoms. Finally we propose a method for cavity mediated detection of the trapped ion and probing the ion-atom interaction for the study of mixed species systems.

5.2 The ion trap

The thin wire ion trap consists of 4 square-shaped loops of tungsten wires of diameter 80 μm, separated by 1.5, 3 and 1.5 mm, respectively, and held taut by winding over a scaffolding provided by four stainless steel rods in quadrupolar geometry (Fig.5.1). Detail of the construction of the trap is given in chapter 3. The wires are electrically isolated by the ceramic (Macor) spacers. The inner two wires are supplied with a time varying radio-frequency (rf) voltage, and the outer wires are held at a constant DC voltage with respect to the experimental ground. The rods around which the wires are wound can themselves be biased in order to influence the position and trajectory of the ions. These are normally kept at the ground potential while the trap is in operation.

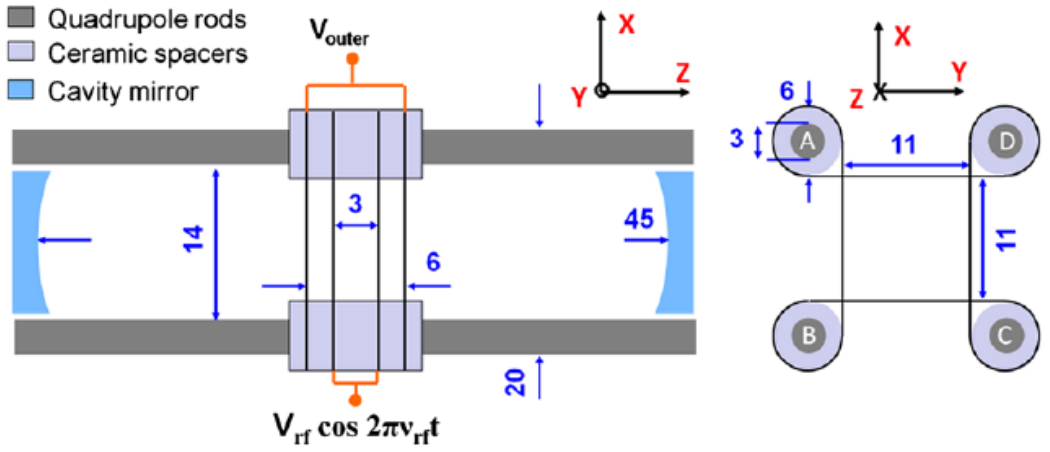

Figure 5.1: Side and axial view of the ion trap containing 4 square shaped tungsten wireloops wound over four quadrupole rods A, B, C, and D. The outer pair of wires are biased with constant voltage V_{outer}, and the inner pair of wires are biased with a time varying radio-frequency voltage V_{rf} at frequency $\Omega_{rf} = 2\pi\nu_{rf}$. All dimensions are in mm.

Another pair of tungsten wires are wound (not shown in the figure), in square and criss-crossed configuration, around ceramic sleeves mounted on the SS rods in front of the ceramic plate holding the cavity mirror attached to the ring pzt. The high voltage on the pzt may effect the performance of the trap. The pair of square and criss-cross wound tungsten wires are maintained at ground during the operation of the trap and shields the pzt voltage from penetrating the center of the trap.

5.3 Loading of ions

The $85Rb^+$ ions are created from the magneto optically trapped $85Rb$ atoms by resonant two photon ionization (TPI). The ionization potential (IP) of Rb atom is 4.18 eV [64]. The two photons for ionization here come from the MOT laser (1.59 eV) and a blue laser (Toptica Ibeam smart λ = 473 nm / 2.63 eV). Since the MOT cooling laser is just slightly red detuned with respect to the atomic transition, $5S_{1/2}(F = 3) \leftrightarrow 5P_{3/2}(F' = 4)$, the process is $1 + 1$ resonant TPI. The sum of the energy carried by the red and blue photons is $\sim$ 4.22 eV, slightly higher than the IP of the Rb atom. The advantage of creating the ions in this method are twofold. First, the ions are created at the center of trap, which implies that the loading process is predominantly insensitive to the phase of the trapping voltage. Second, the ions are created almost at the temperature of the MOT ($\sim$ few hundred microkelvin) as the recoil from the ejected electron imparts a little momentum on the ion due to enormous mass ratio. Hence the loading mechanism is very efficient and the daughter ions can easily be accumulated in the ion trap. However, with the passage of time post ionization, the ions are subjected to various heating mechanisms and therefore require a cooling mechanism to continue remaining trapped. Later in this chapter we will show that the trapped ions are sympathetically cooled, when held together with the parent cold atoms. This leads to stabilization in trapped ion number and long lifetime of the $^{85}Rb^+$ ions in the present setup and opens up the possibility of further investigation like reactive chemistry.

5.4 Simulation and results

To find out a good operating region of the trap, extensive simulations were developed. A specialized software SIMION™is used to create the potential profile due to all the electrodes in the chamber. At a time, the potential due to unity voltage on a particular electrode, with all other electrodes at ground, is generated by solving the Laplace equation. The potential arrays are then imported into Mathematica and added with

appropriate weightage (which is the voltage on that electrode) to create a 3D matrix of potential at space. So the total potential is given by

$$V_{tot}(x,y,z,t) = V_{rf}(x,y,z)Cos(\Omega_{rf}t) + V_{outer}(x,y,z) + V_{CEM}(x,y,z) + V_{mesh}(x,y,z) \tag{5.1}$$

Here V_{CEM} and V_{mesh} are the voltages applied on the CEM and the wire mesh in front of the CEM respectively. Fig.5.2 shows the potential on the radial and axial plane passing through the center of the trap. The corresponding field can easily be obtained by differentiating the potential w.r.t. the spatial co-ordinates. The equation of motion of an ion is solved in that field in order to investigate the dynamics in the trap.

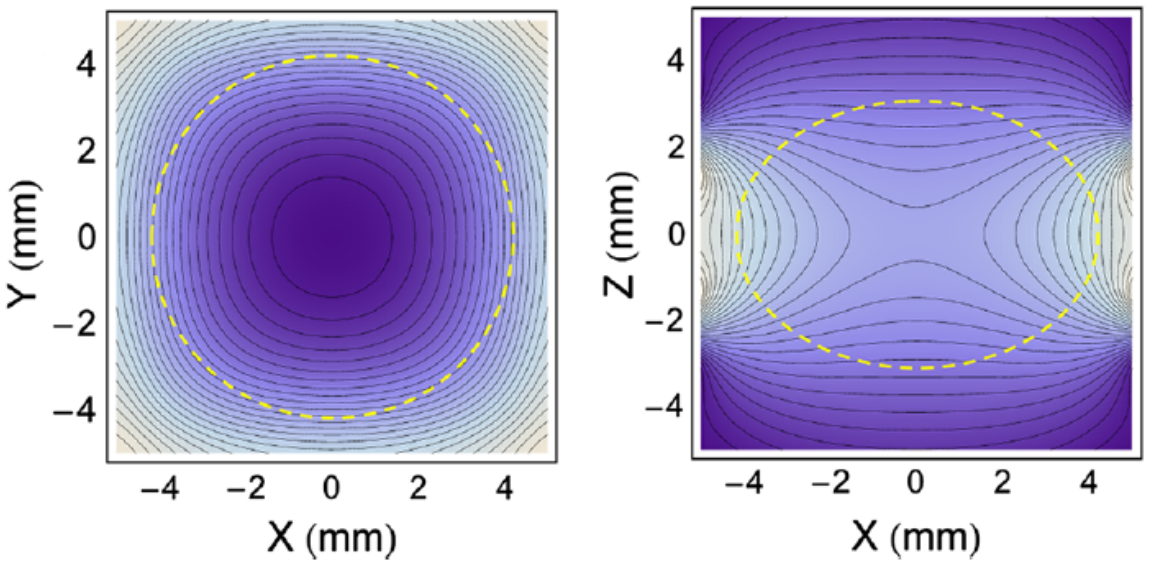

Figure 5.2: Potential profile in XY and XZ planes passing through the trap center. The spatial extent of the stable trapping region is contained within the dashed line, the criterion for which is discussed in section 5.9.

5.4.1 Region of stability

To find out a stable region of operation for a given ion in the trap, we solve the equation of motion of the ion given by

$$\begin{aligned} m_{Ion}\frac{d^2x}{dt^2} &= -Q\frac{\partial}{\partial x}V_{tot}(x,y,z,t) \\ m_{Ion}\frac{d^2y}{dt^2} &= -Q\frac{\partial}{\partial y}V_{tot}(x,y,z,t) \\ m_{Ion}\frac{d^2z}{dt^2} &= -Q\frac{\partial}{\partial z}V_{tot}(x,y,z,t) \end{aligned} \tag{5.2}$$

Here m_{Ion} is the mass of the ion and Q is the charge of the ion. We have always worked with singly charged positive ions. For a given combination of V_{rf} and V_{outer}, a single ion is evolved in the trap for 500 cycles and its position is monitored. If it goes beyond a pre-defined volume within the specified number of cycles, we assume that the ion is lost. If not, we assume it to be a stable operating voltage combination. The simulation is performed for a combination of V_{rf} and V_{outer} at $\Omega_{rf} = 2\pi \times 500$ kHz. The stable points of operation for the $^{85}Rb^{+}$ ion are shown in Fig.5.3(a). Similiar simulation were performed for other possible lighter and heavier ions also at the same Ω_{rf}. Fig.5.3(b) shows the boundary of the stable operating region. It is evident that there are significant overlap in the stability region of multiple ionic species. This opens up the possibility of simultaneous trapping of multiple ionic species and investigate complex collisional physics.

5.4.2 Maximum trappable initial velocity

We also find out maximum initial velocity of the ion that is trappable in our ion trap by a similar simulation. A single ion is loaded at the center of the trap with an assigned initial velocity. Then the ion is evolved in the trap for 500 cycles by solving eq.(5.2) the position is monitored to be inside a defined volume. If the ion goes beyond the volume, we assume the ion to be lost and the initial velocity is high for trapping. In Fig.5.4 we show the maximum inital trapping velocity as a function of the trapping voltage V_{rf}. The simulation was performed at $\Omega_{rf} = 2\pi \times 500$ kHz and $V_{outer} = -5$ V.

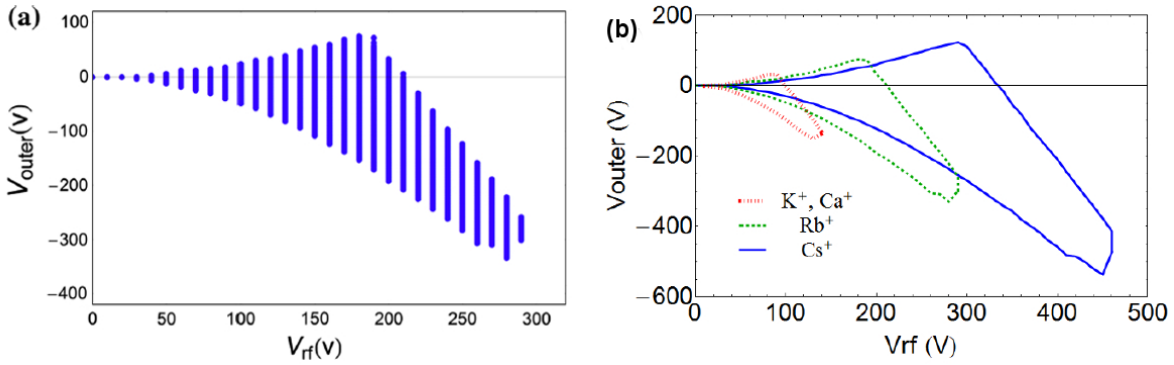

Figure 5.3: (a)The region of stability for a single Rb^+ ion in the trap for a combination of V_{rf} and V_{outer} at $\nu_{rf} = 500$ kHz. (b) The stability region for K^+, Ca^+, Rb^+ and Cs^+ is shown for comparison

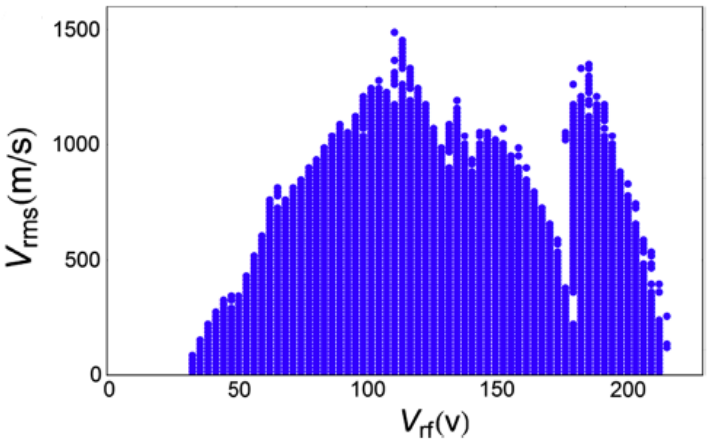

Figure 5.4: Stability plots showing maximum trappable rms velocities of a single Rb^+ ion as function of V_{rf} for $V_{outer} = -5$ V and $\nu_{rf} = 500$ kHz.

5.5 Trapping of ions

While the atoms are ionized, the trap should be operational to contain the ions. The trapping potential is generated by applying a rf voltage (V_{rf}) on the inner pair of wires. This produces a time varying saddle between the radial and the axial directions, as shown in Fig.5.2, providing an effective trapping potential for the ions. A DC voltage on the outer pair of wires can be applied to modify the trap depth in the radial and axial directions. Also, an asymmetric DC voltage combination can be used to translate the ion trap center along the axis in order to have maximum overlap with the MOT atoms.

A small DC voltage can also be applied on the SS rods to shift the trap center radially to maximize over with the MOT. In our experiment, we have systematically maintained equal voltages on the outer pair of wires and all the SS rods are grounded while the trap is operational. The time varying rf signal is produced in a function generator (Agilent: 33512B) and amplified using a wide band rf amplifier (Krohn-Hite: 7602M). As the simulation suggest, the typical range of the parameters used for trapping ions is $400kHz \leq \nu_{rf} \leq 600kHz$ and $70V \leq V_{rf} \leq 120V$. The static voltage on the outer pair of wires is in the range $-15V \leq V_{outer} \leq 10V$.

5.6 Detection of ions

5.6.1 Extraction of ions

The lack of accessible optical transition in Rb^+ ion due to its closed shell structure makes fluorescence detection impractical. In the present experimental setup, a CEM (Dr. Sjuts KBL10RS) is used to detect the ions. Since the cavity and the ion trap share the same axis, axial extraction of the ions is not possible as in ref. [4]. In this experiment, the CEM is placed perpendicular to the cavity axis (along y-axis) at a distance of 44.5mm from the trap center. The CEM is housed in a metallic box, and a mesh is used in front of the cone to shield the high voltage from altering the ion trap potential. The CEM cone is maintained at a voltage of -2.4 kV, and the mesh is biased at -120 V for efficient extraction. The voltages on the CEM and the wire mesh is kept on even during the operation of the trap. Simulation show that this has negligible effect on the performance of the trap. The trapped ions are extracted toward the CEM by switching the left side pair of the quadrupole rods, A and B, to +400 V and keeping the right side pair of rods, C and D, at 0 V (Fig. 5.6). The switching of the extraction voltages on the quadrupole rods is done using a Behlke™(HTS-31) high voltage switch. A simulation, performed in SIMION™, of trapping and extraction of 100 non-interacting ions is shown in Fig.5.6.

Due to design constraints, the drift length of the ions from the center of the trap to the

CEM is much less compared to a typical mass spectrometer. So a large of ions arrives within a very short duration of time. Once an ion has been detected by the CEM, if a second ion arrives within the dead time (8ns) of the detector, then it can not be detected. This pile up problem restricts the number of ions that can be reliably counted to $\sim 100/\mu s$. A partial solution to this problem is given in the following paragraph. Fig.5.5 shows the number of ions detected by the CEM as a function of blue laser power. The number initially increase and then saturates. But we can not conclude whether the nature of saturation is due to the trap saturation or detector saturation.

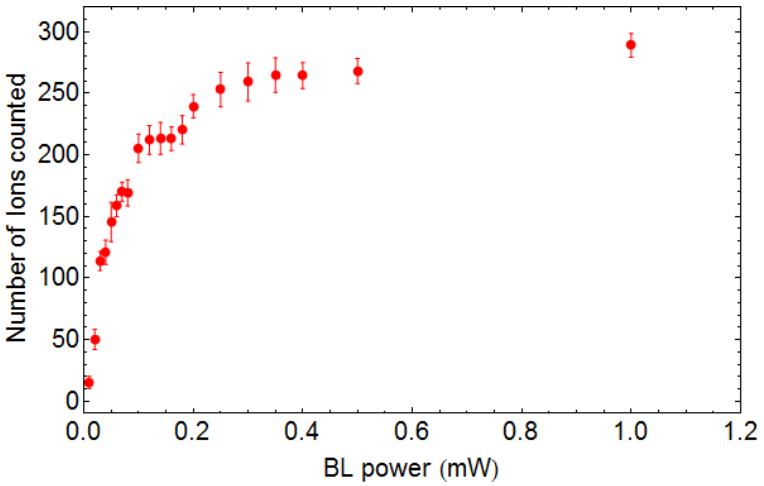

Figure 5.5: Number of ions detected at the CEM as a function of blue laser power. The saturation might be due to pile up of ions at the detector or trap saturation.

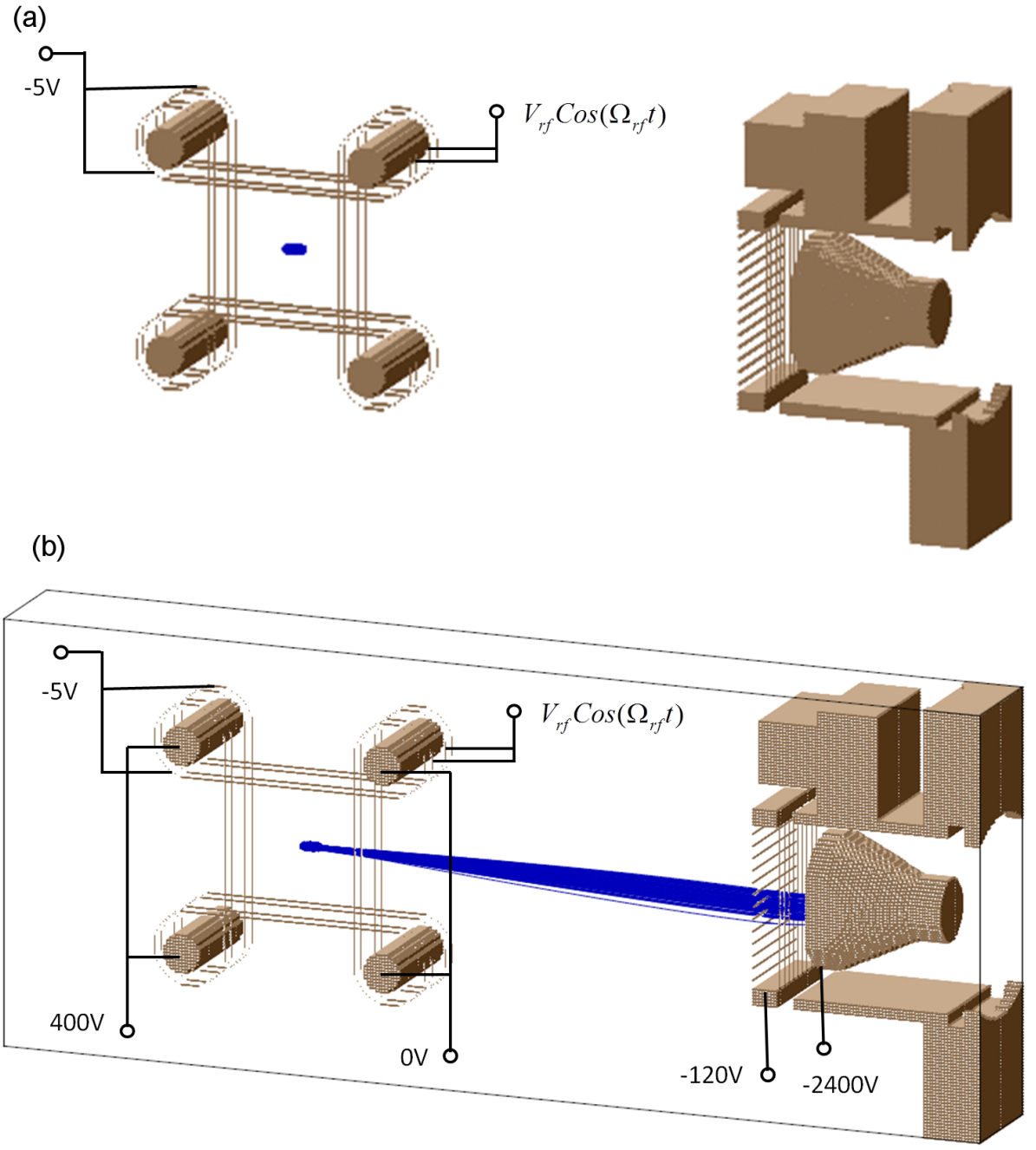

Figure 5.6: A simulation of (a) trapping and (b) extraction of 100 non-interacting ions are shown. The ions are loaded at the trap center at zero initial velocity, evolved for 500 cycles and then extracted onto the CEM. The typical voltage configuration on the electrodes for trapping and extraction are shown.

5.6.2 Dependence of extraction on the phase of trapping voltage

The extraction of the ions is performed while the trap is operational. +400 volt DC on the pair of electrodes A and B, grounded pair of electrodes C and D, -120 volt on the mesh and -2400 volt on the CEM creates a potential slope superimposed on the effective trapping potential which drives the ions out of the trap and accelerates toward the CEM. The field along the line of extraction (y axis in this case) is the resultant of the extraction field and the instantaneous trapping rf field. Hence the field at any point along this line varies in time at the rf frequency. As a result, the peak position and the width of the TOF distribution is significantly affected by the phase of the trapping rf field at which the electrodes are switched on. A detail investigation on this work can be found in ref. [17]. In our experiment, we choose the phase of extraction to be the one with maximum width in TOF distribution. This occurs at phase $\phi = \pi$ of the Cosine trapping rf voltage. The increase in the width of the TOF distribution reduces the pile up at the detector. Fig.5.7(a) shows the real trapping V_{rf} and the 400 volt extraction pulse being switched on at phase $\phi = \pi$. The resultant TOF distribution of the Rb^{+} ions is shown in Fig.5.7(b).

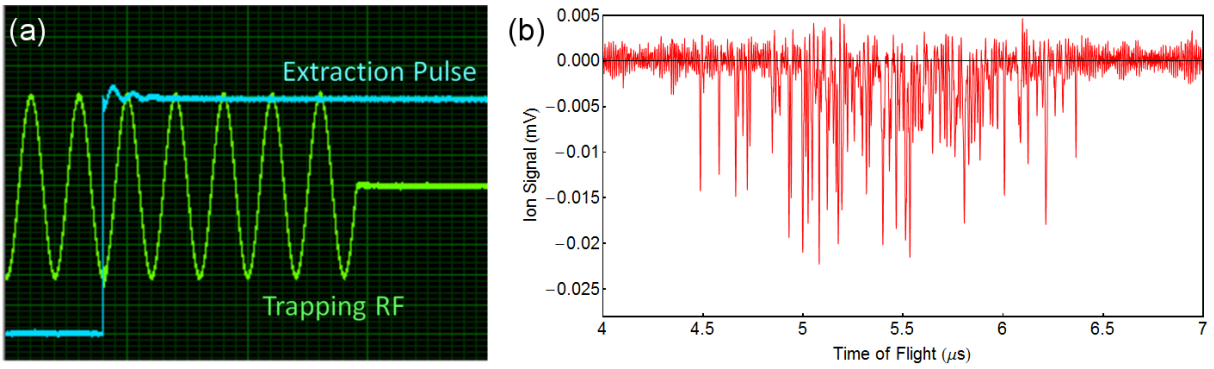

Figure 5.7: (a) The trapping V_{rf} and the 400 volt pulse for the extraction of the ions to the CEM is shown. (b) shows a high density TOF ion signal from the CEM

5.6.3 Counting ion number

To determine the number of ions extracted onto the CEM precisely, two schemes are employed. These are the *pulse counting* and the *integration mode*. In the pulse counting scheme, the arrival of the ion train on the CEM create a corresponding train of current pulses as shown in Fig.5.7(b). These are converted into a voltage signal and measured as 8ns wide negative irregular pulses with amplitudes ranging from a few to several ten milli Volt per pulse. The pulse train is recorded in a digital storage oscilloscope (DSO) and then the number of pulses are counted using an appropriately set discriminator level [4], in the post processing, of approximately 4 mV in the present experiment. Negative peaks with amplitude greater than the discriminator level are counted while the smaller peaks are discarded as noise. Since the data is recorded and therefore always available, it allows for a variety of post processing. A drawback of this scheme is the inability to identify pileup of ions which occurs due to the arrival of more than one ion within the 8ns pulse width. The advantage is that a robust algorithm for pulse counting allows data from several experimental runs to be analyzed in a uniform manner.

In the integration mode, the CEM signal is fed into a low bandwidth amplifier with set amplification factor and the output is recorded on a DSO. The area under the curve, measured in V-μs unit, and a proportionality is established to the number of ions detected. Fig.5.8 shows the ratio of the number of ions counted in *pulse counting* mode and the corresponding area under the curve in *integration mode* method as a function of blue laser power. The calibration gives the constant of proportionality as 5.11 ± 0.23 ions per Vμs. It should be noted that this constant of proportionality is dependent on the CEM bias voltage, the amplifier gain and cut-off frequency. This scheme potentially allows higher ion count rates.

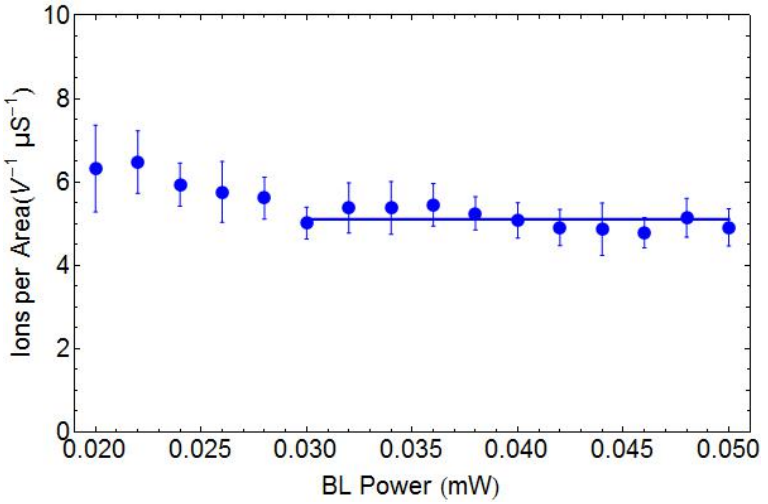

Figure 5.8: Ratio of the number of ions counted in *pulse counting* mode and the corresponding area under the curve in *integration mode* methods as a function of blue laser power. The solid line show the established constant of proportionality. At low ion number limit (low BL power) the *integration mode* gives a higher area due to the low bandwidth of the amplifier. It must be noted that time of ionization for this plot is different than that of Fig.5.5.

5.7 Optimal trapping condition for Rb^+

In this experiment, at a suitable rf frequency of operation (500 kHz), the optimal trapping of the Rb^+ ions rely on two parameters, V_{rf} and V_{outer}. Optimal trapping conditions should ensure long lifetime of the ions and is experimentally determined in two steps. In the first set of experiments the number of trapped ions is counted as a function of V_{rf}. The experiments are repeated at different values of V_{outer} as shown in Fig. 5.9(a). The shift in the trapping region with V_{outer} can be explained from the stability diagram (Fig. 5.3). More negative values of V_{outer} increases the threshold and reduces the range of V_{rf} for stable trap operation. The study allows us to choose $V_{rf} = -5$ V as a good operating regime because it provides a trap depth close to maximum, with a lower threshold and wide range of V_{rf}. The high frequency cutoff of V_{rf} in this experiment comes from the imperfection of the rf arising due to the gain-bandwidth saturation of the amplifier. With the chosen value of V_{outer}, the number of ions in the trap, when held together with the cold atoms, is measured as a function of V_{rf}. Fig.

5.9(b) shows the results for different holdtimes. For longer holdtime, the stable V_{rf} regime shrinks, allowing us to find out $\sim$ 80 V as the most stable V_{rf} of operation for the given trap parameters.

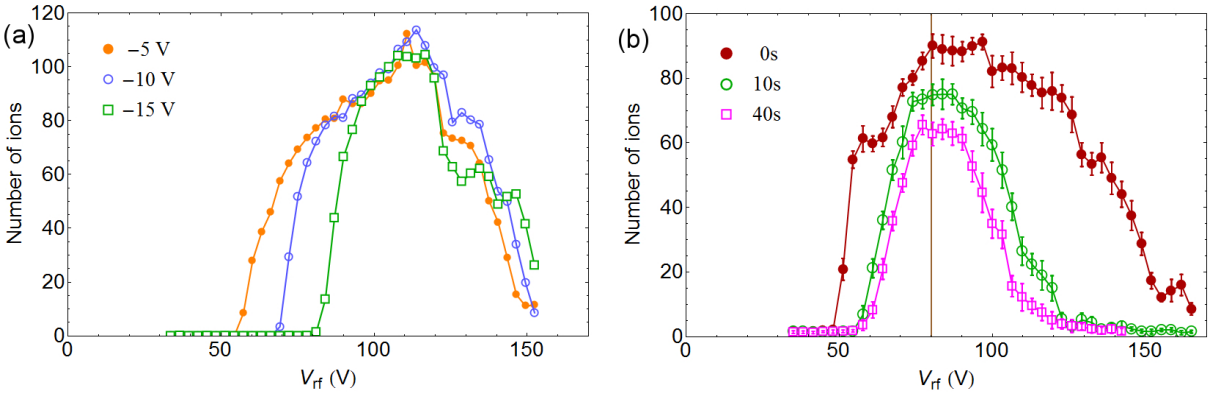

Figure 5.9: Variation in number of trapped ions detected as a function of V_{rf} at 500 kHz for (a) different values of V_{outer} and (b) different trap hold time at V_{outer} = -5 V. All the above measurements were done with the trapped ions overlapped with the cold Rb atoms in the MOT.

5.8 The secular motion and motional resonances

The dynamical trapping of ions in a radio frequency trap leads to motion of the ion that can be decomposed into micromotion and macromotion. The former is induced by the driving rf field and has the same frequency as the driving field. The latter is a slower orbital motion caused by the effective trapping potential. Experimental determination of the macromotion frequencies is done by first trapping ions at the good operating point established above and then applying a weak rf perturbation to the V_{rf}. The trapped ions are held for 10 ms during which a low power rf voltage is mixed in with the V_{rf} before the rf amplifier and applied to the inner wires. The perturbation, scanning in frequency, when in resonance with the macromotion frequencies, results in rapid heating of the ions leading to their ejection from the trap. Fig. 5.10 shows the macromotion resonance spectrum of the Rb^+ ions obtained at $V_{rf} = 80$ V, $V_{outer} = -5$ V and $\nu_{rf} = 500$ kHz. Several resonances are identified as the fundamental, harmonic

and sub-harmonic frequencies corresponding to the oscillation of the Rb^+ ions. From the excitation spectrum in Fig. 5.11, we find the resonance frequencies f_z and f_r to be 54 kHz and 43 kHz respectively.

The experimentally measured macromotion resonance frequencies are independently

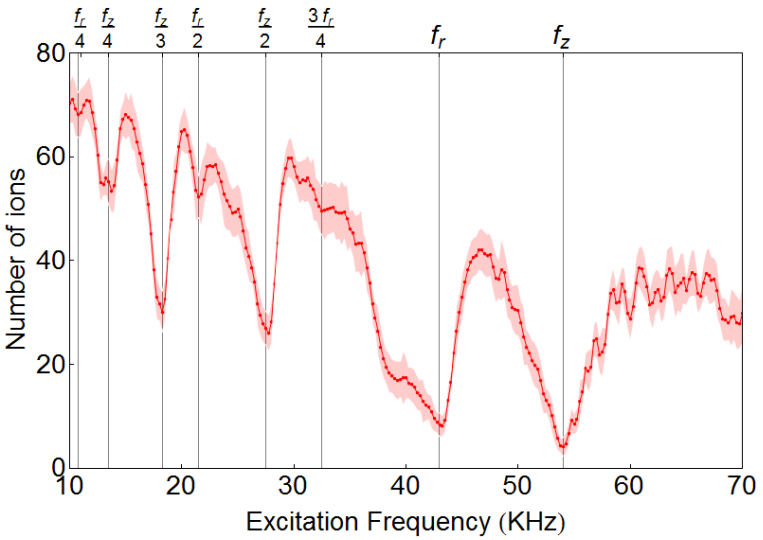

Figure 5.10: Motional resonance spectrum of trapped Rb^+ ions measured at $V_{rf} = 80V$, $V_{outer} = -5V$ and $\nu_{rf} = 500kHz$. The figure illustrates the variation in the ion counts as a function of the excitation frequency, where each point represents the average of 20 measurements, comprising a full cycle of ion creation, trapping, excitation and ion detection. The shaded area represents the standard deviation error.

determined from simulations. Here, the equation of motion of a single ion is solved for 5,000 cycles, in the potential obtained using SIMION™, for the optimized trap parameters. The position of the ion as a function of time is noted as it evolves in the trap. The macro motion frequencies in radial and axial directions are found from the power spectrum (Fig.5.11) of the particle trajectories in the corresponding directions. The measured frequencies agree within a few percent with the macromotion frequencies obtained from the ion trap simulations.

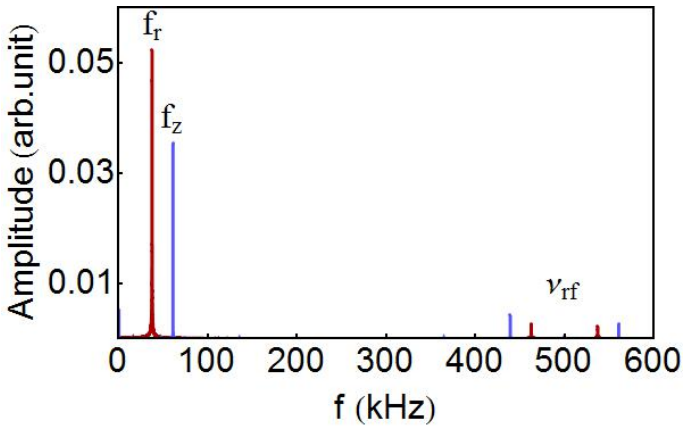

Figure 5.11: Motional resonance spectrum of trapped Rb^+ ions obtained from simulation. The radial and axial secular motion frequencies are identified. The small peak at 500 kHz correspond to the micromotion frequency. The low frequency secular motion creates sidebands around the high frequency micromotion.

5.9 Estimation of trap extent and trap depth

We determine the secular trap depth at the above optimized operating parameters by a combination of simulation and experiment. In the simulation, we determine the maximum spatial displacement that an ion can be subjected to, with zero velocity, and still be trapped. This distance along the x and y axes are found to be 4.2 mm and the displacement is 3.0 mm along the z direction as shown in Fig. 5.12. This is consistent with the potentials illustrated in Fig. 5.2. Substituting these values for maximal displacement into the harmonic oscillator potential energy expression,

$$U_{x,z} = \frac{1}{2} m_{Ion} (2\pi f_{x,z} \Delta_{x,z})^2,$$

where, m_{Ion} is the mass of the Rb^+ ion, $U_{x,z}$ is the maximum secular potential energy, $f_{x,z}$ is the experimentally determined secular frequencies and $\Delta_{x,z}$ is the maximum displacement in the x and z directions respectively, we obtain the secular trap depth. On substitution, we find the secular trap depth is lower in the z direction and has a value of $U_z = 0.46$ eV, which can be regarded as a reliable upper bound on the trap depth.

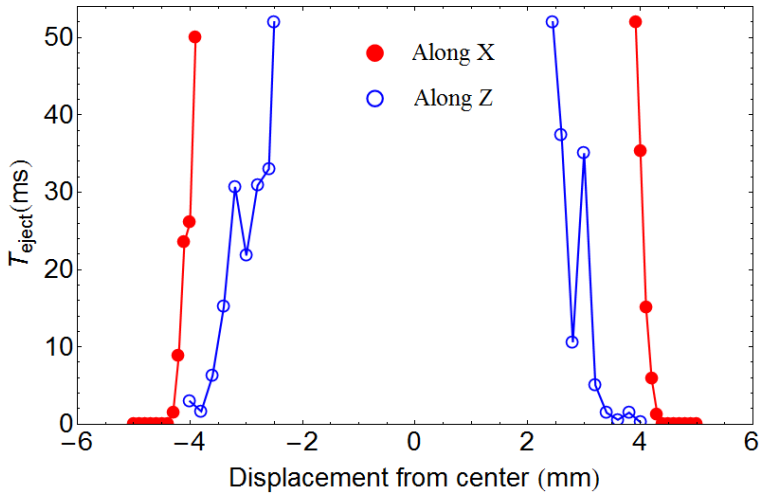

Figure 5.12: The time spent (T_{eject}) by the ion in the trap before it ejects when initial position is displaced along x or z direction is shown. This illustrates the maximum extent of displacement of a trapped ion along the x and z axis. The extreme values represent the outermost turning point for an ion with zero velocity, and therefore the overflow point of the secular trap. The asymmetry along z axis is due to the presence of unbiased electrodes in the set up causing a slight asymmetry in the potential. Therefore in the z direction we take the lower of the two values and define the trap extent as 3.0 mm from the origin.

5.10 Ion-atom interactions: Stabilization of Rb^+ ions

Finally we measure the lifetime of the trapped ions in absence and presence of the cold parent atoms. The lifetime of the ions in an imperfect trap is finite. The loss of ions from the trap due to heating is caused by mainly two factors. Deviation of the trap potential from the ideal quadrupole form and collision induced phase change. However when the ionic ensemble is held together with the localized parent cold atoms, they are cooled by elastic and resonant charge exchange collisions. This leads to stabilization of the number of ions in the trap as has been shown in earlier work [5, 6]. The present experimental system [11], as shown in Fig. 5.13, shows a significant improvement over the earlier works [5, 6] in the lifetime of the trapped ions, in the absence of the cold atoms and a much larger fraction of ions are stabilized when held together with the cold atoms, indicating that the combined ion-atom trap presented here is robust. This

establishes the instrument for hosting a stable ion-atom mixture within a Fabry-Perot cavity.

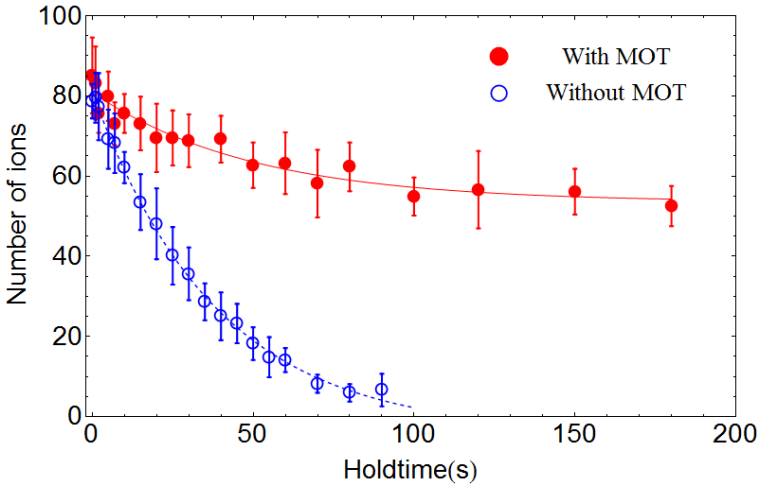

Figure 5.13: Plot showing ion yield as a function of hold time in absence and presence of the MOT. Presence of the MOT leads to longer ion lifetimes attributed to sympathetic cooling. Solid lines are exponential fits without or with an offset for the respective experiments.

5.10.1 Mechanisms of cooling

The Rb^+ ions are cooled when held together with the parent cold Rb atoms. There are two mechanism involved for the cooling [5]. Detail of the process can be found in the ref. [52]. Here we provide a brief description for the understanding of the reader. The first mechanism is elastic collision between the ion and the atom. In every collision the hot ion transfers a tiny fraction of its momentum to the atom. Over multiple elastic collisions, the ion gradually loses its kinetic energy and gets cooled. The second mechanism is resonant charge exchange. In a glancing collision the cold atom transfers its electron to the hot ion resulting in a cold ion and a hot atom. The atom is lost from the trap but the vacancy gets immediately filled as the MOT loading process is continuously on. The cold ion is immediately trapped in the ion trap and again start gaining momentum as it evolves in the trapping potential. The final temperature is an equilibrium between the trap heating rate and sympathetic cooling rate. It must be noted that the cooling of the ion is due to the reduction of macromotion energy. Since the

micromotion is ion position and rf field dependent, any collisional reduction in micromotion velocity is regained instantly post collision, and therefore does not contribute to ion cooling.

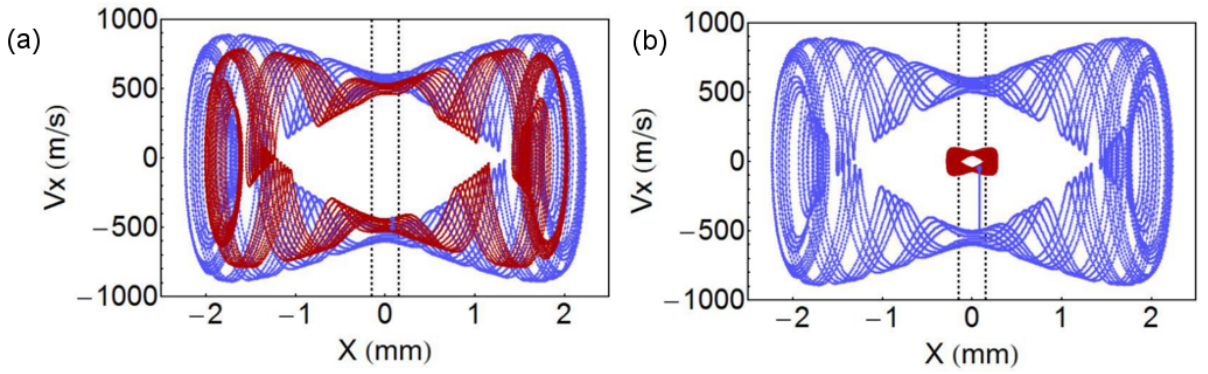

Figure 5.14: The phase space diagram of $^{85}Rb^{+}$ ion before collision (blue) and post collision (brown) with its parent atom. (a) represents an elastic and (b) resonant charge exchange collision respectively. The dashed line shows the typical FWHM of the MOT.

Fig.5.14 schematically describes these two process in phase space. The angle of deflection for the ion in the elastic collision case is 10°. A collisional reduction of macromotion results in a tighter ion orbit, and therefore a cooling of ion motion. Since the macromotion velocity is maximum at the center of the ion trap, where the MOT is located (the MOT volume is much smaller than the ion trap volume), the conditions are ideal for collisional cooling of the ion. While both elastic and resonant charge exchange collisions participate in the cooling of the ion and it is the localized atom distribution which results in collisions exclusively at the trap center that enables the cooling. Both elastic and the charge exchange collision occur at the same spatial point, but the glancing resonant charge exchange is much faster at cooling the hot ion. Although the final equilibrium reached is defined by the elastic process, the glancing collision accelerates the process dramatically. The final temperature of the ions in the trap in this method of cooling is eventually limited by the micromotion velocity which, on an average, can not be reduced.

5.11 Non-destructive ion detection

In our experiment, the trapped $^{85}Rb^{+}$ ions do not have easily accessible transitions for optical detection. So we have to rely on destructive measurement technique (extraction to the CEM) to detect the ions. It is possible to use the ion-atom interaction to detect the trapped ions. But this can not be done with low ion number as the ion-atom collisional loss rate is much lower than the MOT loading rate. In such case the atoms lost by the collision is immediately filled by newly captured atoms and there is no significant effect on the steady state population of the trapped atoms. However if the loading of the MOT is stopped, the collisional loss of the atoms can be easily be probed to detect the trapped ion number. The experimental idea is described below.

Once the MOT reaches its number saturation, a flash of blue laser on the MOT creates the ions. The ions gets trapped as they are created. We wait for a second allowing the MOT to regain the lost atoms. Now the cooling and the repumper lasers are sequentially switched off to create the atomic population in one of the hyperfine ground states. Also the loading of the MOT is stopped in this process. Now we allow the ion-atom mixture to evolve and the atom loss as a function of time can be probed by a VRS experiment at different holdtime(τ).

5.11.1 Theoretical estimation

The number of atoms effectively coupled to a mode of the cavity at any time is given by

$$N_c = \int_v \rho_A(x,y,z)\psi^2(x,y,z)dxdydz \tag{5.3}$$

$\psi(x,y,z)$ is the electric field distribution of the mode supported by the cavity, in this case the fundamental TEM_{00} mode. ρ_A is the atomic density distribution and is given by

$$\rho_A = \frac{N_M}{(2\pi)^{3/2}\sigma^3} Exp\left[-\frac{x^2+y^2+z^2}{2\sigma^2}\right] \tag{5.4}$$

where N_M is the total number atoms in the MOT at any given time. After the cooling is stopped, the atomic cloud goes through ballistic expansion. The Gaussian σ of a cloud

with initial temperature T and FWHM of $2\sqrt{2ln2}\sigma(0)$, after an expansion for time τ is given by

$$\sigma(\tau) = \sqrt{\sigma^2(0) + \frac{k_B T}{m_{Rb}}} \tag{5.5}$$

Although the total number of atom N_M do not change, the ballistic expansion changes the number of atoms coupled to the cavity with time, which can be measured in the vacuum Rabi split given as

$$VRS = 2g_0\sqrt{N_c} \tag{5.6}$$

where g_0 is the single atom-cavity coupling strength as explained in chapter 1. Combining eq.(5.4), (5.5) and (5.6), the time dependence of the VRS with a ballistically expanding cloud can be written as

$$VRS(\tau) = 2g_0\sqrt{\int_v \frac{N_M}{(2\pi)^{3/2}\sigma^3(\tau)} Exp\left[-\frac{x^2+y^2+z^2}{2\sigma^2(\tau)}\right] \psi^2(x,y,z)dxdydz} \tag{5.7}$$

Fig.5.15(a) shows a variation of VRS across $3 \leftrightarrow 4'$ hyperfine transition with time τ. We have chosen parameters consistent with our current experiment.

The ion atom collision cause loss of atoms (N_M) with time which cause further decrease in N_c and hence the measured VRS. The total ion-atom collision rate for cold localized mixture is given as [53]

$$z = \kappa_{ia}\rho_A N_{I;M} \tag{5.8}$$

Here κ_{ia} is the ion-atom collision rate coefficient. In our calculation we use the value $\kappa_{ia} = 1.23 \times 10^{-13} m^3/s$ previously measured in our group [53]. $N_{I;M}$ is the number of ions overlapped with the MOT at a time. If a total number of ions N_I is trapped within the ion trap of volume V_{IT} then

$$N_{I;M} = N_I \frac{V_{MOT}}{V_{IT}} \tag{5.9}$$

V_{MOT} is the volume of the MOT. Assuming that every ion-atom collision causes loss of atoms, we can introduce an atom loss rate γ_{ia} due the ion-atom collisions so that

$$\gamma_{ia} N_M = \kappa_{ia} \frac{N_M}{V_{MOT}} N_I \frac{V_{MOT}}{V_{IT}} \tag{5.10}$$

$$\Rightarrow \gamma_{ia} = \kappa_{ia} \frac{N_I}{V_{IT}} = \kappa_{ia}\rho_I \tag{5.11}$$

ρ_I being the ion density. The rate of change of number of atom in the MOT can be written as

$$\frac{dN_M}{dt} = -\gamma_{ia} N_M \tag{5.12}$$

So starting with an initial number of atoms N_0, the number of atoms remaining in the MOT at time τ is

$$N_M(\tau) = N_0 e^{-\gamma_{ia}\tau} \tag{5.13}$$

Inserting this time dependent atom number in eq.(5.7) gives us the variation of VRS as a function of time in presence of the ions as

$$VRS^{ia}(\tau) = 2g_0 \sqrt{\int_v \frac{N_0 e^{-\gamma_{ia}\tau}}{(2\pi)^{3/2}\sigma^3(\tau)} Exp\left[-\frac{x^2+y^2+z^2}{2\sigma^2(\tau)}\right] \psi^2(x,y,z)dxdydz} \tag{5.14}$$

Fig.5.15(b) show the difference in VRS measured with and without ions.

This method of measuring the loss of atoms from a hyperfine ground state do not restrict us within measuring ion-atom interactions. In fact any loss mechanism of the atoms, collisional or reactive, can be probed using this very general method.

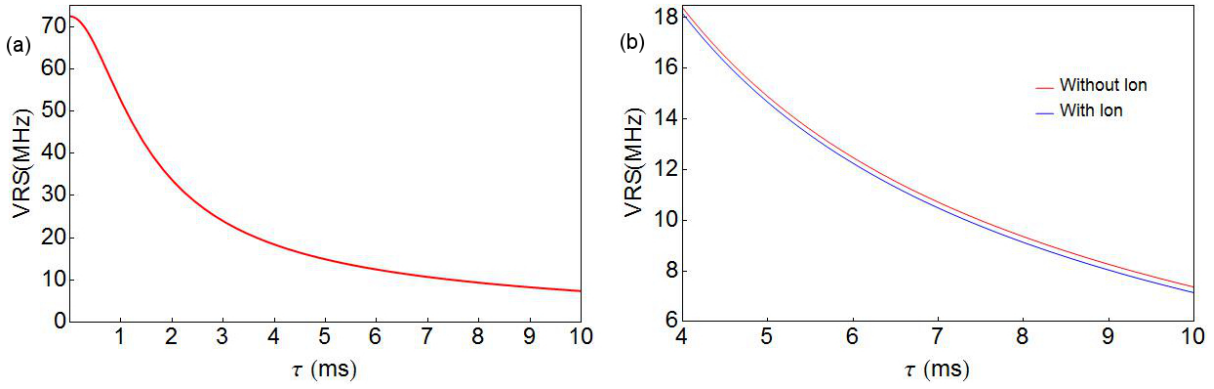

Figure 5.15: (a) VRS against $3 \leftrightarrow 4'$ transition as a function of time when an atomic cloud of 10^6 atoms at an initial temperature of 107μK goes through ballistic expansion. We have taken $g_0 = 0.14MHz$ as suggested by our earlier experiments. (b) Difference in VRS with and without ions with the same atomic cloud. Here we have taken a relatively high ion density of $5 \times 10^7/cm^3$.

5.12 Discussion

We have designed and built a novel thin wire ion trap that is concentric with a magneto-optical trap as a part of the versatile apparatus for the study of inter-species interaction. The open geometry of the trap enables large optical access and allows the trap to be placed within a Fabry-Perot resonator. The trap is characterized both in simulations and experimentally to establish optimal operating parameters. The extent of the trap and the trap depth have been determined at this optimal operating regime. The sympathetic cooling of the ions and hence the stabilization in number was demonstrated. This opens up the possibility of further investigation with stable ion-atom mixture. The axis of the Fabry-Perot cavity passes right through the center of the ion-atom trap allowing the interaction of the mixture to be probed. This can be used to develop a non-destructive detection mechanism of the optically dark trapped ions.

CHAPTER 6

Toward composite objects

6.1 Overview

The ultimate goal of the hybrid apparatus built is to create, trap, detect and study the interactions of composite objects. Stable mixture of composite molecules with atoms or ions allows to study wide range of central potential scattering from $1/r$ to $1/r^6$. The initial step toward the ultimate goal is diatomic molecules and molecular ions. Due to chronologically first experimental realization of the ^{85}Rb MOT, in this thesis we have restricted ourselves within the interaction of ^{85}Rb atoms with the daughter ions and separately with resonant quantized EM field. In this chapter we demonstrate the formation of homonuclear diatomic molecules of ^{85}Rb by photoassociation. We discuss about various possibilities of trapping of neutral molecules within the infrastructure of the apparatus. Finally we demonstrate the formation, short time trapping and detection of $^{85}{Rb_2}^+$ molecular ions along with the $^{85}Rb^+$ atomic ions.

6.2 Photoassociation of $^{85}Rb_2$

Photoassociation(PA) of atoms for production of long range molecules at low temperature is a very effective technique. The idea is illustrated in Fig.6.1. A colliding pair of atoms, in presence of a resonant photon creates a weakly bound excited (electronic) state molecule. The photon must be resonant with one of the vibrational level of the excited electronic state from the ground state atomic asymptote. Close spacing of the vibrational levels near the dissociation threshold makes it convenient to set the photoassociating laser on a resonance by slightly red detuning from the atomic resonance. Due to large overlap of the wavefunctions, a large fraction of the excited molecules decay back to free atoms. However, a small fraction of the excited state molecules may

spontaneously decay to a ground electronic state to form long range (at high vibrational level) ground electronic state molecules. The molecules produced in this process are inherently translationally cold. However in absence of cooling and trapping, they eventually escape out of the region of formation in few tens of milliseconds. So the presence of a PA laser introduces a loss mechanism for the MOT atoms. Photoassociation spectroscopy can be performed by scanning the PA laser in frequency and monitoring the dip in the MOT fluorescence to identify the resonances. It must be noted that a dip in the MOT fluorescence corresponds only to molecule formation in the electronically excited state and does not ensure that the molecule decays to the ground electronic state. In any event, due to Frank-Condon overlap, the electronic ground state molecule produced in this manner would be vibrationally highly excited.

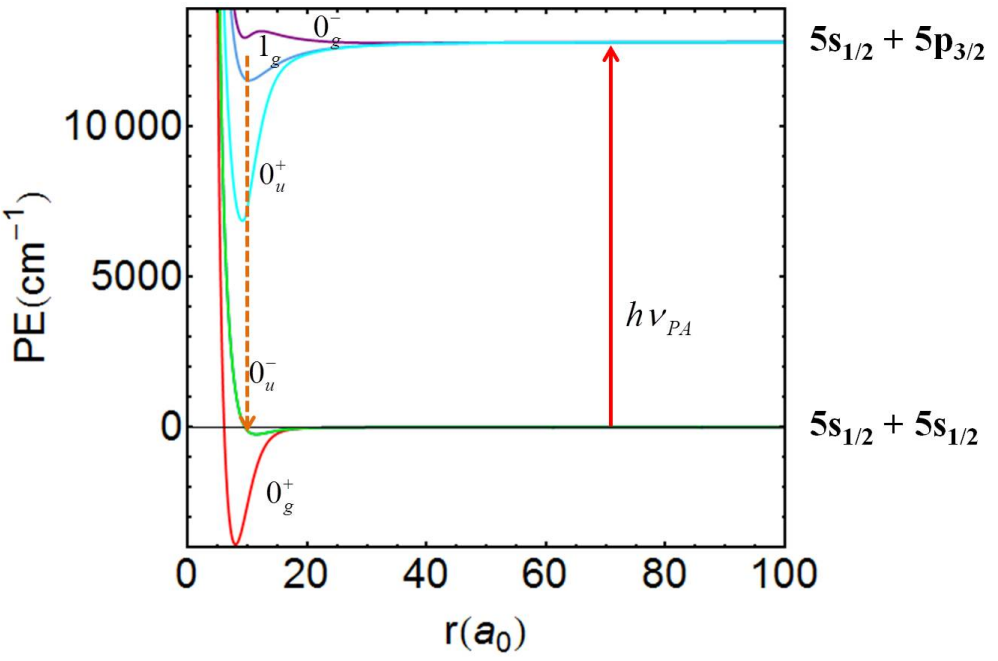

Figure 6.1: The photoassociation scheme for rubidium.

6.2.1 Experiment and result

The photoassociation laser is primarily derived from a homebuilt ECDL. The laser is $\approx 60GHz$ red detuned from the $5S_{1/2}(F = 3) \leftrightarrow 5P_{3/2}(F' = 4)$ atomic transition of ^{85}Rb. The frequency of the laser can be scanned $\approx 20GHz$ without mode hop by ap-

plying a voltage ramp on the pzt of the external cavity of the ECDL. The laser power is amplified using a tapered amplifier (TA) and the output of the TA is coupled into a single mode polarization maintaining fiber (SMPMF) to deliver to the experiment. One part of the laser light, before injecting into the TA is coupled to a wavemeter to monitor the wavelength. Detail of the laser arrangement is provided in chapter 3. The collimated laser light out of the SMPMF is focused by a 200 mm focal length lens on the MOT. The focusing serves two purpose i) It increases the peak intensity of the PA light on the MOT. ii) The small beam size can easily pass through the wire mesh (ion trap). This dramatically reduces the scattering of the light from the tungsten wires to provide a less noisy background for fluorescence detection of the MOT.

First, the MOT is loaded to its number saturation. The PA laser light is then allowed

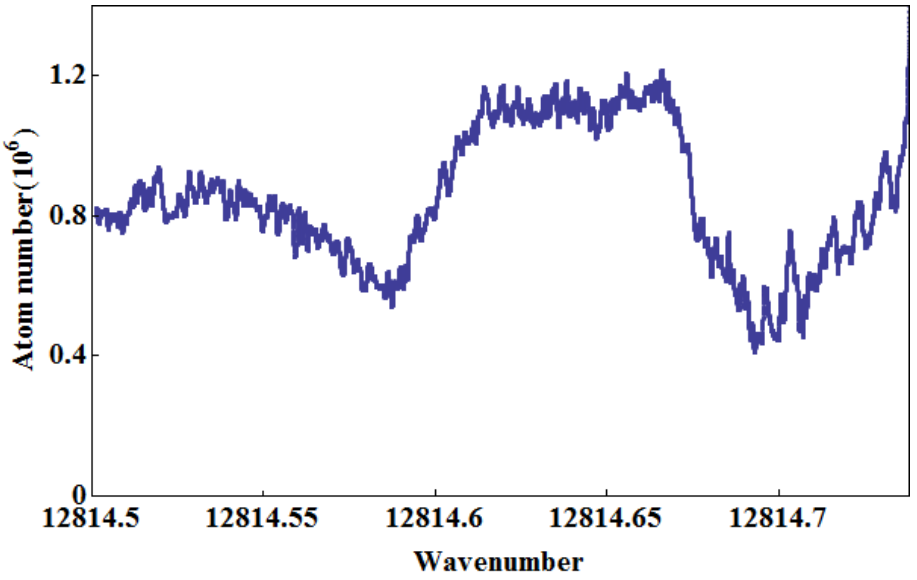

Figure 6.2: The dip in the MOT fluorescence when the PA laser is scanned in frequency.

to fall on the MOT by opening a mechanical shutter installed in the path the laser. The fluorescence of the MOT is monitored (as described chapter4) while the PA laser is scanned in frequency. The dip in the fluorescence corresponds to photoassociation resonance. Fig.6.2 shows a typical spectra while the PA laser is scanned from 12814.5 cm^{-1} to 12814.75 cm^{-1} .

The spectra shown is not as clean in compared to spectra obtained in another experiment in our lab [65]. This is due to the dips caused by the atomic fluorescence getting

coupled into the cavity whose length is drifting due to thermal instability. In addition, the scatter of PA light from the thin wires gives rise to optical noise in the MOT fluorescence signal. Active stabilization of the cavity may lead to better spectra as would oeperating with a dark spot MOT. Stabilization of the PA laser on one of the PA resonances will allow us to produce molecule at a constant rate.

6.2.2 Possibilities of trapping neutral molecules

The hybrid apparatus provides several possibilities of trapping the cold molecules produced by photoassociation or any other means. The cavity can be used to form a standing wave which has a high electric field gradient between the node and the anti-node. The neutral molecules can be dipole trapped in the cavity anti-nodes using a far red-detuned trapping light. In fact the enhanced light intensity in the cavity can be used for efficient photoassociative production of the molecules also.
Heteronuclear diatomic molecules can be produced in the apparatus using photoassociation in a manner similar to the production of homonuclear molecules. The heteronuclear molecules have permanent dipole moments. So it can be confined in an electric field gradient trap in a way demonstrated by ref [50]. The gradient electric field can be easily produced by applying DC bias voltages on the thin tungsten wires. Such a trap utilizes the Stark shift of molecules to confine the molecules in weak field seeking states, at the geometric center, where a local minima of the gradient electric field is formed.

6.3 Production and trapping of molecular ions

Cold Rb_2 molecules are spontaneously formed in the MOT by long range photo association of the atoms in the presence of the cooling laser light [66, 67]. A fraction of the photo associated molecules decay to vibrational levels of the ground electronic molecular state. We perform resonance enhanced two photon excitation (RE2PI) of the ground state molecules to create the molecular ions. Fig.6.3 explains the scheme. The

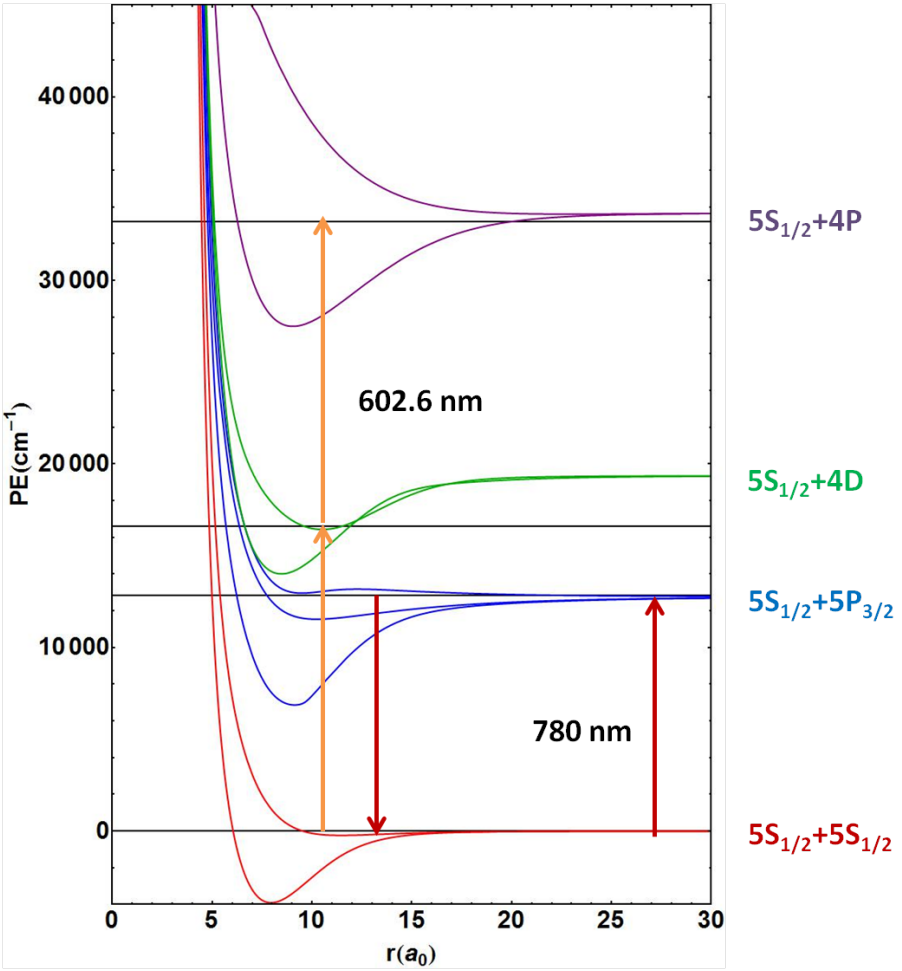

Figure 6.3: The scheme for production of Rb_2^+ molecular ion.

780 nm cooling laser creates a small number of ground state molecules near the dissociation limit. The molecules produced in this process have the same initial temperature of the atom. The low initial velocity allows the molecules to spend some time within the MOT volume before they ballistically fly out of the region. Hence for a continuously loading MOT, with a particular power and detuning of the cooling laser, there is always a steady population of ground state molecules that is present within the MOT volume. Two photons of 602.6 nm ionize the newly formed molecule, via an intermediate resonant molecular electronic-vibrational state to create a molecular ion near asymptote. Due to low Frank-Condon overlap of the transitions, one needs high intensity lasers to make the process efficient. In our experiment we use a pulsed dye laser (wavelength set to 602.6 nm, pulse duration 1-2 ns) pumped by the second harmonic

of a Nd:YAG ns pulsed laser (10 Hz repetition rate).

The 602.6 nm photons also ionize a ^{85}Rb atom from its $5P_{3/2}$ excited state. So in the

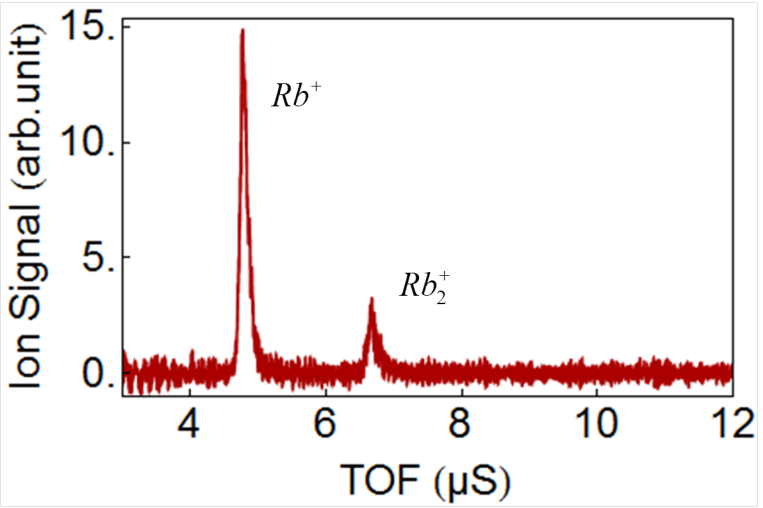

Figure 6.4: Time of flight signal of simultaneously trapped Rb^+ and Rb_2^+. The ion trap is switched off before the extraction.

process of creation of molecular ions, we also get a large number of atomic ions. In fact, due to higher atomic density the number of atomic ions produced per pulse are much larger than the molecular ions. As a consequence we produce a mixture of atomic and molecular ions, where the number of atomic ions dominates.

The optimal trapping parameters for $^{85}Rb^+$ is not suitable for trapping of Rb_2^+ ions because of its double mass. Hence we operate the trap at $V_{rf} = 150V$ ($\Omega_{rf} = 2\pi \times 500$ kHz) with the other parameters kept unchanged. Once the MOT reaches its number saturation, the dye laser pulse is allowed to incident on the MOT at a 10 Hz repetition rate. The trap is operational while the ions are created from the pulsed dye laser. After the arrival of the pulse and creation of the ions the trap is kept operational for another 200μs, which equals to 100 RF cycles of 500kHz, to examine the simultaneous trapping of the atomic and molecular ions. Finally the trap is turned off and the ions are extracted onto the CEM by turning on the extraction electrodes immediately. The TOF signal is recorded in an oscilloscope for post processing. Fig.6.4 show a sum of 4000 TOF signal. The large peak at TOF = 4.6μs correspond to Rb^+, whereas the smaller peak at TOF = 6.5μs correspond to Rb_2^+. The signal clearly indicates that it is possible

to simultaneously trap Rb^+ and Rb_2^+ ions, at least for a short period of time, in our apparatus.

6.4 Discussion

In this chapter we have demonstrated some preliminary results toward formation of composite objects in our apparatus. Formation of cold neutral Rb_2 molecules by photoassociation was demonstrated. Rb_2^+ molecular ions was formed, trapped and detected. Although further investigation is required in these fronts toward achieving a stable mixture of composite objects, the preliminary demonstration establishes the credibility of the hybrid apparatus as a universal platform for the study of mixtures at cold temperature.

CHAPTER 7

Summary and future prospects

7.1 Summary of the results

We have planned, designed, built and implemented a hybrid apparatus for the study of multispecies interactions at low temperature. The unique apparatus combines a MOT and an ion trap that is spatially overlapped with the MOT. Both, MOT and the ion trap can be simultaneously operated. The combined trap is positioned within a moderate finesse Fabry-Perot cavity. The geometrical design of the apparatus ensures that the center of the MOT, ion trap and the cavity coincides. Further, the apparatus offers possibility of trapping cold neutral molecules within its geometry. The details of the design and construction of the apparatus have been discussed.

A MOT of ^{85}Rb atoms was formed inside the apparatus. Number of atoms captured in the MOT and the spatial density was determined. The collective strong coupling of the cold atoms with the fundamental mode of the cavity was studied. Vacuum Rabi splitting (VRS) was observed as a signature of the collective strong coupling. VRS was measured, as a function of atoms coupled to the cavity mode, for both open and closed atomic transitions with linear and circularly polarized light. The single atom-cavity coupling strength g_0 was experimentally determined from the measurement and it agrees closely with the theoretically calculated values. The knowledge of g_0 was used for experimentally determining the number of atoms coupled to the cavity as a function of time for a ballistically expanding cloud. The initial temperature of the cold atomic ensemble was measured from the measurement.

We demonstrate the operation of the modified spherical Paul trap, built using thin tungsten wire electrodes, with $^{85}Rb^{+}$ ions. The trap was characterized in detail, both experimentally and in simulations for the same ion. Efficient loading, trapping and detection (by extraction onto a CEM) mechanism were established for the optically dark

ions. The optimal trapping parameters of the ion trap were established experimentally and its was found to be well within the regime suggested by the simulations. We found out the radial and axial secular motion frequencies of the trap experimentally, by resonant excitation of the trapped ions. The extent of the trap was determined from simulation. Combining these two results we determined the trap depth for $^{85}Rb^{+}$ ions. The stabilization of the ion number in the trap, when held together with the parent cold atom were observed and it was attributed to sympathetic cooling of the ions by the cold atoms. Further, we proposed a scheme for non-destructive detection of the ions by using the ion-atom-cavity interaction as a probe.

Formation of homonuclear Rb_2 molecules using photoassociation was demonstrated in the same apparatus. Schemes for trapping of neutral molecules within the scope of the apparatus was discussed. Finally, we demonstrate creation of Rb_2^{+} molecular ion by resonance enhanced two photon excitation from the spontaneously formed long range molecules in the MOT. The molecular ions can be simultaneously trapped in the thin wire ion trap, with the atomic ions generated in the same process. A mass spectrometry was performed for detection of the atomic and the molecular ions.

7.2 Future prospects

Within the scope of this thesis we have performed experiments with the ^{85}Rb atoms, the daughter $^{85}Rb^{+}$ ions and homonuclear neutral molecule and molecular ions created from the cold atomic ensemble of ^{85}Rb. The atoms are derived from getter sources. Our hybrid apparatus contains sources of other atomic species also. A list of installed dispensers and the isotopes is given in chapter 3. This opens up the possibility of studying a variety cross species ion-atom interactions. In a combination of $^{85}Rb^{+}$ ions with ^{87}Rb atoms (or vice-versa) resonance charge exchange process is highly suppressed. So processes driven by only elastic scattering can be well studied. This kind of mixture also provides an ideal platform for the study of isotope effects in cold reactive

chemistry. The presence $^{39/40}K$ and ^{133}Cs along with $^{85/87}Rb$ provides an opportunity to study ion-atom interactions with different mass ratio and experimentally establish a general method for sympathetic cooling with localized ensemble. Further, transitions of $^{40}Ca^{+}$ ion are optically accessible which opens up the possibility of laser cooling and forming ion crystals. Also the ions can be optically detected and state prepared. Interaction of the cold atomic clouds with $^{40}Ca^{+}$ ions offers the study of a whole new set of problems with the ease of in situ optical detection.

The presence of the cavity allows frequency sensitive interrogation of the species within. The cavity was developed as a tool for probing any interaction that causes loss of atoms. The high intensity of light in the cavity mode may be used for efficient photoassociation to form molecules within the mode. The enhanced spontaneous emission into the cavity mode may be used as a detection tool for the molecules. Further, high electric field gradient in the cavity mode standing wave offers the possibility of dipole trapping the neutral atoms of molecules.

The thin wires electrodes used for the ion trap can also be used to apply high electric field at the center of the apparatus which can be useful in many ways. An electrostatic trap for bipolar molecules, as discussed in chapter 6, can be developed. Also it can be a useful tool to align dipolar molecules or define a quantization axis for a quantum system.

Altogether the versatility of the hybrid apparatus offers a variety of experimental systems and interesting physics that can be explored in future.

APPENDIX **A**

Mechanical drawing of the apparatus

We provide the detail of the mechanical drawing of the apparatus. Each figure shows a crutial part of the instrument. All dimensions are given in milimeter (mm). The components are assembled inside a spherical hexadecagon stainless steel chamber (Kimball physics Inc: MCF600-SphHexadecagon-F2A16). The apparatus is attached to the inner wall of the chamber using groove grabbers (Kimball Physics: MCF600-GrvGrb-C01). The mechanical drawing of the chamber and the groove grabber are available from Kimball physics Inc.

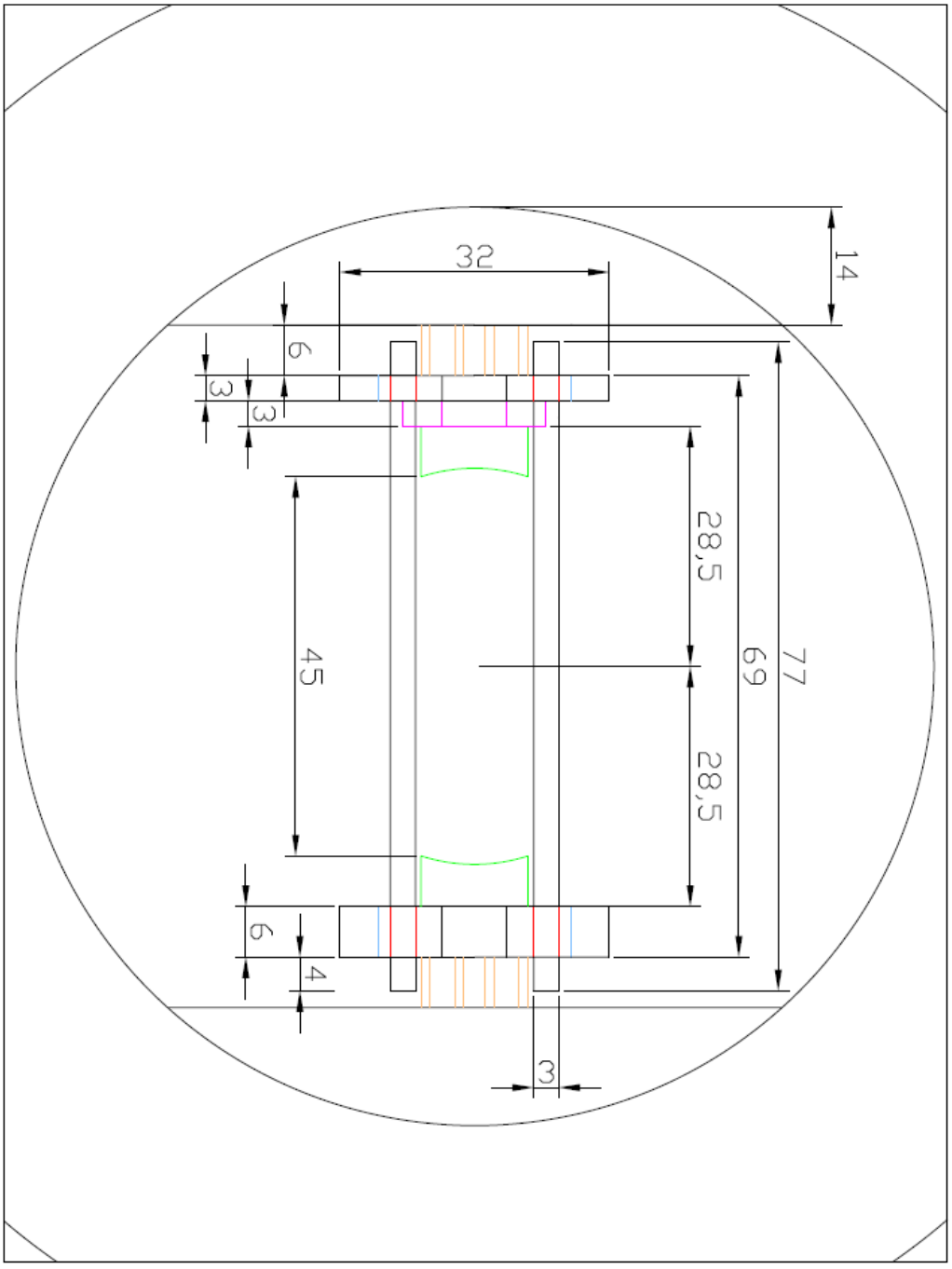

Figure A.1: The assembled apparatus.

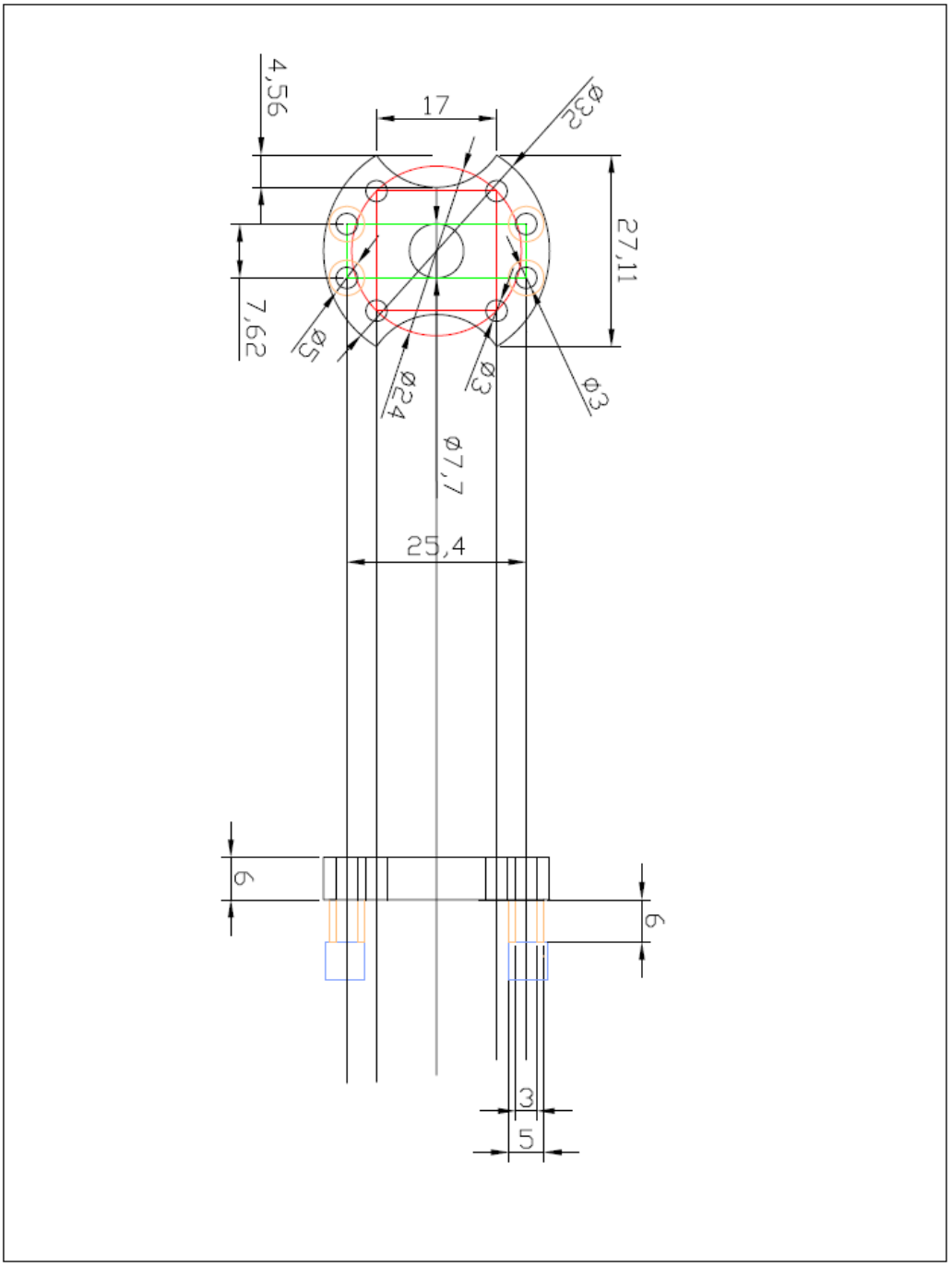

Figure A.2: The Macor plate and the mounting scheme of the plate to the groove grabber using stainless steel spacers.

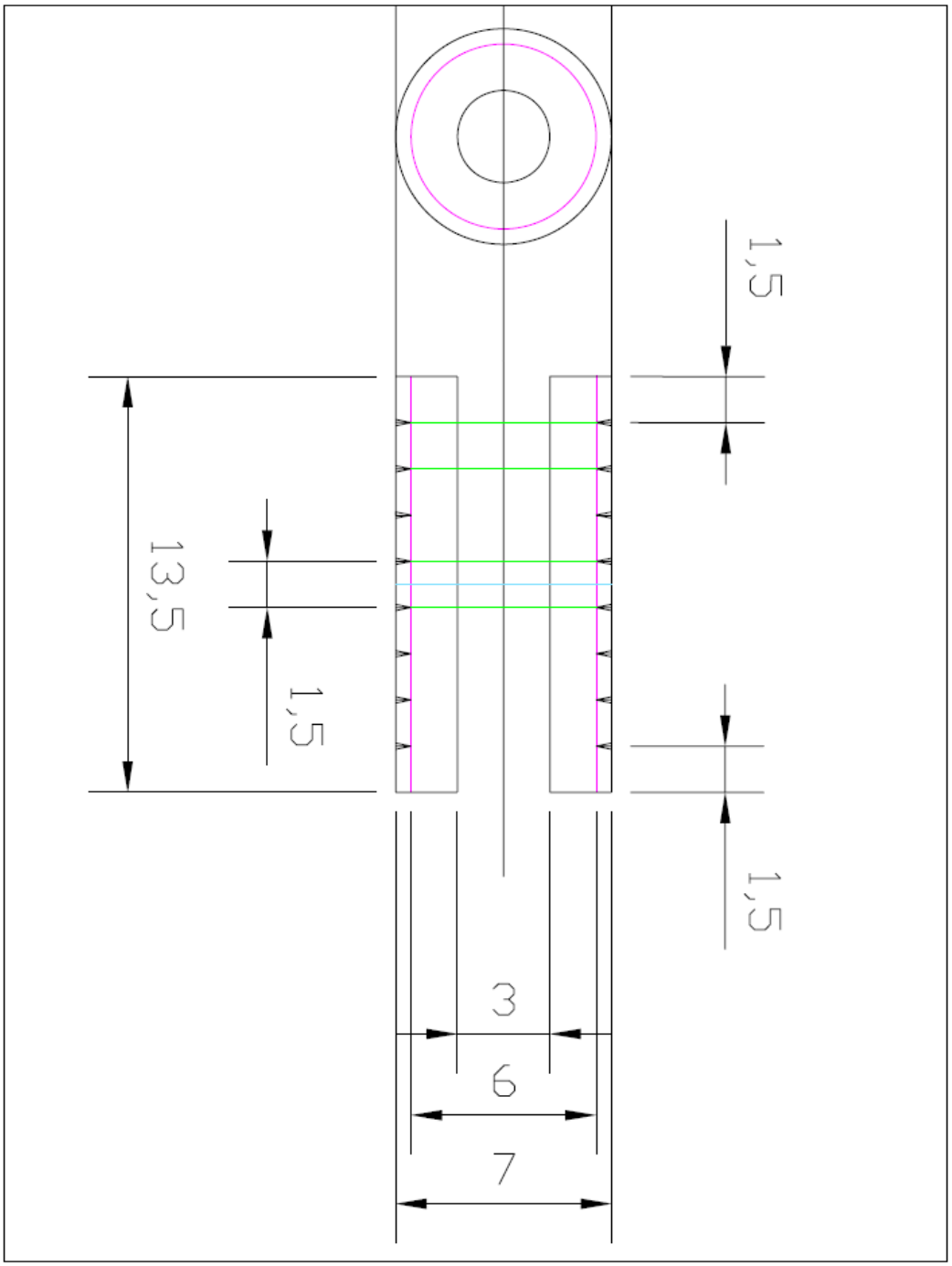

Figure A.3: The grooved ceramic sleeve on which the thin wire trap is scaffolded.

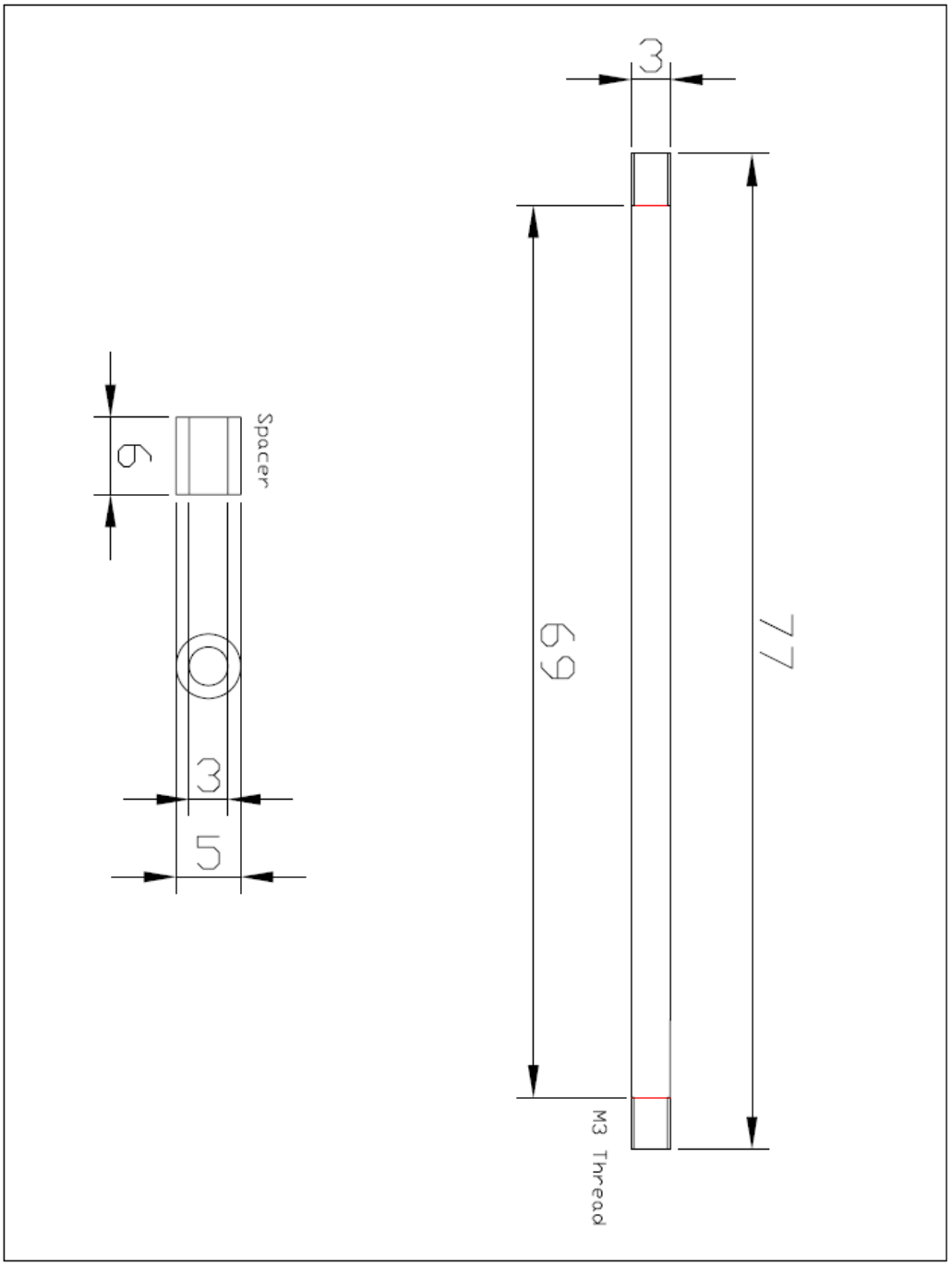

Figure A.4: The stainless steel rod for coupling the Macor plates and the stainless steel spacers to attach the Macor plate to the groove grabber.

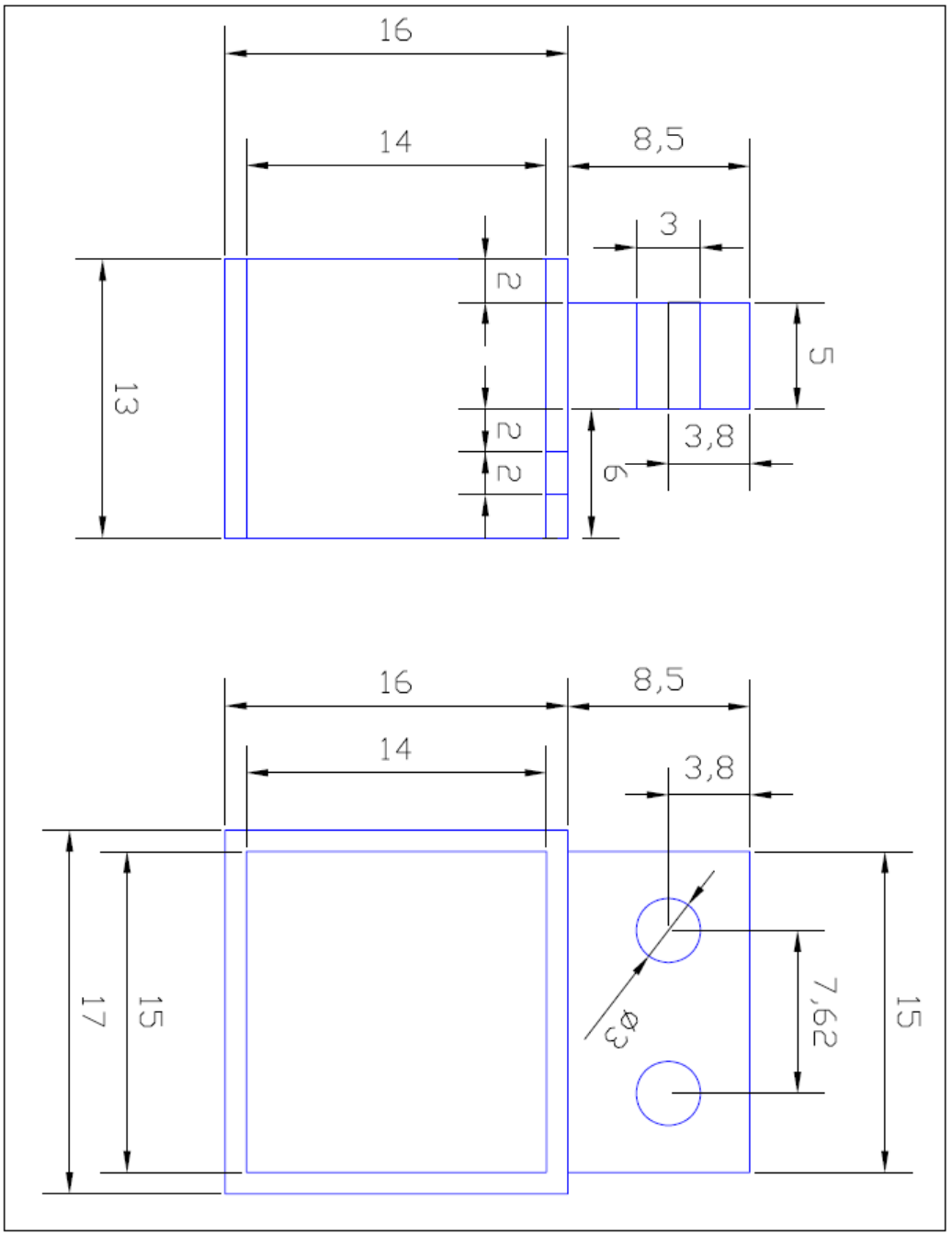

Figure A.5: The aluminum housing of the channel electron multiplier.

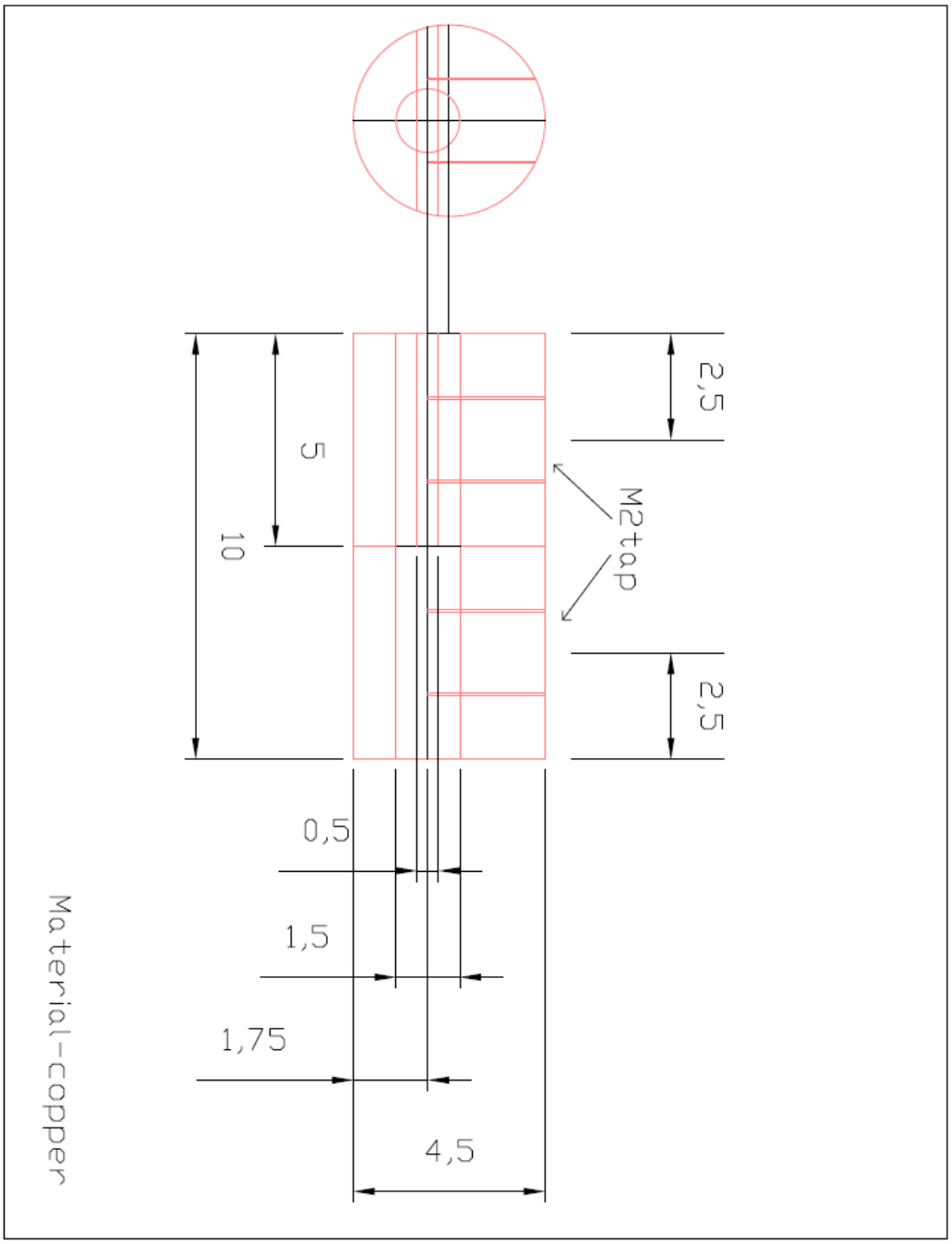

Figure A.6: The copper bead connector to the feedthrough. The connector contains an off-axis through hole and a horizoltal slot for attaching the connections.

Bibliography

[1] C. Zipkes, S. Palzer, C. Sias, and M. Köhl. A trapped single ion inside a bose-einstein condensate. *Nature*, 464:388, 2010.

[2] S. Schmid, A. Härter, and J. H. Denschlag. Dynamics of a cold trapped ion in a bose-einstein condensate. *Physical Review Letters*, 105:133202, 2010.

[3] Felix H. J. Hall and Stefan Willitsch. Millikelvin reactive collisions between sympathetically cooled molecular ions and laser-cooled atoms in an ion-atom hybrid trap. *Phys. Rev. Lett.*, 109:233202, Dec 2012.

[4] K. Ravi, S. Lee, A. Sharma, G. Werth, and S.A. Rangwala. Combined ion and atom trap for low-temperature ionatom physics. *Applied Physics B*, 107(4):971–981, 2012.

[5] K. Ravi, Seunghyun Lee, Arijit Sharma, G. Werth, and S.A. Rangwala. Cooling and stabilization by collisions in a mixed ion-atom system. *Nat Commun*, 3:1126, 2012.

[6] I. Sivarajah, D. S. Goodman, J. E. Wells, F. A. Narducci, and W. W. Smith. Evidence of sympathetic cooling of na^+ ions by a na magneto-optical trap in a hybrid trap. *Phys. Rev. A*, 86:063419, Dec 2012.

[7] Min Xiao Amitabh Joshi. *Controlling Steady-state and Dynamical Properties of Atomic Optical Bistability*. World Scientific, 2012.

[8] S. Haroche and J. M. Raimond. *Exploring the Quantum: Atoms, Cavities, and Photons*. Oxford University Press,Oxford, 2006.

[9] Jun Ye and Theresa W. Lynn. Applications of optical cavities in modern atomic, molecular, and optical physics. volume 49 of *Advances In Atomic, Molecular, and Optical Physics*, pages 1 – 83. Academic Press, 2003.

[10] F. G. Major V. N. Gheorghe and G Werth. *Charged particle traps*. Springer-Verlag Berlin Heidelberg, 2005.

[11] Tridib Ray, S. Jyothi, N.Bhargava Ram, and S.A. Rangwala. A thin wire ion trap to study ionatom collisions built within a fabryperot cavity. *Applied Physics B*, 114(1-2):267–273, 2014.

[12] Michael Tavis and Frederick W. Cummings. Exact solution for an *n*-molecule¯radiation-field hamiltonian. *Phys. Rev.*, 170:379–384, Jun 1968.

[13] MICHAEL TAVIS and FREDERICK W. CUMMINGS. Approximate solutions for an *n*-molecule-radiation-field hamiltonian. *Phys. Rev.*, 188:692–695, Dec 1969.

[14] Tridib Ray, Arijit Sharma, S. Jyothi, and S. A. Rangwala. Temperature measurement of laser-cooled atoms using vacuum rabi splitting. *Phys. Rev. A*, 87:033832, Mar 2013.

[15] Felix H. J. Hall and Stefan Willitsch. Millikelvin reactive collisions between sympathetically cooled molecular ions and laser-cooled atoms in an ion-atom hybrid trap. *Phys. Rev. Lett.*, 109:233202, Dec 2012.

[16] Wade G. Rellergert, Scott T. Sullivan, Svetlana Kotochigova, Alexander Petrov, Kuang Chen, Steven J. Schowalter, and Eric R. Hudson. Measurement of a large chemical reaction rate between ultracold closed-shell ca40 atoms and open-shell yb+174 ions held in a hybrid atom-ion trap. *Phys. Rev. Lett.*, 107:243201, Dec 2011.

[17] S. Jyothi, Tridib Ray, N. Bhargava Ram, and S. A. Rangwala. Phase sensitive radial extraction and mass spectrometry of trapped ions in a compact geometry. *Communicated*, 2014.

[18] Steven Chu, L. Hollberg, J. E. Bjorkholm, Alex Cable, and A. Ashkin. Three-dimensional viscous confinement and cooling of atoms by resonance radiation pressure. *Phys. Rev. Lett.*, 55:48–51, Jul 1985.

[19] Anthony J. Leggett. Bose-einstein condensation in the alkali gases: Some fundamental concepts. *Rev. Mod. Phys.*, 73:307–356, Apr 2001.

[20] D.M. Stamper-Kurn W. Ketterle, D.S. Durfee. *Proceedings of the International School of Physics Enrico Fermi", Course CXL*, pages 67–176, 1999.

[21] David M Weld and Wolfgang Ketterle. Towards quantum magnetism with ultracold atoms. *Journal of Physics: Conference Series*, 264(1):012017, 2011.

[22] D. Jaksch, H.-J. Briegel, J. I. Cirac, C. W. Gardiner, and P. Zoller. Entanglement of atoms via cold controlled collisions. *Phys. Rev. Lett.*, 82:1975–1978, Mar 1999.

[23] D Blume. Few-body physics with ultracold atomic and molecular systems in traps. *Reports on Progress in Physics*, 75(4):046401, 2012.

[24] D. Leibfried, R. Blatt, C. Monroe, and D. Wineland. Quantum dynamics of single trapped ions. *Rev. Mod. Phys.*, 75:281–324, Mar 2003.

[25] K. Blaum, Yu. N. Novikov, and G. Werth. Penning traps as a versatile tool for precise experiments in fundamental physics. *Contemporary Physics*, 51(2):149–175, 2010.

[26] R. Blatt and D. Wineland. Review article entangled states of trapped atomic ions. *Nature*, 453:1008, 2008.

[27] Winthrop W. Smith, Oleg P. Makarov, and Jian Lin. Cold ionneutral collisions in a hybrid trap. *Journal of Modern Optics*, 52(16):2253–2260, 2005.

[28] M.J. Thorpe and J. Ye. Cavity-enhanced direct frequency comb spectroscopy. *Applied Physics B*, 91(3-4):397–414, 2008.

[29] Paul R. Berman, editor. *Cavity Quantum Electrodynamics*. Academic Press, New York, 1994.22.

[30] J. F. Barry & D. DeMille E. S. Shuman. Laser cooling of a diatomic molecule. *Nature*, 467:820–823, 2010.

[31] Martin Zeppenfeld, Barbara Englert, Rosa Glckner, Alexander Prehn, Manuel Mielenz, Christian Sommer, Laurens van Buuren, Michael Motsch, and Gerhard

Rempe. Sisyphus cooling of electrically trapped polyatomic molecules. *Nature*, 491:570–573, 2012.

[32] Gilbert Grynberg Claude Cohen-Tannoudji, Jacques Dupont-Roc. *Atom-Photon Interactions: Basic processes and applications*. John wiley & Sons Inc., Hoboken, New Jersey, 1992.

[33] M. Suhail Zubairy Marlan O. Scully. *Quantum optics*. Cambridge University Press, 1997.

[34] T.W. Hnsch and A.L. Schawlow. Cooling of gases by laser radiation. *Optics Communications*, 13(1):68 – 69, 1975.

[35] E. L. Raab, M. Prentiss, Alex Cable, Steven Chu, and D. E. Pritchard. Trapping of neutral sodium atoms with radiation pressure. *Phys. Rev. Lett.*, 59:2631–2634, Dec 1987.

[36] Daniel A. Steck. *Classical and Modern Optics*. June 2008.

[37] William T. Silfvast. *Laser Fundamentals, 2'nd ed.* Cambridge University Press, 2004.

[38] M. Albert, J. P. Marler, P. F. Herskind, A. Dantan, and M. Drewsen. Collective strong coupling between ion coulomb crystals and an optical cavity field: Theory and experiment. *Phys. Rev. A*, 85:023818, Feb 2012.

[39] E.T. Jaynes and F.W. Cummings. Comparison of quantum and semiclassical radiation theories with application to the beam maser. *Proceedings of the IEEE*, 51(1):89 – 109, jan. 1963.

[40] P. Maunz, T. Puppe, I. Schuster, N. Syassen, P. W. H. Pinkse, and G. Rempe. Cavity cooling of a single atom. *Nature*, 428:50–52, 2004.

[41] Antonio Badolato, Kevin Hennessy, Mete Atatre, Jan Dreiser, Evelyn Hu, Pierre M. Petroff, and Atac Imamoglu. Deterministic coupling of single quantum dots to single nanocavity modes. *Science*, 308(5725):1158–1161, 2005.

[42] A. Wallraff, D. I. Schuster, A. Blais, L. Frunzio, R. S. Huang, J. Majer, S. Kumar, S. M. Girvin, and R. J. Schoelkopf. Strong coupling of a single photon to a superconducting qubit using circuit quantum electrodynamics. *Nature*, 431:162–167, 2004.

[43] R. J. Thompson, G. Rempe, and H. J. Kimble. Observation of normal-mode splitting for an atom in an optical cavity. *Phys. Rev. Lett.*, 68:1132–1135, Feb 1992.

[44] M. G. Raizen, R. J. Thompson, R. J. Brecha, H. J. Kimble, and H. J. Carmichael. Normal-mode splitting and linewidth averaging for two-state atoms in an optical cavity. *Phys. Rev. Lett.*, 63:240–243, Jul 1989.

[45] Gessler Hernandez, Jiepeng Zhang, and Yifu Zhu. Vacuum rabi splitting and intracavity dark state in a cavity-atom system. *Phys. Rev. A*, 76:053814, Nov 2007.

[46] H. Steinwedel W Paul. *Z. Naturforsch A*, 8:448, 1953.

[47] F. M. Penning. *Physica 3*, 873, 1936.

[48] J. R. Pierce. *Theory and design of electron beams*. Van Nostrand, Princeton, 1954.

[49] D.A Church. Collision measurements and excited-level lifetime measurements on ions stored in paul, penning and kingdon ion traps. *Physics Reports*, 228(56):253 – 358, 1993.

[50] J. Kleinert, C. Haimberger, P. J. Zabawa, and N. P. Bigelow. Trapping of ultracold polar molecules with a thin-wire electrostatic trap. *Phys. Rev. Lett.*, 99:143002, Oct 2007.

[51] L. Ricci, M. Weidemller, T. Esslinger, A. Hemmerich, C. Zimmermann, V. Vuletic, W. Knig, and T.W. Hnsch. A compact grating-stabilized diode laser system for atomic physics. *Optics Communications*, 117(56):541 – 549, 1995.

[52] K. Ravi. *Trapping and Cooling of Ions and the Study of Ion Atom Interactions*. PhD thesis, Raman Research Institute, 2012.

[53] Seunghyun Lee, K. Ravi, and S. A. Rangwala. Measurement of collisions between rubidium atoms and optically dark rubidium ions in trapped mixtures. *Phys. Rev. A*, 87:052701, May 2013.

[54] J. J. Sanchez-Mondragon, N. B. Narozhny, and J. H. Eberly. Theory of spontaneous-emission line shape in an ideal cavity. *Phys. Rev. Lett.*, 51:550–553, Aug 1983.

[55] J. J. Childs, K. An, M. S. Otteson, R. R. Dasari, and M. S. Feld. Normal-mode line shapes for atoms in standing-wave optical resonators. *Phys. Rev. Lett.*, 77:2901–2904, Sep 1996.

[56] G. S. Agarwal. Vacuum-field rabi splittings in microwave absorption by rydberg atoms in a cavity. *Phys. Rev. Lett.*, 53:1732–1734, Oct 1984.

[57] Yifu Zhu, Daniel J. Gauthier, S. E. Morin, Qilin Wu, H. J. Carmichael, and T. W. Mossberg. Vacuum rabi splitting as a feature of linear-dispersion theory: Analysis and experimental observations. *Phys. Rev. Lett.*, 64:2499–2502, May 1990.

[58] Daniel A. Steck. Rubidium 85 d line data. 19 September, 2012.

[59] A. E. Siegman. *Lasers*. University Science Books, 2003.

[60] David S. Weiss, Erling Riis, Yaakov Shevy, P. Jeffrey Ungar, and Steven Chu. Optical molasses and multilevel atoms: experiment. *J. Opt. Soc. Am. B*, 6(11):2072–2083, Nov 1989.

[61] Paul D. Lett, Richard N. Watts, Christoph I. Westbrook, William D. Phillips, Phillip L. Gould, and Harold J. Metcalf. Observation of atoms laser cooled below the doppler limit. *Phys. Rev. Lett.*, 61:169–172, Jul 1988.

[62] M. S. Santos, P. Nussenzveig, L. G. Marcassa, K. Helmerson, J. Flemming, S. C. Zilio, and V. S. Bagnato. Simultaneous trapping of two different atomic species in a vapor-cell magneto-optical trap. *Phys. Rev. A*, 52:R4340–R4343, Dec 1995.

[63] Andrew T. Grier, Marko Cetina, Fedja Oručević, and Vladan Vuletić. Observation of cold collisions between trapped ions and trapped atoms. *Phys. Rev. Lett.*, 102:223201, Jun 2009.

[64] David R. Lide., editor. *CRC Hand Book of Chemistry and Physics*. CRC Press, New York, 2004.

[65] Seunghyun Lee. *The study of trapped ion collisions with cold atoms and cold molecules*. PhD thesis, Raman Research Institute, 2013.

[66] C. Gabbanini, A. Fioretti, A. Lucchesini, S. Gozzini, and M. Mazzoni. Cold rubidium molecules formed in a magneto-optical trap. *Phys. Rev. Lett.*, 84:2814–2817, Mar 2000.

[67] A. R. L. Caires, V. A. Nascimento, D. C. J. Rezende, V. S. Bagnato, and L. G. Marcassa. Atomic density and light intensity dependences of the rb_2 molecule formation rate constant in a magneto-optical trap. *Phys. Rev. A*, 71:043403, Apr 2005.